Electron Optics
in Ballistic Graphene

Inauguraldissertation

zur
Erlangung der Würde eines Doktors der Philosophie
vorgelegt der
Philosophisch-Naturwissenschaftlichen Fakultät
der Universität Basel

von

Peter Simon Rickhaus
aus Gündlischwand BE

UNI
BASEL

Basel, 2015

Genehmigt von der Philosophisch-Naturwissenschaftlichen Fakultät
auf Antrag von

        Prof. Dr. Christian Schönenberger
        Prof. Dr. Lieven Vandersypen
        Prof. Dr. Klaus Ensslin

Basel, 15.9.2015

                                                Prof. Dr. Jörg Schibler
                                                      Dekan

Contents

1 Introduction

Isaac Newton believed that light consists of what he called corpuscles. These small and heavy particles are emitted ballistically from shining objects and thereby explain straight light trajectories and reflections. His opponent was the dutch physicist Christiaan Huygens, who stated that light is best described as a wave that propagates in a medium, the aether. This theory in turn described the phenomena of refraction and diffraction in a better way. At first, Newton's theory was more popular mainly due to the excellent reputation of its author. Only the experiments of Young, who measured interference patterns e. g. behind a double-slit structure, disproved Newton. The pattern that Young observed was best described as a superposition of two circular waves, that interfere positively or negatively. In the early twentieth century it was found that the concepts of Newton and Huygens were both correct to some degree. Light is a relativistic particle and a wave propagating in vacuum.

Apparently, the nature of light caused a long and intense debate which repeated when the electron was discovered in the turn of the twentieth century by Wiechert and Thomson as the particle that carries charge and, if mobile, transports electrical current in a conductor. The wave nature of electrons was proven in interference experiments as well in the 1930s by Davisson and Germer with free electrons in vacuum. However, such experiments are way more challenging in a conductor. Since electrons are massive and charged, they easily interact with their environment. Most prominent are interactions with lattice vibrations (i. e., phonons), crystalline defects and uncontrolled electrostatic potentials that typically originate from impurities in the proximity of the conductor. To observe a wave-like behavior, the conductor needs to be a defect-free material in a clean environment and measured at low temperatures, where electron-phonon scattering is reduced. Under such conditions, the propagation of an electronic wavefunction is described by the time-dependent Schrödinger equation. The mathematical similarity to Maxwell's wave-equation leads to a vast amount of phenomena that can be analogously observed in quantum-mechanical and in optical systems.

These phenomena are joined in the field of electron optics [1], which has evolved in three waves. First, in 1927, Bush could focus free electrons in vacuum using a magnetic lense [2]. This has triggered the development of complex electron-optical systems of which the scanning electron microscope (SEM) [3] is the most famous. In

a second wave [4], classical ballistic transport has been realized in metals [5, 6] and later, quantum ballistic transport in high-mobility two-dimensional electron gases (2DEG) [7–10], triggering the concept of mimicking optical systems in condensed matter physics. And finally, with the advent of graphene [11], the idea of electron optics got a new twist [12, 13].

The two experiments that triggered the field of condensed-matter electron optics are the quantum point contact (QPC) and the magnetic focusing. Point contacts were realized first in metals [5] and then in 2DEGs [7] where the conductance exhibits plateaus separated by $2\,e^2/h$. Already the first explanations [4, 14] stressed the analogy to optics: The confinement potential acts as a multi-mode waveguide where the transverse modes are quantized. The number of modes is tuned by the electron density n in the channel, which is related to the wavelength λ by $n = 2\pi/\lambda^2$. If λ is smaller than the width of the QPC, the transmission probability is one, otherwise zero. In the optical analogue, monochromatic light of frequency ν and polarized in z-direction ($E_x = E_y = B_z = 0$) is sent to a metallic screen that has a long slit along z-direction. The wave equation for this problem is similar to the Schrödinger equation of a 2DEG (with $\lambda \to \lambda_F$) if the QPC has boundaries with infinite potential walls. The same transmission probability is obtained in both systems for equal distribution of the impinging energy (optical) or particle flux (QPC) [4].

There are two very distinct ways to realize a lense in a two-dimensional conductor. On the one hand, having a QPC as a point source and another one as a detector, the electronic wavefunction could be focused with a biconcave lense [15]. This lense was formed electrostatically by gates that locally tune the wavelength and thereby engineer the refraction properties. On the other hand, by applying a perpendicular magnetic field, focusing is also possible. If electrons are injected at a QPC under different angles and bent by the Lorentz force, the trajectories (called "skipping orbits") are reflected in a specular way from the walls which leads to the formation of a cusp structure. Here, the walls, defined by depleted regions of the 2DEG, act as mirrors whereas the magnetic field can be seen as a lens, with an optical aberration causing the cusp structure [4]. A condition that needs to be met is that the walls or the mirror are reflective in a specular and non-diffusive way. This was only achieved in 2DEGs where λ_F is typically much larger than the roughness of the boundary.

Another class of optical experiments deals with interference effects. Generally, the wave nature of any physical entity is demonstrated by measuring an interference pattern. We distinguish two types of interferometers: two-path and multi-pass interferometers. Examples for the former are the Michelson and the Mach-Zehnder types, which are both widely used in optical experiments. In 2DEGs, two-path interferometers have been realized in double slit experiments [16–19] or in an electronic realization of the Mach-Zehnder interferometer [20]. The latter is operated in high magnetic fields where QPCs act as semi-transparent mirrors or beam splitters and Quantum Hall edge states as electron beams. In contrast, the Fabry-Pérot (FP) interferometer is of the multi-pass type. In optics, an FP interferometer is an element that consists of a transparent glass plate with two partially reflective surfaces on opposite sides. It can therefore be viewed as a cavity. Light within the cavity is bouncing back

and forth between the mirrors, but at each reflection a fraction of light is coupled out. The superposition of all outgoing waves gives rise to an intensity modulation (the interference pattern) that depends on the wavelength of the light and the distance between the mirrors. In solid-state physics, a two-dimensional conducting sheet between two electrodes can realize an electronic FP interferometer [21].

Such electron-optics experiments can be realized in graphene as well. There are, however, two very special aspects about this two-dimensional crystal regarding its suitability for electron optics. First, its low-energy electronic excitations are described by massless Dirac fermions that have a linear dispersion relation similar to photons [11, 22]. The velocity v_F of the charge carriers in this material is very high and constant, i.e. $v_F = c/300$, where c is the speed of light. Second, it is possible to form gapless p-n interfaces in graphene. These interfaces are formed by combining regions of electron (n) and hole (p) doping. The transmission probability depends only on the angle of incidence and can be tuned from zero to one, making it an attractive and novel tool for electron-optics. Taking advantage of this "optics-like" electron dynamics, generic optical elements like lenses, beam splitters and wave guides have been proposed for electrons in engineered ballistic graphene [12, 13]. These proposals require ballistic transport which has become achievable in graphene recently.

This thesis is centered on the experimental observation of electron-optics phenomena in graphene. In **Chapter 2**, graphene is introduced and the ability to form p-n junctions, with particular regard to electron optics experiments, is discussed.

Since ballistic transport is crucial for this subject, the question "when is graphene clean?" is posed in **Chapter 3**, where different characterization methods are compared and linked to devices of this thesis. The experimental part begins with a description of the fabrication methods in **Chapter 4**, which is 'spiced' with information about complex device structures, superconducting contacts and the use of CVD-grown graphene.

Chapter 5 describes an interference experiment over a distance of $2\,\mu$m, where we used p-n junctions to tune and manipulate ballistic Fabry-Pérot resonances. The peculiar angular dependence of the transmission allows to filter out large propagation angles. Thus, the p-n interface can be used to form coherent planar waves, i.e. it acts in this case similar to an optical polarization filter. This filtering effect is crucial for the high visibility of Fabry-Pérot resonances we achieved in p-n and p-n-p devices.

A perpendicular magnetic can be viewed as a lens which bends and focuses electrons. Along a p-n interface, this leads to trajectories that curve back and forth. Such trajectories are called snake states and they give rise to magneto-conductance oscillations. In terms of optics, these oscillations occur since the focal point of the magnetic lens can be either on the left- or on the right side of the p-n cavity. We demonstrate the observation of snake states in **Chapter 6**.

Furthermore, the p-n interface can be viewed as a mirror that is reflective or semi-transparent, depending on the angle of incidence. By using such mirrors it is possible to create channels for electrons that are described in a similar way to optical waveguides. However, the refraction can be tuned dynamically and p-n interfaces can be exploited to create additional confinement. We use this to guide electrons in an elec-

trostatic channel in **Chapter 7** where we observe signatures of quasi 1-dimensional transport. The thesis is complemented in **Chapter 8** with unpublished results on a device that allows to explore the properties of a tilted p-n interface that acts as a beam-splitter.

2

Optics with electrons in Graphene

In this chapter, the basic working principles of graphene-based electron-optic elements will be explained. After some introductory words on graphene, effects of interfaces having different charge carrier densities are discussed. For this purpose, the negative index of refraction at an electron-hole (p-n) interface and the phenomena of Klein-tunneling and Klein collimation are introduced. Afterwards it is explained how p-n cavities lead to complex Fabry-Pérot patterns. Furthermore, the tight-binding simulation techniques used throughout this work by our collaborators from theory are discussed. This theory chapter follows partly References [23, 24].

2.1. Properties of graphene

2.1.1. The bandstructure of graphene

The graphene honeycomb lattice has two atoms in the unit cell which form the two sublattices A and B. The unit cell is sketched in Figure 2.1a and it is spanned by the two lattice vectors $\mathbf{a_1}$ and $\mathbf{a_2}$. Transport is described in a tight-binding formalism, where electrons hop from one lattice site to another. Next-nearest neighbor hopping will lead to a correction of the band structure at high energies and is often neglected. The nearest-neighbor vectors are:

$$\mathbf{d_1} = \begin{pmatrix} -\sqrt{3}a/2 \\ -a/2 \end{pmatrix}, \ \mathbf{d_2} = \begin{pmatrix} \sqrt{3}a/2 \\ -a/2 \end{pmatrix}, \ \mathbf{d_3} = \begin{pmatrix} 0 \\ a \end{pmatrix}. \tag{2.1}$$

Here, $a = 1.42\,\text{Å}$ is the inter-atom distance. The tight-binding Hamiltonion, which describes hopping from one to another atom with the creation or annihilation operators $\psi(\mathbf{R})$ and $\psi^\dagger(\mathbf{R})$, is:

$$H = -\gamma_0 \sum_{\mathbf{R}} \psi^\dagger(\mathbf{R}) \left\{ \psi(\mathbf{R} + \mathbf{d_1}) + \psi(\mathbf{R} + \mathbf{d_2}) + \psi(\mathbf{R} + \mathbf{d_3}) \right\} + h.c., \tag{2.2}$$
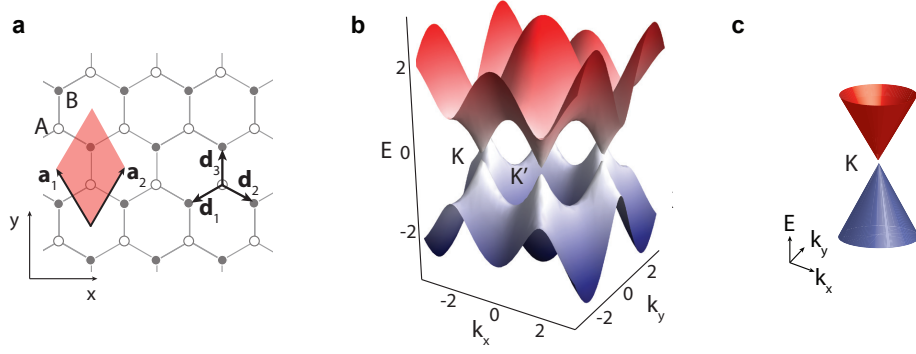
Figure 2.1.: **a**, In graphene, carbon atoms are arranged in a honey-comb lattice. The unit cell (red) contains two atoms. **b**, Band-structure of graphene, adapted from [25]. **c**, At low energies and in the vicinity of the K, K' points, charge carriers are described by the linear dispersion $E = \hbar v_F k$.

where the on-site energy is set to zero. The operators can be written in momentum space. For example, the operator that annihilates an electron on sublattice B with momentum **k** is:

$$c_{B,\mathbf{k}} = \frac{1}{\sqrt{N}} \sum_{\mathbf{R}} e^{i\mathbf{k}\mathbf{R}} \psi(\mathbf{R} + \mathbf{d3}), \tag{2.3}$$

where N is the number of lattice points. The Hamiltonian then simplifies to

$$H = -\gamma_0 \sum_{\mathbf{k}} \gamma_{\mathbf{k}} c_{A,\mathbf{k}}^{\dagger} c_{B,\mathbf{k}} + h.c. \text{ with } \gamma_{\mathbf{k}} = 1 + e^{i\mathbf{k}\mathbf{a_1}} + e^{i\mathbf{k}\mathbf{a_2}}. \tag{2.4}$$

It is now very convenient to write the sublattice index as a vector, i.e. $c_{A,\mathbf{k}} = (1,0)$ and $c_{B,\mathbf{k}} = (0,1)$. The Hamiltonian takes the form

$$H = -\gamma_0 \sum_{\mathbf{k}} \begin{pmatrix} 0 & \gamma_{\mathbf{k}} \\ \gamma_{\mathbf{k}}^{\star} & 0 \end{pmatrix}, \tag{2.5}$$

with the eigenvalues

$$E = \pm \gamma_0 |\gamma_{\mathbf{k}}|. \tag{2.6}$$

This function is plotted in Figure 2.1b. Graphene has two bands which touch at six points in the Brillouin zone, the so called Dirac points. Therefore, graphene is called a zero-bandgap semiconductor. In undoped graphene, the Fermi level is at the Dirac point and can be shifted by changing the on-site energy (i.e. the diagonal terms in Equation 2.6). Only two of the six touching points are not equivalent and they are referred to as the K and K' valley.

In graphene, charge carriers with small quasi-momentum $\hbar\mathbf{k}$, i. e. in the vicinity of the K and K' points, have a linear energy dispersion (see Figure 2.1c). In the conduction and valence band, the energy $E(\mathbf{k})$ as a function of wavevector **k** is given

by $E_c(\mathbf{k}) = \hbar v_F k$ and $E_v(\mathbf{k}) = -\hbar v_F k$, respectively, where $k = |\mathbf{k}|$ and v_F is the Fermi velocity; see Figure 2.1c. As a consequence, their velocity $v_F = 3\gamma_0 a/(2\hbar) = c/300$ (first derivative of $E(\mathbf{k})$) is constant.

The low-energy Hamiltonian describing the linear dispersion relation is obtained by linearizing Equation 2.6 around the K and K'- points:

$$H \approx \hbar v_F \begin{pmatrix} 0 & \pm k_x - ik_y \\ \pm k_x + ik_y & 0 \end{pmatrix} = \hbar v_F \boldsymbol{\sigma} \boldsymbol{k} \ \text{ with } \ \boldsymbol{\sigma} = \begin{pmatrix} \pm\sigma_x \\ \sigma_y \end{pmatrix}. \qquad (2.7)$$

The $\pm$-sign accounts for the K and K' point respectively. Since they are at the opposite corner of the Brillouin zone, the sign of k_x is positive or negative respectively. The Hamiltonian in real space, with a chemical potential E_g, reads:

$$H = \mathbf{1}E_g + \hbar v_F \boldsymbol{\sigma} \boldsymbol{\nabla}, \qquad (2.8)$$

which is a Dirac equation.

The linear dispersion relation yields an electron density n given by $n = \text{sgn}(E)k^2/\pi$. Compared to other two-dimensional electron-gases with parabolic dispersion relation (such as GaAs), the density of states $D(E)$ depends on the energy, i.e.

$$D(E) = \frac{2E}{\pi\hbar^2 v_F^2}, \qquad (2.9)$$

where spin and valley degeneracy are included. Note that $D(E)$ vanishes at the Dirac point.

2.1.2. Pseudospin and Berry-phase

Since the unit cell of the graphene crystal contains two atoms, the charge carriers have an additional degree of freedom, called pseudospin. It describes the orbital wavefunction of the two sublattices and is described as a spin 1/2 at low energies where the dispersion relation is linear.

Equation 2.7 can be rewritten using $k_x + ik_y = k_F e^{i\theta}$ with $\theta = \arctan(k_y/k_x)$ the angle of propagation:

$$H = \begin{pmatrix} 0 & \pm k_F e^{\mp i\theta} \\ \pm k_F e^{\pm i\theta} & 0 \end{pmatrix}, \qquad (2.10)$$

which has the normalized eigenvectors $|\boldsymbol{k}+\rangle$ in the conduction and $|\boldsymbol{k}-\rangle$ in the valence band:

$$|\boldsymbol{k}+\rangle = \frac{1}{\sqrt{2}} \begin{pmatrix} e^{\mp i\theta/2} \\ +e^{\pm i\theta/2} \end{pmatrix}, \ |\boldsymbol{k}-\rangle = \frac{1}{\sqrt{2}} \begin{pmatrix} e^{\mp i\theta/2} \\ -e^{\pm i\theta/2} \end{pmatrix}, \qquad (2.11)$$

where the $\pm$-sign accounts for the solution around the K or K' valley again. In a more compact way, the eigenvector $|\boldsymbol{s}\rangle$ with the parameter $s = 1$ for electrons and
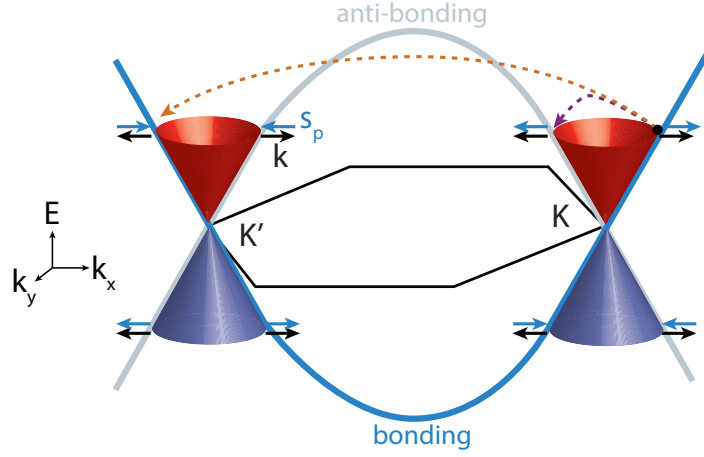
Figure 2.2.: Dirac cones in the valence (blue) and the conduction band (red) at low energies with the propagation direction (black) at different energies in the K and K' valley and the corresponding pseudospin vector $\boldsymbol{s}_p$, pointing parallel to $\boldsymbol{k}$ for the bonding and anti-parallel for the anti-bonding orbitals.

$s = -1$ for holes reads:

$$|\boldsymbol{s}\rangle = \frac{1}{\sqrt{2}} \begin{pmatrix} e^{\mp i\theta/2} \\ se^{\pm i\theta/2} \end{pmatrix}. \tag{2.12}$$

The vector in Equation 2.12 is in the pseudospin space. Similar to a real spin, it can be viewed as the result of a spin-1/2 rotation operator $R(\theta)$ acting on the initial state $|\mathbf{s}_0\rangle$ which points along the y-direction:

$$|\mathbf{s}\rangle = R(\theta)|\mathbf{s}_0\rangle = \begin{pmatrix} e^{\mp i\theta/2} & 0 \\ 0 & e^{\pm i\theta/2} \end{pmatrix} \begin{pmatrix} 1/\sqrt{2} \\ s/\sqrt{2} \end{pmatrix} \tag{2.13}$$

If $|\mathbf{k}\rangle$ is rotated by 2π, $R(2\pi) = e^{i\pi}$ which means that a phase of π is added to the wavefunction. In other words: If the origin in k-space (here $\mathbf{K}$) is encircled, a phase of π is picked up by the charge carrier. This phase is called the Berry phase.

The pseudospin points in propagation direction in the $\mathbf{K}$-valley. This can be ascertained by considering that the helicity operator, which projects the spin onto the direction of momentum, is defined as:

$$\hat{h} = \frac{1}{2k}\boldsymbol{\sigma}\boldsymbol{k}, \tag{2.14}$$

which is proportional to H (Equation 2.7) such that the eigenvectors are also eigenstates of $\hat{h}$. For s=1 the pseudospin is parallel and for s=-1 anti-parallel to $\mathbf{k}$ and one speaks of right-handed Dirac fermions and left-handed Dirac anti-fermions respectively. At the other edge of the Brillouin-zone (i.e. at the $\mathbf{K}'$ point), the helicity

is inverted. Figure 2.2 summarizes this.

As a consequence, backscattering, i.e. the process which flips $\mathbf{k} \to -\mathbf{k}$, is suppressed within the same valley. Consider the electron, marked with a black dot in Figure 2.2. A backscattering process within the same valley would invert the helicity, which is not allowed since helicity is a conserved quantity at low energies. Backscattering with conserved helicity would involve an electron of the opposite valley and would require a large momentum therefore. Such backscattering is only possible if the potential in real space changes abruptly at the atomic level, e.g. at the edge of a graphene flake, at atomic defects or at very small wrinkles.

2.1.3. Half-integer quantum Hall effect

The Hall effect [26] is observed in a geometry where the current I_x flows along the x axis and a perpendicular magnetic field B_z is applied. Due to the Lorentz force, charge carriers are deflected in y direction which causes a voltage drop V_y between upper and lower boundary of the sample. The measured resistivity, calculated from the equation of motion in steady state $m\dot{\boldsymbol{v}} = -e\boldsymbol{v} \times \boldsymbol{B} - e\boldsymbol{E} - m/\tau\boldsymbol{v} = 0$, is:

$$\rho = \rho_0 \begin{pmatrix} 1 & \omega_c\tau \\ -\omega_c\tau & 1 \end{pmatrix}, \tag{2.15}$$

with e. g. $\rho_{xy} = V_y/I_x$, m the effective mass of the charge carrier, τ the inelastic scattering time in the Drude model and $\rho_0 = ne^2\tau/m$ the resistivity at $B_z = 0$. Since the cyclotron frequency is $\omega_c = eB/m$, ρ_{xx} is constant with increasing B_z, whereas ρ_{xy} increases linearly.

In a high-mobility 2-dimensional electron gas (2DEG) at low temperatures, ρ_{xx} drops to zero, whereas $\rho_{xy} = h/(e^2\nu)$ with $\nu = 1, 2, 3, ...$ becomes quantized [27]. This is the case if B_z is large enough for electrons to complete orbits within the mean free path. The energy levels $E_N = \hbar\omega_c(N+1/2)$ are called Landau levels (LL), where N is an integer. The filling factor ν, responsible for the conductance plateaus, is given by the density n of charge carriers per flux quantum: $\nu = n/(eB/h)$.

In graphene, solving the Dirac equation in a perpendicular magnetic field yields the LL energies:

$$E_N = \pm v_F\sqrt{2e\hbar B \cdot N}. \tag{2.16}$$

Due to the square-root dependence on B, there is a large spacing between the first two LLs which leads to the observation of the QHE at room temperature [28]. The Hall conductivity takes the form

$$\sigma_{xy} = \frac{4e^2}{h}(N+1/2). \tag{2.17}$$

The factor of 4 in this formula is due to spin and valley degeneracy, whereas the shift of 1/2 is due to the Berry phase picked up by closed orbits.

The quantum Hall effect is usually measured in a six-terminal device, a so-called

Hall-bar. For this thesis, we measured only two-terminal Hall conductances. This leads to a mixing of the σ_{xx} and σ_{xy} components, but the plateaus can be still easily identified if the aspect ratio of the device $W/L \approx 1$ [29, 30].

2.2. Graphene *p-n* junctions

Graphene *p-n* junctions are described by two regions with different potential V, one with negative energy compared to the charge-neutrality point, and one with positive energy. Such *p-n* junctions can be formed artificially by electrostatic gating, but they are also present at low densities where electron-hole puddles dominate the transport properties [31]. For electron optics, two properties of such junctions are important: The negative refraction and the angular dependence of transmission. Therefore, we first introduce Snell's law in unipolar (*n-n* or *p-p*) and bipolar (*p-n* or *n-p*) graphene and then describe Klein tunneling. The transmission properties are altered in the case of smooth *p-n* interfaces which are important regarding the experimental setup. After describing the conductivity of a *p-n* junction we explain how Fabry-Pérot resonances in *p-n* cavities can be observed in transport experiments.

2.2.1. Snell's law in Graphene

In graphene, the local Fermi energy takes the role of the refractive index. This simply follows from the condition that the parallel momentum k_y at an interface has to be conserved. The refraction at the interface is described by Snell's law in graphene:

$$E_l \cdot \sin(\theta_l) = E_r \cdot \sin(\theta_r) \tag{2.18}$$

This is illustrated in Figure 2.3 for a unipolar *n-n'* and a bipolar *n-p* interface. In Figure 2.3a, the Fermi-energy on the left (l) side is larger than on the right (r) side, leading to a larger k-circle at the Fermi energy. Since the k_y component has to be conserved, this situation will lead to a refraction towards the interface. The angle for total internal reflection is simply given by $\theta_c = \arcsin(E_l/E_r) = \arcsin(k_l/k_r)$, and is obtained for $k_{y,l} > |\mathbf{k}_r|$.

The situation for a *p-n* interface as sketched in Figure 2.3b is more interesting. Again, k_y needs to be conserved and therefore the angle of the back-reflected trajectory $\theta_l' = \theta_l$. Since the transmitted electron needs to have a positive group velocity **v** in the x direction and since **v** is anti-parallel to **k**, it follows that $k_{x,l} = -k_{x,r}$ for a symmetric *p-n* junction (i. e. $|n_l| = |p_r|$). In summary:

$$k_{y,l} = k_{y,r} = k_{y,l}' \quad \text{and} \quad k_{x,l} = -k_{x,r} = -k_{x,l}' \tag{2.19}$$

From Equation 2.18, the index of refraction, defined as $sin(\theta_r)/sin(\theta_l)$, is negative in a graphene *p-n* junction. This allows to focus charge carriers from an injector to a detector point by using a straight interface as shown in Figure 2.3c. This Veselago
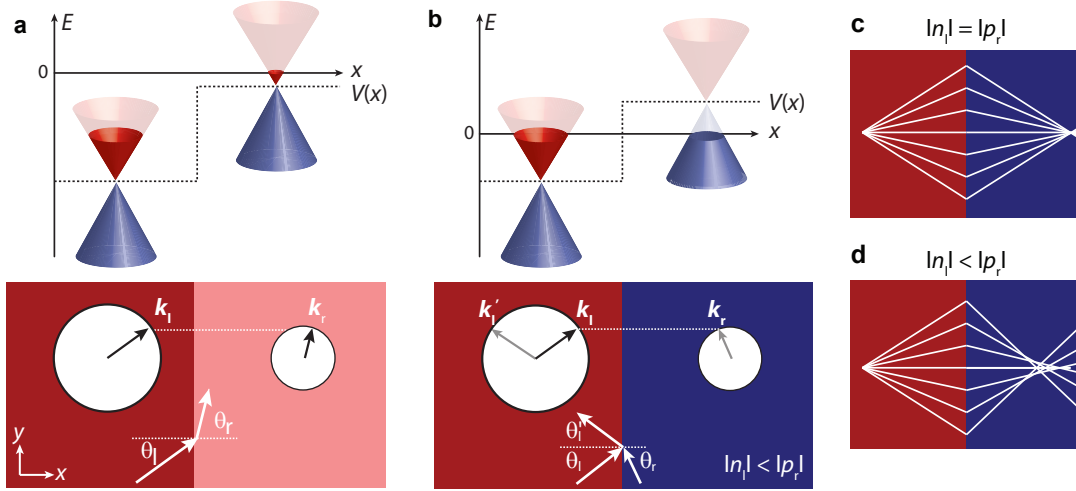
Figure 2.3.: **a**, Illustration of Snell's law in graphene for a unipolar *n-n'* junction. An electron with angle of incidence θ_l will be transmitted under angle θ_r due to conservation of parallel momentum k_y. **b**, At a *p-n* interface, the incident electron can be reflected under angle θ_l' or transmitted under angle θ_r. Again, the parallel momentum and the energy need to be conserved. **c**, Due to the negative index of refraction at a *p-n* interface, electrons can be focused from one point to another with a straight lense, the Veselago lense. **d**, The focal point becomes blurry for asymmetric doping, here $|n_l| < |p_r|$.

lense was described first by Cheianov et. al. for graphene [12]. For an antisymmetric junction with $|n_l| < |p_r|$, the focal point becomes blurry and a caustic pattern forms as sketched in Figure 2.3d. Apparently, the Veselago lense requires rather sharp *p-n* interfaces such that trajectories with large angles are transmitted as well and can be focused. Otherwise, the transport between injector and detector will be dominated by the $\theta = 0$ trajectories which are always transmitted.

2.2.2. Klein tunneling and Klein collimation

The Klein paradox was discovered by Oskar Klein who calculated the transmission t at a barrier $V(x)$ for relativistic particles in 1929 [32]. He found that t does not decay with distance, contradicting non-relativistic quantum mechanics where the transmission at a potential barrier of height V is exponentially decaying i.e. $|t|^2 \sim e^{-kx}$. The reason for Klein's paradoxical finding is that the transmitted particles propagate as anti-particles as it was discovered later [33]. In addition, the result $|t|^2 \sim 1$ obtained by Klein is valid only for a sharp potential step as it has been clarified by Sauter [34]. He found an exponentially decaying transmission, if the potential $V(x)$ is gradually changing over a distance d larger than the Compton wavelength $\lambda_c = h/mc$.

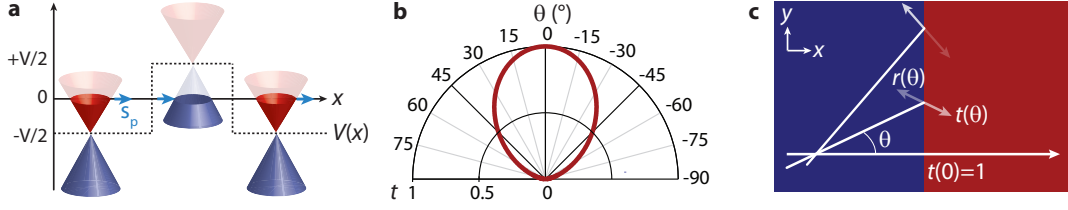Figure 2.4.: **a**, A *p*-*n*-p junction is formed by a potential profile $V(x)$ which is positive (+V/2) on one side and negative (-V/2) on the other side of the interface with respect to the charge neutrality point. The pseudospin $\mathbf{s}_p$ is conserved if the charge carrier is transmitted, but would need to be flipped in the case of reflection. **b-c**, Transmission t as a function of incidence angle θ at a single *p*-*n* interface. The Klein-tunneling case is $t(0) = 1$.

In graphene it is possible to form regions of electron (n) and hole doping (p) by using electrostatic gates [35]. Due to the gapless dispersion relation, the interface between these regions is not insulating making it possible to observe the Klein paradox in graphene. The Klein paradox is experimentally realized in a *p-n-p* junction, as shown in Figure 2.4a, where the transmission would exponentially decay in the middle region for non-relativistic carriers. If an electron with momentum $\mathbf{k} = \mathbf{k}_x$ crosses the interface, backscattering ($k_x \rightarrow -k_x$) is forbidden as explained before. On the other hand, due to the symmetry of the potential, the parallel momentum k_y is conserved. It follows that the transmission t for perpendicular incidence, $\theta = 0$, is [36]

$$|t(\theta = 0)|^2 = 1. \tag{2.20}$$

This is known as Klein tunneling. During the process, the pseudospin $\mathbf{s_p}$ is conserved, since it is parallel to $\mathbf{k}$ in the conduction- and anti-parallel in the valence band, as depicted in Figure 2.4a. An indirect experimental proof of Klein tunneling has been given by Young et. al. [37] by studying the transmission of a phase-coherent *p-n-p* interface in a magnetic field. The authors applied a weak B field such that the origin in k-space was encircled and the Berry phase was picked up. By studying the Fabry-Pérot interference (Chapter 2.2.5), they observed a phase shift of π at a critical field and could conclude that the transmission at the *p-n* interface was largest for small angles.

Now we consider the angular transmission at a single *p-n* interface in the case of a symmetric and sharp potential. For oblique incidence, t decreases and backscattering becomes possible. The angle dependence of the transmission, obtained by matching the real-space wavefunctions right and left of the *p-n* interface, is given by [38]:

$$|t(\theta)| = cos^2(\theta). \tag{2.21}$$

For electrons impinging on the interface at 45°, transmission and reflection probability

are both 50%, as shown in Figure 2.4b-c for a single *p-n* interface.

2.2.3. Smooth versus sharp *p-n* interface
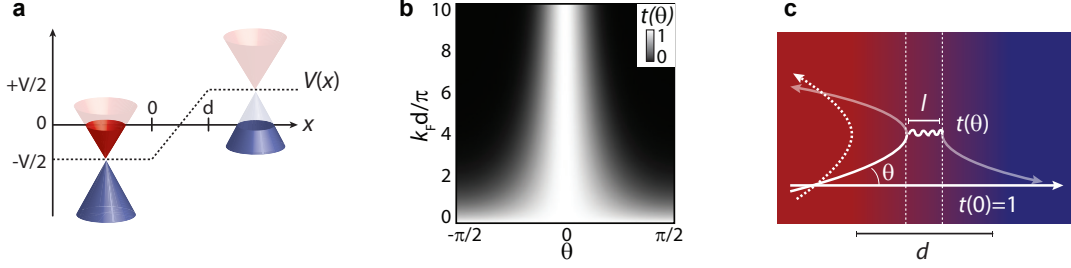
Figure 2.5.: **a**, Potential profile of an ideal smooth *p-n* interface. Within a length of d, the potential is gradually changing from n to p. **b**, Due to the additional electric field, trajectories reaching the *p-n* interface under an angle θ bend away from the interface. They come closest to the interface at a distance l. Therefore, their transmission probability depends exponentially on the injection angle. **c**, Transmission probability $t(\theta, k_{\mathrm{F}}d/\pi)$ of an ideal smooth *p-n* interface.

In reality, the experimentally available *p-n* interfaces are not sharp, but change gradually from p- to n on a lengthscale d. If d is the length over which the carrier density varies and k_{F} the Fermi wavevector far away from the interface, the junction is assumed to be smooth if $k_{\mathrm{F}}d \gg 1$ and sharp in the opposite limit. The simplest case of such a profile reads:

$$
V(x) = \begin{cases} -V/2 & x < 0 \\ Fx & 0 \leq x \leq d \\ V/2 & x > d \end{cases} \tag{2.22}
$$

where $\pm V/2$ is the Fermi energy in the left (right) bulk and $F = V/d = \hbar k_{\mathrm{F}}/d$ the electric field created by the gradually changing potential. The potential is sketched in Figure 2.5a. We now yield an exponentially decaying transmission for $\theta > 0$:

$$
|t(\theta)| = e^{-\pi k_{\mathrm{F}}d \cdot \sin^2\theta} \tag{2.23}
$$

This function is shown in Figure 2.5b, where the transmission $|t|$ as a function of θ and the dimensionless parameter $k_{\mathrm{F}}d/\pi$ is plotted. Here, k_{F} refers to the bulk part. We find e. g. that 50% transmission for $\lambda = 100\,\mathrm{nm}$ is achieved for $\theta \approx 7°$.

The exponential dependence of t on the angle of incidence can be understood by taking into account that trajectories entering the smooth region obliquely, gradually turn away from the interface due to the additional electric field F. This is sketched in Figure 2.5c where the electron trajectory with incidence angle θ comes closest to the interface at the turning point $l = v_F p_y/F$ [38]. Now it has an exponential

tunneling probability to reach the other side. The exponential dependence on the angle is similar to the exponential dependence that Sauter [34] has found for massive relativistic particles. His solution is similar to Equation 2.23 for $v_F \to c$, $\lambda_F \to \lambda_c$ and $sin(\theta) \to m$, where m is the mass of the (free) particle. In graphene it is therefore possible to study the Klein ($t = 1$) and Sauter situation by looking at different angles of incidence θ.
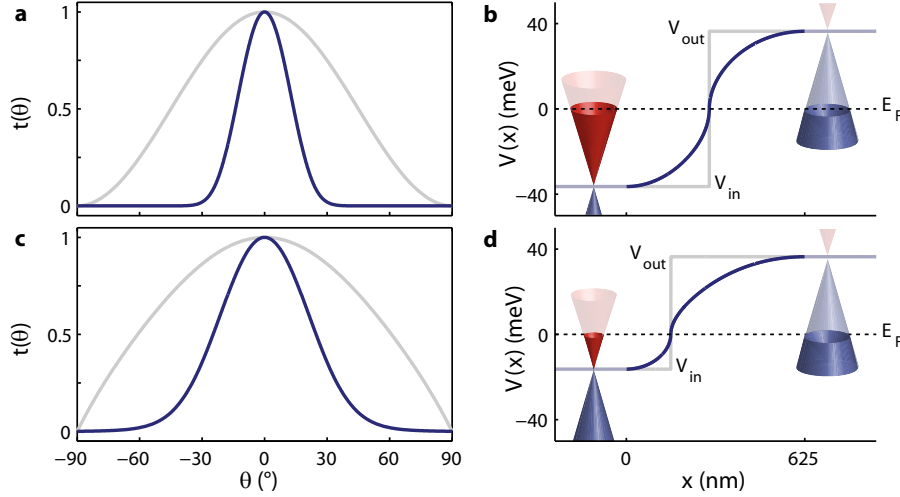
Figure 2.6.: Angle-resolved transmission function (blue curves) $t(\theta)$ across a realistic *p-n* junction at carrier densities $(n_{\text{in}}, n_{\text{out}}) = (10, -10) \times 10^{10}\,\text{cm}^{-2}$ in **a** and $(n_{\text{in}}, n_{\text{out}}) = (2, -10) \times 10^{10}\,\text{cm}^{-2}$ in **c**, taking into account the smooth junction profiles $V(x)$ obtained from electrostatic calculations of a suspended graphene device and sketched (blue curves) in **b** and **d**, respectively. Gray curves in **a** and **c** are $t(\theta)$ when the smooth $V(x)$'s are replaced with ideally abrupt profiles as sketched (gray steps) in **b** and **d**, where $V_{\text{in/out}} = -\,\text{sgn}(n_{\text{in/out}})\hbar v_F \sqrt{\pi |n_{\text{in/out}}|}$ is the band offset applied on the incoming/outgoing lead ($x < 0\,\text{nm}$ and $x > 625\,\text{nm}$).

The potential profile for a realistic smooth *p-n* interface is defined by electrostatic gating. This causes a non-linear potential profile, unlike the one given in Equation 2.22. The angle-dependent transmission probability will differ from Equation 2.23 for such a profile. In addition, Equation 2.23 is only valid for a symmetric potential. We therefore model the transmission probability of a realistic *p-n* junction created by electrostatic gates (similar to the device shown in Chapter 7) using tight-binding theory as described in Section 2.3. The realistic potential $V(x)$ is obtained from electrostatic simulations which are provided throughout this thesis by our collaborator Ming-Hao Liu from the University of Regensburg.

The results are plotted in Figure 2.6, where the red curves correspond to a smooth potential step and the gray ones to a sharp one, which was calculated to check consistency with Equation 2.21. The $t(\theta)$ curves shown in Figures 2.6a and 2.6c ac-

count for symmetric and asymmetric *p-n* junctions, respectively, and are obtained in the same way as Reference 39. In the symmetric case of Figure 2.6a,b with $n_{\text{in}} = -n_{\text{out}} = 10^{11}\,\text{cm}^{-2}$, the transmission curve for the abrupt case corresponds to the well-known expression [38], $t(\theta) = \cos^2(\theta)$, which drops to one half at $\pm 45°$, while for the smooth case of our device t drops to one half at about $\pm 14°$. In the asymmetric case of Figure 2.6c,d with $|n_{\text{in}}| < |n_{\text{out}}|$, the peak of $t(\theta)$ is slightly broadened since the wavelength in the left cavity is larger.

Due to the strong suppression of large angles, smooth *p-n* interfaces act as rather efficient angular-filters or collimators. These collimators can be used to create planar waves in graphene, but they also enhance the visibility of Fabry-Pérot oscillations and make guiding of electrons in a waveguide possible, as it will be discussed later.

2.2.4. Conductivity of a pn-junction
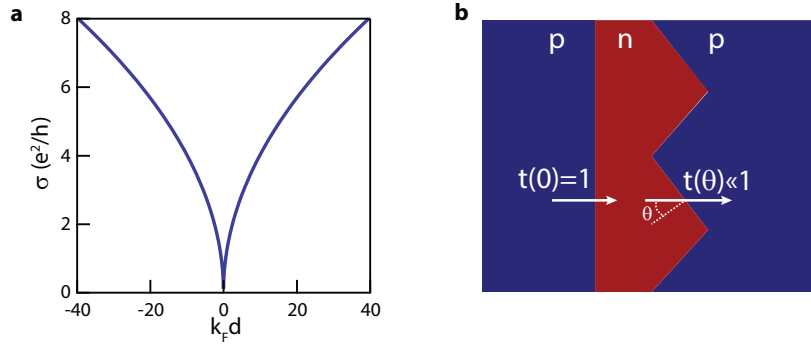
Figure 2.7.: **a**, Conductivity per unit width of an ideal, smooth *p-n* interface. **b**, Proposal for an efficient field-effect transistor using *p-n* interfaces [40].

The transmission of a sharp and smooth *p-n* junction has been given in Equations 2.21 and 2.23. The conductance per unit width is found by averaging the transmission over the angles:

$$g_{pn} = \frac{4e^2}{h} \int_{-\pi}^{\pi} \frac{d\theta}{2\pi} k_{\text{F}} \cos(\theta)^2 = \frac{4e^2}{h} \frac{k_{\text{F}}}{2} \tag{2.24}$$

In contrast, the transmission at the smooth interface exponentially depends on k_{F}. The conductance per unit width g is then [38]:

$$g_{pn} = \frac{4e^2}{h} \int_{-\pi}^{\pi} \frac{d\theta}{2\pi} k_{\text{F}} e^{-\pi k_{\text{F}} d \cdot \sin(\theta)^2} \approx \frac{2e^2}{\pi h} \sqrt{\frac{k_{\text{F}}}{d}} \tag{2.25}$$

This is valid for a wide junction where scattering at the edge of graphene can be neglected. In Figure 2.7a, the conductivity is plotted as a function of the dimensionless parameter $k_{\text{F}}d$. In a real device, σ does not drop to zero for $k_{\text{F}}d \to 0$. For electrons reaching the *p-n* interface under zero incidence angle ($t(0) = 1$), transport through evanescent modes between the contacting electrodes is possible. This is explained in

more detail in Chapter 3.2.1. A possibility to lower the conductivity minimum of such a realistic device using *p-n* interfaces has been discussed in Reference [40]. It was proposed to create a series of tilted *p-n*-p junctions, as shown in Figure 2.7b. The first *p-n* interface transmits, especially if it is smooth, only trajectories close to zero incidence. These trajectories will be reflected by the second, tilted *n-p* interface. Such a design could be used as an efficient graphene field-effect transistor.

2.2.5. Fabry-Pérot cavity
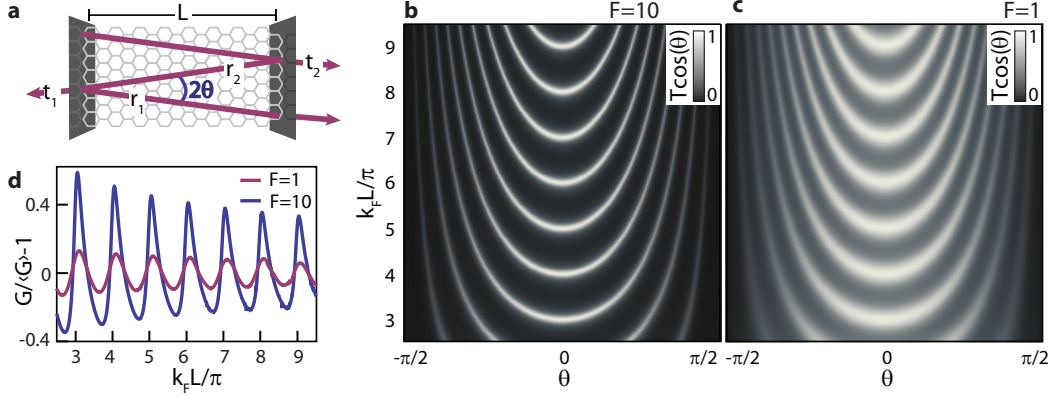
Figure 2.8.: **a**, Sketch of an idealized graphene-based Fabry-Pérot resonator. **b**, Intensity plot of the transmission $T \cdot cos(\theta)$ as a function of the dimensionless parameter $k_F L/\pi$ and angle of incidence θ for a finesse $F = 10$ and **c**, $F = 1$. **d**, Normalized conductance $G/\langle G \rangle - 1$ through an ideal graphene cavity as a function of $k_F L/\pi$ for $F = 1$ in purple and $F = 10$ in blue.

An optical Fabry-Pérot resonator consists of two partially reflective mirrors that form a cavity. The electromagnetic waves interfere constructively or destructively inside the cavity, depending on their wavelength $\lambda = 2\pi/k_F$ and the cavity size L. By changing one of the two parameters, the intensity of the light coupled out of the cavity is modulating. In solid state physics, a corresponding electronic interference pattern can be measured e.g. in a 2DEG with partially reflective contacts.

In a ballistic graphene cavity, as sketched in Figure 2.8a, the phase difference between two successive outgoing rays is $\Delta\phi = 2k_F L \cos(\theta)$. Summing over all partial outgoings waves, one obtains for the transmission probability:

$$T(\theta) = \frac{1}{1 + F \sin^2(\Delta\phi/2)}, \tag{2.26}$$

where $F = 4|r_1||r_2|/|t_1|^2|t_2|^2$ with $|r_{1,2}|$ and $|t_{1,2}|$ the reflection and transmission amplitudes at the two interfaces. F is a measure of the quality factor and known as finesse. The finesse of an FP interferometer determines the visibility of the interference pattern, i. e. the difference in T between constructive and destructive

interference relative to the mean transmission probability. The visibility is very close to unity if $F \gg 1$, and it is small and given by F in the opposite limit. Equation 2.26 is plotted in Figure 2.8b which shows a 2D plot of $T(\theta)\cos\theta$ as a function of θ and the dimensionless parameter $k_F L/\pi$ with finesse $F = 10$, and $F = 1$ in Figure 2.8c.

Since the electric measurement of the two-terminal conductance cannot distinguish the direction of the waves within the cavity, one has to integrate over the angles to deduce the expected conductance. The normalized dimensionless conductance

$$G/\langle G \rangle - 1 = \frac{1}{2} \int_{-\pi/2}^{\pi/2} T(\theta)\cos(\theta)d\theta - 1 \qquad (2.27)$$

is shown in Figure 2.8d as a function of the dimensionless parameter kL/π for $F = 10$ and $F = 1$. $\langle G \rangle$ is the mean value or the background conductance of the plotted range. For both cases, resonances appear equidistantly whenever $k_F L$ is a multiple of π, indicating that the conductance peaks are mainly due to electrons at small incidence angles. The low finesse cavity has a much higher background conductance since $t_{1,2}$ are larger, but the visibility is lower. The visibility is defined as:

$$\frac{\Delta G}{\langle G \rangle}, \qquad (2.28)$$

with $\Delta G = G_{\max} - G_{\min}$, the difference between oscillation peak and dip. For $F = 1$ the visibility is roughly 20% but for $F = 10$ it reaches close to 100% at low k_{F}. Therefore, the visibility measures the quality of the Fabry-Pérot etalon.

2.2.6. Fabry-Pérot cavity created by *p*-*n* interfaces

In the case of an FP cavity created by *p-n* interfaces, the reflection and transmission amplitudes at the two interfaces are angle dependent. In the case of sharp *p-n* interfaces ($k_F d \ll 1$ with d the width of the interface), the transmission probability is $|t|^2 = \cos^2\theta$ (Equation 2.21). This leads to a finesse $F = 4(1 - \cos^2\theta)/\cos^4\theta$. Figure 2.9a shows a 2D plot of the transmission through such a FP cavity as a function of θ and the dimensionless parameter $k_F L/\pi$. For a smooth interface $k_F d \gg 1$, the transmission probability is $|t|^2 = e^{-\pi k_F d \sin^2\theta}$ as given in Equation 2.23. Figure 2.9b shows the same kind of plot as Figure 2.9a for a smooth interface with $d = 300$ nm. The visibility is roughly 20% for the smooth interface and only 0.2% (for $k_{\mathrm{F}}L/\pi < 4$) for the sharp one, as given in Figure 2.9c. In other words: The quality of the Fabry Pérot interferometer can be drastically enhanced by using smooth *p-n* interfaces that efficiently filter out large angles.

2.3. Theoretical modeling and simulation

In a real device, the local charge carrier density is tuned by control- or gate-electrodes. To model an experimental setup, it is therefore required to link the spatial charge
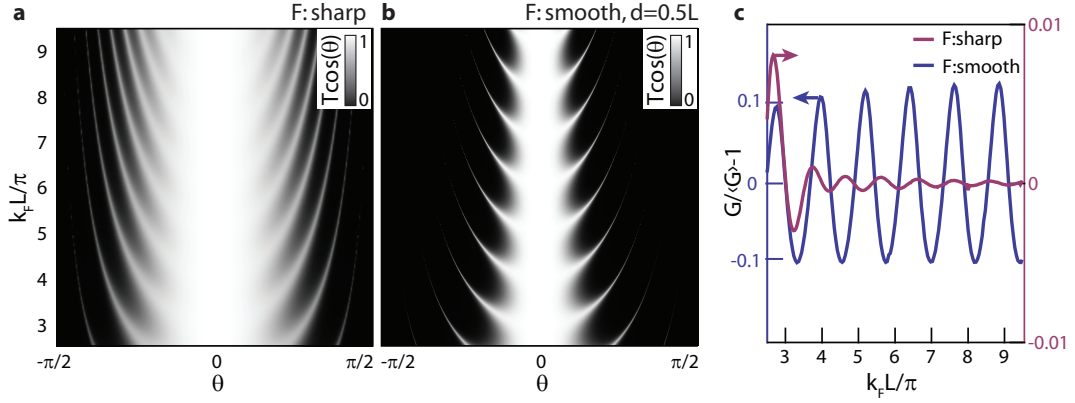
Figure 2.9.: **a**, 2D color plot of $T(k_{\mathrm{F}}L/\pi, \theta)\cos\theta$ for an FP cavity created between two sharp *p-n* interfaces. **b**, Same as **a** for an FP cavity created between two smooth interfaces with $d = 0.5 \cdot L$ **c**, Normalized conductance $G/\langle G \rangle - 1$ as a function of the dimensionless parameter $k_{\mathrm{F}}L/\pi$ for a sharp and a smooth junction. While the conductance oscillates roughly 10% around the mean value for the smooth junction, the oscillation amplitude is only of order 0.1% for the sharp interface (for $k_{\mathrm{F}}L/\pi > 4$).

carrier density to a voltage applied to a gate electrode. In addition, effects of the contact electrodes and the quantum capacitance of graphene need to be taken into account.

2.3.1. A simple capacitance model

In a most simplistic picture, the charge carrier density n can be obtained from a parallel-plate capacitance model. Let us assume that we apply a voltage V to an electrode placed at a distance $d = 600\,\mathrm{nm}$ from a graphene flake. The voltage between two conducting, infinite parallel plates is given by the electric field $E = en/\epsilon$ times d, where $\epsilon = \epsilon_r \epsilon_0$ is the permittivity. In vacuum, $\epsilon = \epsilon_0$ and it follows that

$$n = \frac{CV}{e} = \frac{\epsilon_0}{ed}. \tag{2.29}$$

This simple model is often used to estimate the mobility in the case of uniform gating, but it is not suited to calculate density profiles caused by local gates, and it does not take into account effects of contact doping or quantum capacitance in graphene.

In addition to the classical capacitance C calculated above for the infinite parallel plate capacitor, the quantum capacitance C_{Q} becomes important in graphene [41]. Thus, it is taken into account that applying a voltage to the metallic side of the capacitor will change the electrochemical potential in graphene. By inducing N electrons in graphene, the chemical potential will change by $\Delta\mu = N/\rho$, where $\rho(E)$ is the density of states. This will cause an additional voltage between electrode and

18

graphene, $\Delta V_Q = \Delta\mu/e = N/e\rho = Q/e^2\rho$, and therefore:

$$C_Q = \rho e^2 \ \text{ with } \rho = \frac{4E}{2\pi(\hbar v_F)^2}. \tag{2.30}$$

The density n in graphene by applying a voltage V to a gate is therefore given by

$$n = (C + C_Q) \cdot V/e. \tag{2.31}$$

In order to calculate more complex device geometries, the profile of $n(x)$ is computed by a finite-element-based electrostatic simulator with the quantum correction accounted for through the quantum capacitance model [42], which allows to treat electric, chemical, and contact-induced doping in a unified manner. The detailed methods used by our collaborators are described in the Appendix A.1.

In the devices on LOR described throughout this thesis, we typically apply voltages below $30\,\text{V}$. Due to the large distance between gates and graphene $(400-600\,\text{nm})$, we are always working at low energies, $E < 40\,\text{meV}$, or densities $n < 10^{11}\,\text{cm}^{-2}$.

The densities at the edge of a graphene flake can be a factor of 2 larger than in the bulk if the gate electrode is larger than the graphene, i.e. if there are additional field-lines from the part of the gate electrode that is not below the graphene flake. This is discussed in more detail in Appendix A.2.

2.3.2. Contact Doping

There is an additional voltage V_c arising from the experimentally applied source-drain voltage and the charge transfer from the contact to graphene due to the difference of their work functions. As the measurements are usually performed at low AC-voltages, we may attribute V_c solely to the charge transfer. Since we usually use palladium (Pd) as a contact material, we can compare our results to previous first-principles studies which expect ideal Pd(111) contacts to dope graphene as n-type and may cause a shift of its Fermi level about $\Delta E_F \sim 0.45$ eV, which corresponds to a potential on the palladium contact to be $V_c \sim 1.19$ V [43, 44]. In the experiments in this thesis, however, neither the palladium contact is ideally grown along (111), nor is the graphene/palladium interface clean. Hence, the charge transfer is greatly reduced and the values that correspond to the measured data are typically $V_c \ll 1.19$ V. The doping induced by the contacts is usually p-type and of order $V_c \approx 10^{-2}\,\text{V}$ or $n \approx 7 \cdot 10^{10}\,\text{cm}^{-2}$. The saturation of the field-effect traces between $20-30\,\text{V}$, as it is typically seen in our suspended LOR devices with Pd contacts, is caused by the contact resistance, i.e. the number of available modes provided by the contacting interface is limited.

2.3.3. Scalable Tight Binding Model for Graphene

Here, the simulation method used by our collaborator Ming-Hao Liu from the university in Regensburg is briefly explained, following the argumentation of Reference [45],
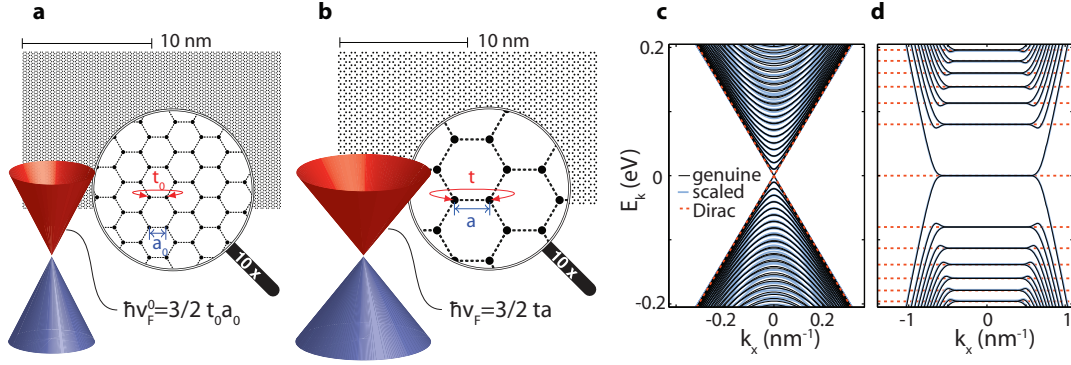
Figure 2.10.: Schematic of a sheet of **a** real graphene and **b** scaled graphene and the low-energy band structures. **c**, Band structure consistency check using an armchair graphene nanoribbon with a width of 200 nm. Here, genuine graphene with $s_f = 1$ is compared to scaled graphene with $s_f = 4$, corresponding to chain numbers $N_a = 800$ and $N_a = 200$ respectively. **d**, Same comparison for an additional perpendicular magnetic field of $B = 5\,\text{T}$.

where also the figures have been adapted from.

Transport properties of real graphene can be modeled using "artificial graphene", which is a honey-comb lattice with scaled bond length a and a reduced hopping energy t, as depicted in Figure 2.10a-b. This scaling is valid as long as the band structure in the relevant energy range remains unchanged. Tight-binding transport is described with the Hamiltonion of Equation 2.7. The linear dispersion $E(\boldsymbol{k}) = \pm \hbar v_F |\boldsymbol{k}|$ is written in terms of the tight-binding parameters as $t_0 \approx 2.8\,\text{eV}$ and $a \approx 0.142\,\text{nm}$

$$E_0(k) = \frac{3}{2} t_0 a_0 k \tag{2.32}$$

for real graphene. To keep the band structure unchanged while scaling up the bond length by a factor s_f, the hopping energy has to be changed accordingly:

$$a = s_f a_0, \quad t = t_0 / s_f. \tag{2.33}$$

This is valid if the band structure is linear, which is true as long as the wavelength is much larger than the lattice spacing: $\lambda_F \gg a$ which implies

$$s_f \ll \frac{3 t_0 \pi}{|E_{\text{max}}|}, \tag{2.34}$$

with E_{max} the maximal energy of interest. For the low carrier densities in suspended graphene with $n < 10^{12}\,\text{cm}^{-2}$, this allows for a very large scaling range with $s_f \ll 264$. In a magnetic field, the magnetic length $l_B = \sqrt{\hbar/eB_z}$ must remain larger than a

which leads to the second restriction:

$$s_f \ll \frac{l_B}{a_0} \approx \frac{180}{\sqrt{B_z}}. \tag{2.35}$$

An example is given in Figures 2.10c+d for a 200 nm wide armchair nanoribbon with $s_f = 1$ and $s_f = 4$, where the genuine and the scaled nanoribbon are very consistent in the given energy range at $B_z = 0\,\text{T}$ and $B_z = 5\,\text{T}$.
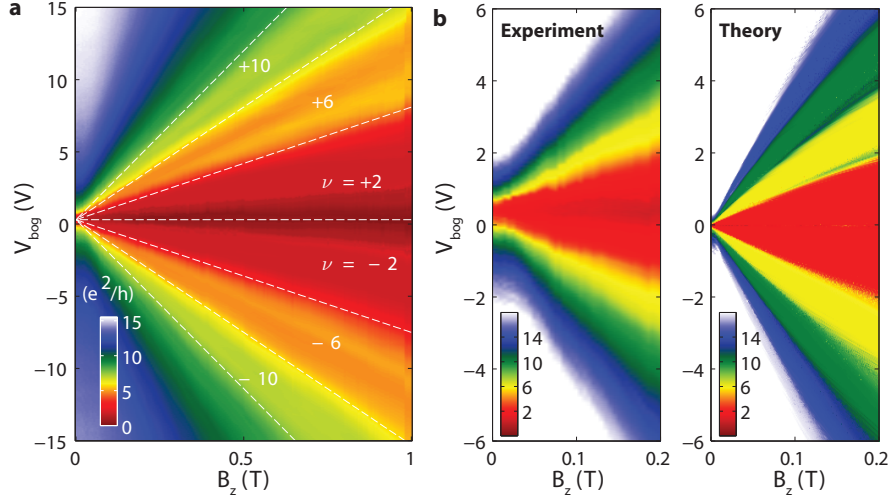
Figure 2.11.: **a** Experimental data of two-terminal conductance of a suspended graphene flake of size $2 \times 2\,\mu$m as a function of gate voltage V_{bog} and magnetic field up to 1 T. The lowest quantized plateaus are labeled by the filling factors $\nu = \pm 2, \pm 6, \pm 10$. **b** Comparison of the experimental data at low field with the theory data for $s_f = 50$

This scaling model has been applied to capture the Fabry-Pérot maps in Chapters 6 and 7 and the magnetic field behavior in Chapter 6. In Figure 2.11, we compare experimental and theoretical quantum Hall data of a sample of size $2 \times 2\,\mu$m. The Landau fan diagrams of experiment and theory in Figure 2.11b are rather consistent. For the calculation, $s_f = 50$ and a low Anderson-type disorder potential with strength $U_{\text{dis}} = 3\,\text{meV}$ is used.

The great advantage of the scaling technique is that it allows to compute real-sized graphene devices while keeping the computation time affordable. Taking the illustrated sample, the computation time is $\Delta t \approx 2.4\,\text{s}$ on a single Intel Core i7 CPU for $s_f = 100$ and about a month for $s_f = 1$.

3

When is graphene clean?

The wave-nature of electrons becomes visible only if scattering is sufficiently reduced. In order to realize electron-optic experiments, extremely clean materials are required therefore. In graphene, such quality has been achieved in several recent experiments, like transverse magnetic focusing [46, 47], the observation of superlattice effects [48], the complex ground-state structure of bilayer graphene [49, 50] and the observation of the fractional quantum Hall effect [51, 52]. In this context, "very clean" means, that the transport is ballistic over the corresponding length-scale. For the electron-optical phenomena discussed in Chapter 2, this requires ballistic transport between the contact electrodes i.e. on μm-length-scales. Once such quality is achieved, two related questions become important: "what are the cleanest devices we can possibly make" and "what is the best way to compare devices that are fabricated differently or that are designed in a very different way?" In this chapter, we try to address these questions.

3.1. What limits device quality?

Scattering in graphene can be caused by extrinsic or intrinsic sources. It is known from early SEM studies, that exfoliated graphene has very few crystalline defects [53]. While such defects can be of importance for CVD-grown graphene they are negligible if exfoliated graphene is used for fabrication [54]. As the most important factor limiting device performance, charged impurities in the substrate or on top of the graphene layer were identified [31, 55, 56]. At low densities, these impurities cause electron-hole puddles which are responsible for charge-carrier scattering.

The community has developed two distinct pathways to circumvent these problems. Nowadays, a large part of the graphene community is using stacks of graphene/hexagonal boron nitride (h-BN) [54, 57–62] to obtain high-mobility devices. Due to the encapsulation of the graphene layer between crystalline h-BN layers, which have a very low amount of charged impurities, scattering is reduced to the extend that ballistic transport over μm-length-scales becomes feasible. Alternatively, extrinsic fluctuations can

be reduced drastically by suspension and in-situ current annealing of graphene [63,64]. Due to the very high temperatures during annealing, residual dopants evaporate. Several recent experiments show that the quality of freely suspended devices fabricated either by under-etching graphene on SiO_2 [63] or obtained by the method first proposed by Tombros et. al. [65] is equivalent or even higher than for graphene encapsulated in h-BN [66,67].

The limitations of device performance are of different origin for suspended and for encapsulated graphene. The encapsulated structures tend to have bubbles at the graphene-h-BN interface. Even though the amount of bubbles can be drastically reduced by optimizing the transfer technique [68], it appears to be extremely difficult to get completely rid of them. In addition, impurities, once encapsulated, cannot be removed anymore. Furthermore, recent studies suggest that the quality of these devices is ultimately limited by strain fluctuations due to wrinkles [69,70]. However, if h-BN and graphene are aligned with high precision [71], Moirée super-lattice effects are present [48,72] which can be exploited, among other possibilities, to study the fractal spectrum of Hofstadter's butterfly [73,74] or creating valley-Hall currents [75].

The problems are of different origin in suspended graphene devices. Since current-annealing is done in situ as a very last fabrication step, no special care during fabrication is needed. But suspended devices often suffer from very non-uniform cleanliness. While ballistic transport might be possible in some regions, others remain highly doped. The non-uniformity of cleaning is due to local variations of heat dissipation during current annealing since the contacts act as heat sinks. As a consequence, regions close to the leads often remain dirty. For the two-terminal devices presented in Chapter 5 and 6, there was no evidence of remaining residues close to the contacts. But non-uniformity of cleanliness is of importance for the four-terminal devices in this thesis (Chapter 7 and 8).

At higher temperatures, flexural phonons [76] limit the mobility of suspended graphene. Even though electron-phonon scattering is expected to be weak in graphene since the phonon frequencies are very large [77], the out-of plane vibrations occur at low-enough frequencies. The phonons cause ripples at which elastic scattering occurs [78]. The resisitvity due to flexural phonons rises with T^2, since, for symmetry reasons, always two phonons are involved in scattering. Even though electron-phonon scattering is not the limiting factor at temperatures below 10K, it restricts the mobility to few $10'000 \, \mathrm{cm^2 V^{-1} s^{-1}}$ at room temperature. Straining graphene by only 0.1% is predicted to yield a dramatic improvement of room-temperature mobility of suspended samples.

Finally, suspended devices are more delicate to handle than encapsulated ones. The complexity of contacting structures and the size of the suspended region are limited by the mechanical stability of graphene. For this reason many research groups fabricate encapsulated devices nowadays.

3.2. Characterization methods

3.2.1. Conductance of a ballistic graphene wire
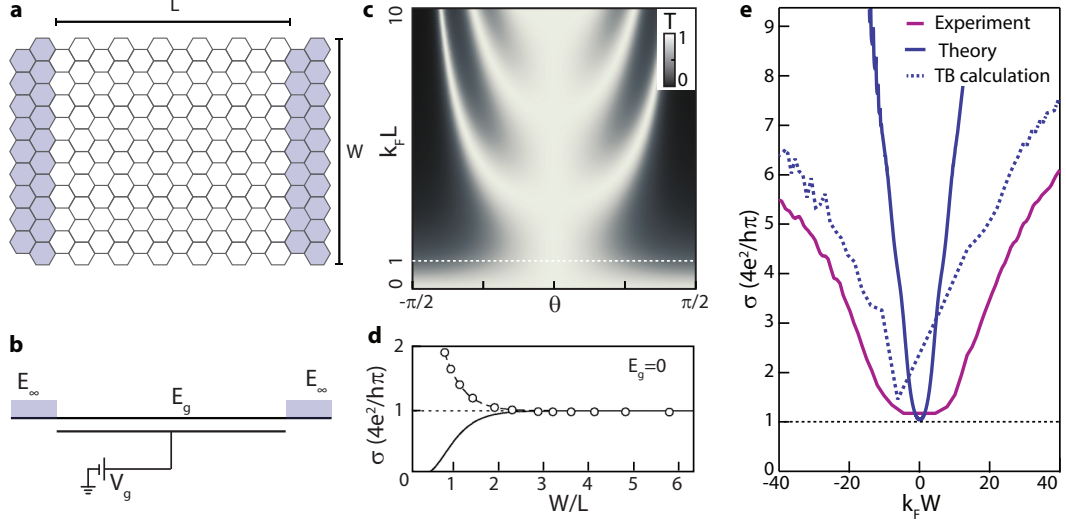
Figure 3.1.: **a**, Model to calculate the two-terminal resistance of a flake with width W and length L. The leads are shaded blue. Adapted from Reference [79]. **b**, The energy E_g in the central part of the flake is tuned by applying a voltage V_g on a capacitively coupled gate. The lead energy $E_\infty \gg E_g$ is large and remains unchanged by the V_g. **c**, Calculated $T(\theta)$ for $W = L$ using Equation 3.1. **d**, Conductivity σ as a function of aspect ratio W/L for a smooth edge (solid curves) and metallic armchair edge (data points from numerical calculation), adapted from Reference [79]). **e**, Comparison of $\sigma(k_F W)$ for experiment (purple), analytical theory (blue) and tight-binding calculation (blue dashed). The experimental data is taken from Chapter 6. For the tight-binding calculation a contact resistance $R_c = 1.45\,\text{k}\Omega$ has been taken into account.

A way to test the quality of the device is by comparing measurements to theoretical expectations for ballistic graphene. The conductance of a graphene wire was calculated by Tworzydło et. al in the context of describing its Fano factor [79]. There are two kinds of boundary conditions that need to be set. First, the contacting leads consist of highly doped graphene. These regions (shaded blue in Figure 3.1a-b) are not tuned by a gate voltage due to the large screening effect of the metallic contacts. The transmission between left and right lead T is then calculated in the framework of Klein tunneling, assuming a large potential $E_\infty \gg E_g$ in the leads and a finite, gate-tunable E_g in the middle part. The minimum conductivity is therefore limited by reflections in the contact region, at least if the width W is clearly larger than the length L of the measured graphene wire. If this is not the case, the transmission

will depend on the second boundary condition, i. e. how the upper and lower edge in the middle region are modeled. This can be easily understood since, close to the Dirac point, the electronic wavelength becomes larger than the sample width and the transport through these evanescent modes is extremely sensitive to the type of edges involved.

The transmission for an infinite amount of modes in the leads assuming smooth edges (i. e. edges of infinite mass that do not mix the pseudospin) is [79]:

$$T(k_y) = \frac{2k_x^2}{2k_x^2 + k_y^2 \left(1 - \cos(2k_x L)\right)}, \tag{3.1}$$

where $k_x^2 = \sqrt{k_F^2 - k_y^2}$. $|T|$ is plotted in Figure 3.1c as a function of incidence angle θ, with $L = 1$. At the Dirac point, there is still a finite transmission through evanescent modes for $k_F L < 1$. At higher k_F, constructive or destructive interferences lead to resonant peaks and dips depending on the angle of incidence. This Fabry-Pérot pattern has been discussed in Section 2.2.5.

The conductance is given by summing over the m modes in the lead, $G = 2e^2/h\sum_m T_m$. For a wide junction $W/L > 2$, the summation over the transverse modes can be replaced by the integral

$$G = \frac{4e^2}{h} \frac{W}{\pi} \int_0^\infty dk_y T(k_y), \tag{3.2}$$

The conductivity $\sigma = GL/W$ is plotted in Figure 3.1d as a function of the aspect ratio W/L. Here, the circles are calculated using equation 3.1, whereas the black line corresponds to the numerically calculated transmission for an armchair wire. Apparently the two solutions match for $W/L > 2$, i. e. the conductivity does not depend on the boundary conditions for the upper and lower edge anymore. The dependence of σ on E_g is given as the blue curve of Figure 3.1e for an aspect ratio of 1.2. The minimum conductivity in graphene for $W/L > 2$ is:

$$\sigma_{\min} = \frac{4e^2}{h\pi}, \tag{3.3}$$

In diffusive samples, the observed minimum conductance missed the factor of π, which was attributed to the presence of e-h puddles [80, 81]. Figure 3.1e reveals however, that Equation 3.3 is almost met in our devices. In the figure we compare the conductivity given by Equation 3.2 to an experimental curve (from Chapter 6). But, even though the minimum conductance is close to $4e^2/h\pi$, the curves deviate rather strongly for larger k_F. One explanation might be that the transport is not ballistic. Impurity scattering would drastically lower the mobility, which would reduce the slope. However, the ballistic tight-binding calculation (bl ue dashed line in Figure 3.1e) which is calculated based on the geometry of the device, exhibits a similar slope as the experiment if a contact resistance of $R_c = 1.45\,\text{k}\Omega$ is taken into account.[1] As

---

[1]The tight-binding data is not symmetric and does not reach the same minimum as the experiment due to limited resolution

a consequence, the main difference between the experiment and analytical theory is due to deviations in the boundaray conditions. First, the potential at the contact electrodes is not infinite but finite in the real device. Second, $W/L \approx 1$ in the experiment and therefore the edge potential becomes important.

Apparently, the above equations are not well suited to characterize and compare device quality, because Equation 3.2 strongly depends on the boundary condition and the value of Equation 3.3 can also be obtained if the current in the device is flowing through a resistor in series and/or in parallel to the cleaned region. Such a resistance could be the contact resistance (R in series), it could be due to *p-n* junctions in series or due to paths through highly doped graphene caused by non-uniform cleaning (R in parallel).

3.2.2. *p-n* interfaces
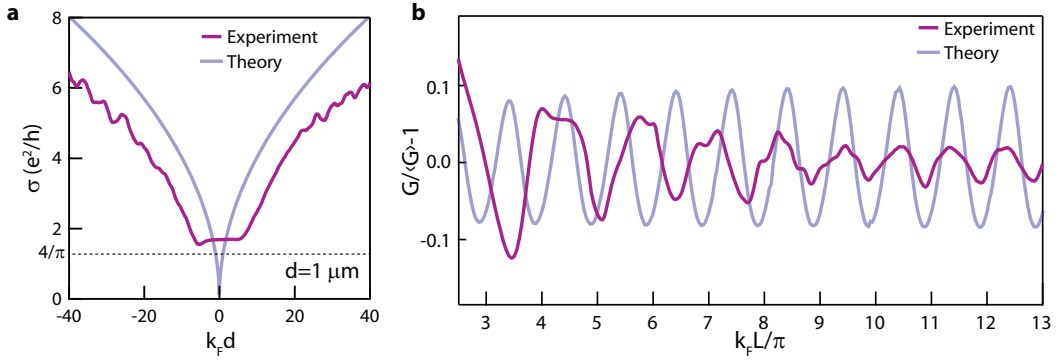
Figure 3.2.: **a**, Comparison of theoretical (Chapter 2.2.4) and experimental (Chapter 6) conductivity as a function of $k_F d$, where d is the smoothness of the junction (here, $d = 1\,\mu\text{m}$). **b**, Fabry-Pérot oscillations of a *p-n-p* device, where $G/\langle G\rangle - 1$ corresponds to the conductance oscillations around a mean value $\langle G\rangle$ as in Chapter 2.2.5. The experimental curve is taken from Chapter 5.7.

Using *p-n* interfaces, a much better comparison between analytical theory and experiment is possible, since the boundary condition which dominates the problem, i. e. the *p-n* interface, is well defined in contrast to the poorly controlled and characterized boundary conditions given by the edge of graphene or by metallic contacts.

First, we compare the analytical formula for the conductivity of a smooth *p-n* junction (Equation 2.25 and Figure 2.7a) to the measured conductivity of the device mentioned above (Chapter 6) in the *p-n* regime. These two curves are plotted in Figure 3.2a without using any fit parameters. The difference at low $k_F d$ is due to coupling of evanescent waves between two contacts in the real device, which yields the minimum conductivity close to $4e^2/h\pi$ discussed above (Chapter 3.2.1). Otherwise,

the curves match well given the simplicity of the analytical model. This clearly indicates that the transport in this smooth *p-n* junction (where the region of smoothness is $d = 1\,\mu$m long) is described by ballistic trajectories.

Moreover, conductance oscillations visible on the experimental curve of Figure 3.2a are signatures of Fabry-Pérot interferences over the full length of graphene, i. e. the electrons are bouncing back and forth between contacts and do not scatter in-between. These oscilllations, which are described in more detail in Chapter 5, yield the best prove for ballistic transport over large flake areas. Here, we compare Fabry-Pérot oscillations in the middle region of a *p-n-p* device to analytical results. In Figure 3.2b, $G/\langle G\rangle - 1$, corresponding to the conductance oscillations around a mean value $\langle G\rangle$ as in Chapter 2.2.5, is plotted as a function of $k_F L/\pi$. The experimental curve is taken from Chapter 5.7. For larger values of $k_F L/\pi$, the periodicity of experimental and theoretical calculations matches, whereas a deviation for lower values is observed. This is due to a changing cavity length L at low gate voltages as e. g. the simulations in Appendix A.1 reveal. The oscillation amplitude is close to the theoretically expected value of $\approx 10\%$.
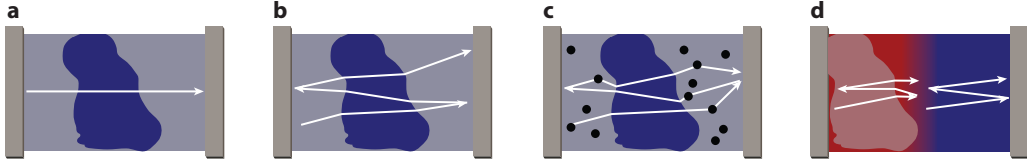
Figure 3.3.: Comparison of different characterization methods. **a**, The dark blue region of graphene is clean and the light gray region is highly doped. If the conductance between the two contacts is measured and the cleanliness of graphene is characterized only by how strong the Dirac dip is and how close to zero gate voltage it occurs, it will appear to be clean. **b**, However, no regular Fabry-Pérot pattern can occur. **c**, The situation is even worse in the situation of a clean region in the middle and a strongly varying potential outside. The additional scatterers (black dots) will completely destroy any regular Fabry-Pérot pattern, however, a high resistance at zero gate voltage can still be observed. **d**, By using local gates, information about the local cleanliness can be extracted, i. e. in the depicted situation, a regular Fabry-Pérot pattern can be observed in the right cavity but not in the left one.

In fact, the Fabry-Pérot measurements shown in Chapter 5 yield an excellent proof for ballistic transport over large flake areas. In the case of suspended graphene, polymer residues tend to accumulate close to the metallic contacts, leading to large puddles as shown in Figure 3.3. Such large-scale puddles also may exist in the case of graphene that is encapsulated between hBN. There, the puddles mostly originate from bubbles between graphene and hBN, and those bubbles are very difficult to

avoid in the fabrication process. In both cases, it is usual that clean and dirty regions coexist.

We suppose that there is a clean region in the middle of graphene (blue area in Figure 3.3a) and a highly doped region outside (light gray). Even though large areas of the graphene flake are not clean, one will observe a Dirac-point at zero gate voltage. This Dirac point can be deep and steep, since the middle region will dominate the resistance at low voltages. One would therefore conclude that graphene is very clean and has a high mobility. Yet, the Fabry-Pérot interference pattern originating from oscillations as sketched in Figure 3.3b will be irregular. The situation is even worse if one assumes large potential variations in the outer regions. They will not affect the position of the Dirac point, nor its depth. But if we regard these fluctuations as scattering centers (black dots in Figure 3.3c), they will completely destroy any regular Fabry-Pérot pattern.

By studying the interference patterns tuned by local gates, additional information can be obtained. E. g. the situation sketched in Figure 3.3d will reveal a regular interference pattern in the right cavity, but an irregular pattern in the left one. Therefore, one gains local information about the cleanliness. This is a particular importance for multi-terminal devices, where different annealing paths can be chosen.

3.2.3. Commonly used numbers
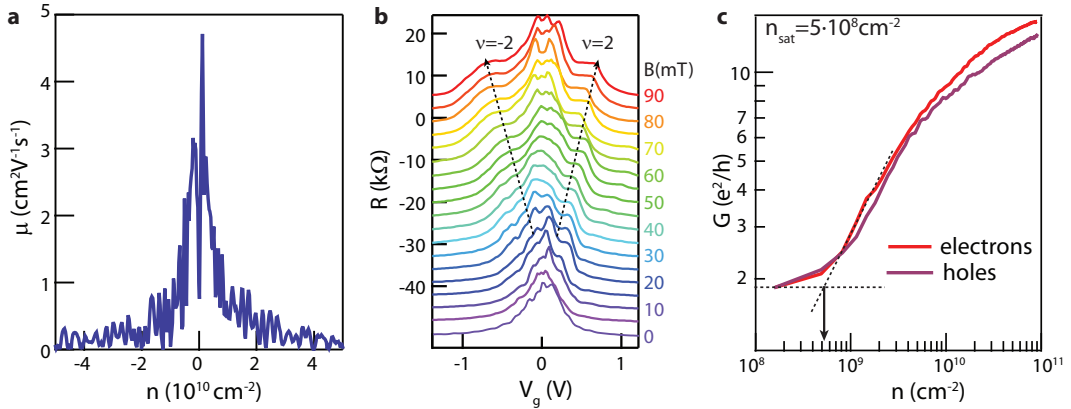
Figure 3.4.: **a**, Mobility calculated from field-effect measurement (Equation 3.4) for the sample of Chapter 6. **b**, $R(V_g)$ for small magnetic fields shows the onset of SdH oscillations at $10\,\mathrm{mT}$, corresponding to $\mu \approx 1 \cdot 10^6\,\mathrm{cm^2V^{-1}s^{-1}}$, and fully developed quantum Hall plateaus at $40\,\mathrm{mT}$. **c**, The saturation density for the same sample n_{sat} is extracted in a log-log plot of $G(n)$. n_{sat} is of order $\delta_n \approx 5 \cdot 10^8\,\mathrm{cm^{-2}}$ for both the electron and the hole side.

Finally, we compare the quality of the above mentioned device from Chapter 6 to

numbers that are typically given throughout the literature for device characterization. However, these numbers again strongly depend on device geometry and measurement setup, since scattering at the graphene edges and the contacts become important at low densities, when the Fermi wavelength is comparable to the geometric dimensions. Due to the very different fabrication methods and the geometrical constraints, it is difficult to really compare the device quality.

Most commonly, the mobility μ extracted from the field-effect $\sigma(n)$ curves

$$\mu = \frac{1}{e}\frac{d\sigma}{dn}, \tag{3.4}$$

is used for comparison. Typical values are $\mu \approx 3 \cdot 10^3\,\mathrm{cm^2V^{-1}s^{-1}}$ on SiO$_2$ [25], $\mu \approx 5 \cdot 10^5\,\mathrm{cm^2V^{-1}s^{-1}}$ for encapsulated graphene [54, 82] and $\mu \approx 1 \cdot 10^6\,\mathrm{cm^2V^{-1}s^{-1}}$ for suspended devices [83]. The devices in this thesis exhibit field-effect mobilities in the order of $\mu = 2 - 7 \cdot 10^5\,\mathrm{cm^2V^{-1}s^{-1}}$ if extracted with the above equation. In Figure 3.4a, the mobility for the device of Chapter 6 is given, having a maximum of $\mu = 4.7 \cdot 10^5\,\mathrm{cm^2V^{-1}}$.

A more reliable way to extract μ was outlined by Mayorov et.al. [84] by looking at the magnetic field B_q at which Shubnikov-de Haas (SdH) oscillations first appear. SdH oscillations occur once the small-angle scattering time τ_q times the cyclotron frequency ω_c is 1, i. e. oscillations become visible once cyclotron orbits can be completed before scattering occurs [85]. Therefore, the mobility can be extracted by:

$$\mu B_q = \omega_c \tau_q = 1 \tag{3.5}$$

The above formula is obtained by the Drude model for $\sigma = en\mu = ne^2\tau/(\hbar k_F/v_F)$ and the cyclotron frequency in graphene $\omega_c = eB/(\hbar k_F/v_F)$. As shown in Figure 3.4 the SdH oscillations are slightly visible at 5 mT and certainly visible at 10 mT which yields a mobility of $\mu \approx 1 \cdot 10^6\,\mathrm{cm^2V^{-1}s^{-1}}$ for the latter case. A flat Quantum Hall plateau can be seen already at 30 mT. In this thesis, B_q is in the order of 10 mT for all devices. Such high mobility is in agreement with the observation of a regular Fabry-Pérot pattern as it is present in the devices described in Chapters 5, 6 and 7, but, for geometrical reasons, not in the bilayer-device in Chapter 8.

Alternatively, one can extract the amount of residual dopants δn from the width of the Dirac peak, which is of order $\delta_n \approx 5 \cdot 10^{10}\,\mathrm{cm^{-2}}$ on SiO$_2$ [86], $\delta_n \approx 5 \cdot 10^9\,\mathrm{cm^{-2}}$ on h-BN and $\delta_n \approx 5 \cdot 10^8\,\mathrm{cm^{-2}}$ for the cleanest suspended devices [84]. As shown in Figure 3.4a, where $\sigma(n)$ is given in a log-log plot, the residual doping of one of the samples in this thesis (Chapter 6) is with $\delta_n \approx 5 \cdot 10^8\,\mathrm{cm^{-2}}$ among the best devices reported so far. This sets an energy scale of 3 meV, which means that above only 30 K, the width of the Dirac peak is given by thermal smearing only. In conclusion, the devices we obtain by the method described in the following chapter, are sufficiently clean to observe electron-optical phenomena. Whereas the value for μ calculated with Equation 3.4 is strongly limited by scattering at the boundaries, the observation of a regular Fabry-Pérot pattern, the very low saturation density and the quick onset of SdH oscillations reveal, that our graphene is among the cleanest reported so far.

4
Fabrication

In this chapter we report on our experience in fabricating freely suspended graphene samples. In a first step, the key elements of the method are discussed and the modifications to the original process, which led us to the production of ultra-high quality devices with an excellent yield, are highlighted. We show the possibility to implement local bottom and top gates for these suspended devices. We further discuss the feasibility of the method to fabricate more complex graphene structures like multi-terminal samples or devices with superconducting electrodes. Finally, we analyze the mechanical stability of different suspended structures by using CVD graphene. The methods presented here have been partially published in Reference [87]. Compared to our publication, we extend the information on current annealing and graphene exfoliation and add the sections on superconducting contacts and mechanical stability.

4.1. Suspending Graphene
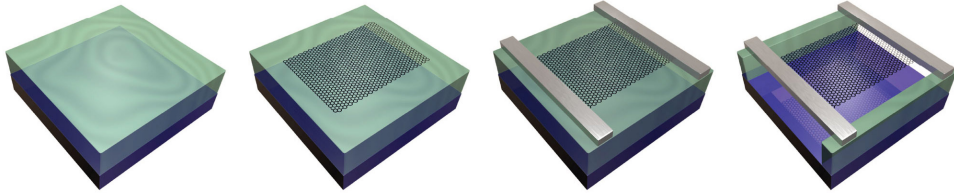
Figure 4.1.: Fabrication of suspended graphene following the method introduced by Tombros et al. [65]. The SiO_2 is colored blue, LOR is shown in green. The final image shows suspended graphene attached to free-standing contacts.

The main idea of the fabrication method proposed by Tombros and coworkers [65, 88] is to use a layer of lift-off resist (LOR)[1] as a sacrificial layer to realize freely suspended graphene devices. Figure 4.1 summarizes this method, and detailed step-by-step recipes can be found in the Appendix B. We start the fabrication by depositing

---

[1]LOR 5A, MicroChem Corp.

a set of numbered markers by standard UV-lithography on a heavily doped Si/SiO_2 wafer. The markers, spaced 200 μm apart from each other, serve for orientation and alignment during the process. Afterwards, we spin-coat LOR on the wafer.

Subsequently graphene is exfoliated from natural graphite with Nitto tape[2] directly onto the LOR surface. The yield of large-area single-layer graphene flakes can be improved by modifying the exfoliation procedure. For this purpose, the Nitto-tape which is already covered with flakes, is put into a freezer, while the LOR-covered wafer is treated in a UV-Ozone plasma for 2-3 minutes. Within very short time, the tape is taken out of the freezer and pressed onto the UV-Ozone treated device. This yields large graphene flakes on Polymer substrates such as LOR and PMMA in a reproducible fashion. For exfoliation on SiO_2, we could not see an improvement of flake size.

No particular care is required for the identification of graphene by optical contrast on the wafer/resist stack, since we use dark-field and Nomarski differential interference contrast (NDIC) microscopy to locate single-layer graphene flakes. NDIC microscopy separates the source light into two orthogonally polarized parts, which are recombined after reflection on the device. The contrast given by the interference of the two polarized parts reveals the edges of the graphene flakes extremely well [89]. In addition, the microscope is equipped with a camera system, which allows digital contrast enhancement of the live microscope image, providing an easy determination of the number of graphene layers. Without the live contrast enhancement, the graphene flakes are barely visible due to the additional layer of polymer between graphene and SiO_2.

Once a suitable graphene flake has been spotted, the contacting structures are realized by e-beam lithography with a 500 nm thick 950K PMMA layer at 20 keV electron acceleration voltage with a dose of 200 $\mu C/cm^2$. For convenience, we design our structures in Adobe Illustrator. Details are given in Appendix B.1. Structures are written in Raith Elphy Plus using an auto-alignment procedure, where we align the design with the actual device using predefined markers. As for Tombros et. al., PMMA development is done with xylene at room temperature. After development, 50 nm of palladium is thermally evaporated in a UHV chamber with the device cooled to -30°C. Lift-off is done with xylene at 80°C, and the sample is rinsed with hexane. We note here that micro-bonding of these samples is difficult, since the wedge tool of the bonder breaks through the bonding pads on the LOR. This problem can be resolved by removing the LOR at the bonding pad position before contact fabrication. To this end we write a step-like structure into the LOR to provide a smooth increase in height for the Pd-wires, and develop this structure in ethyl-lactate for 2 minutes. The steps are written by exposing subsequent areas with decreasing dose (Appendix B.5.2).

To suspend graphene, LOR is exposed using e-beam lithography at 20 keV with a dose of 1100 $\mu C/cm^2$. Due to back-reflected electrons, the 600 nm thick LOR-layer is even exposed below the contacts. Finally, after development of LOR with ethyl-

---

[2]SPV 224P, Nitto Europe NV

lactate for 2 minutes and rinsing in hexane, both graphene and metallic contacts are suspended. This is different from the original method where the contacts remain supported by LOR pillars. An scanning electron microscope (SEM) picture of a device with supported and suspended contacts is given in Figure 4.2a and b respectively. We will show that what we call "full suspension" is crucial for efficient current annealing.

Compared to Tombros and coworkers, we reduced the thickness of the LOR from 1.15 μm to 600 nm in order to increase the back-gate efficiency, i. e. to access higher charge carrier densities. Even with this reduced thickness, suspension remains possible and we found that we can further reduce the LOR thickness to < 400 nm if we rinse the sample in warm Hexane after development. This is possible due to the low viscosity of hexane, which is 0.3 mPa $\cdot$ s at $25\,^{\circ}$C and only 0.19 mPa $\cdot$ s at $75\,^{\circ}$C, compared to the room-temperature viscosity of water (1 mPa $\cdot$ s), ethanol (1.1 mPa $\cdot$ s) or isopropanol (2.1 mPa $\cdot$ s).

4.2. Current annealing
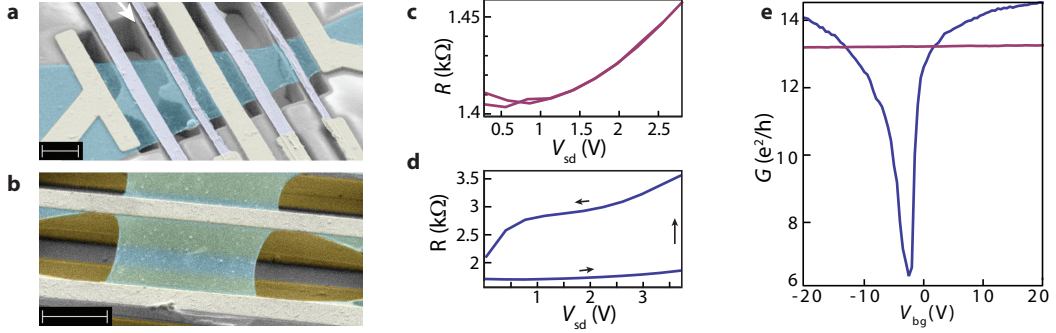
Figure 4.2.: **a**, Scanning electron micrograph (SEM) of a suspended graphene device, where the LOR below the contact has not been removed (highlighted with a white arrow). **b**, SEM image of a device where also the electrodes are free-standing. **c**, Typical current annealing resistance-voltage traces for the first and, **d**, last annealing step. **e** Field-effect of graphene before current annealing (purple), and after the last annealing step (blue).

We performed electronic transport experiments either in a ^{4}He cryostat with a variable temperature insert at low gas pressures <1 mbar, or in a dilution refrigerator, or in a ^{3}He cryostat, depending on the base temperature needed. The current annealing was preformed at 4 K, where the process is better controlled compared to room temperature. Figure 4.2c and d shows current annealing curves for a "fully suspended" device. During annealing, the applied voltage is ramped to a maximum value and back to zero, while the resistance of the flake is recorded. This is done by measuring the voltage drop over a pre-resistor R_{pre}. Depending on whether R_{pre} is

smaller or larger than the sample resistance R_s, the setup is more voltage- or more current-biased. The dissipated power is $P = U^2/R$ in the voltage-biased case and $P = I^2 \cdot R$ in the current-biased situation, respectively. Since we expect that R_s increases when graphene becomes clean, a voltage-biased setup (i. e., $R_\mathrm{pre} < R_\mathrm{s}$) is more favorable. Like this, run-away loops can be avoided, i. e. in the current biased setup, increased R_s would lead to increased power which would result in a positive feedback.

Before annealing, the graphene device displays only a very small field effect as shown by the purple curve in Figure 4.2e, thus indicating strong doping by resist residues from LOR and PMMA. The first annealing curve, shown in Figure 4.2c, displays no hysteresis; the graphene quality remains similar and shows weak gate dependence. The maximum voltage applied during the ramp cycle is slowly increased, and if a resistance difference between the increasing and the decreasing voltage sweep is found, the gate dependence is recorded. The curve in Figure 4.2d shows the last annealing step of the same graphene device, where a huge jump in the device resistance is observed at high voltages. The gate dependence measured after this step is shown in blue in Figure 4.2e and displays a sharp conductance minimum corresponding to the charge neutrality point. The current densities of $\sim\!350\,\mu\mathrm{A}/\mu\mathrm{m}$ needed to clean suspended devices are smaller than values reported for devices with supported contacts [63, 65]. During annealing, graphene heats up, but the contacts remain colder such that residues condensate. When the contacts are also suspended, their cooling power is reduced. This ensures that graphene becomes uniformly clean.

After current annealing, graphene is characterized by measuring the conductance as a function of applied gate voltage, as explained in Chapter 3. The "full-suspension" fabrication allows obtaining ultra-clean graphene devices with a current annealing yield close to 100% for two-terminal devices. These devices are at the state of the art concerning residual doping and ballistic behavior.

4.3. Implementation of bottom gates

For electron-optic experiments, it is essential to be able to tune the charge carrier density locally. This has already been done on supported samples both with bottom and top gates [90–93]. Concerning suspended graphene, implementation of local top and bottom gates remains challenging, even if some realizations are present in the community [94–96].

One possibility to realize local gating is to pre-pattern bottom gates before spin-coating the LOR, as shown in Figure 4.3a. The challenge is now to deposit the desired graphene flake on top of these gates. To do so, we chose a dry transfer technique [54]: graphene is exfoliated onto a separate wafer of $\mathrm{Si/SiO_2}$ with a stack of PVA/PMMA of $50\,\mathrm{nm}/300\,\mathrm{nm}$. Once again, optical localization of single-layer graphene flakes is done by NDIC microscopy, and no specific resist thickness is needed for this. Afterwards, the wafer is placed on the surface of de-ionized water where the PVA layer slowly
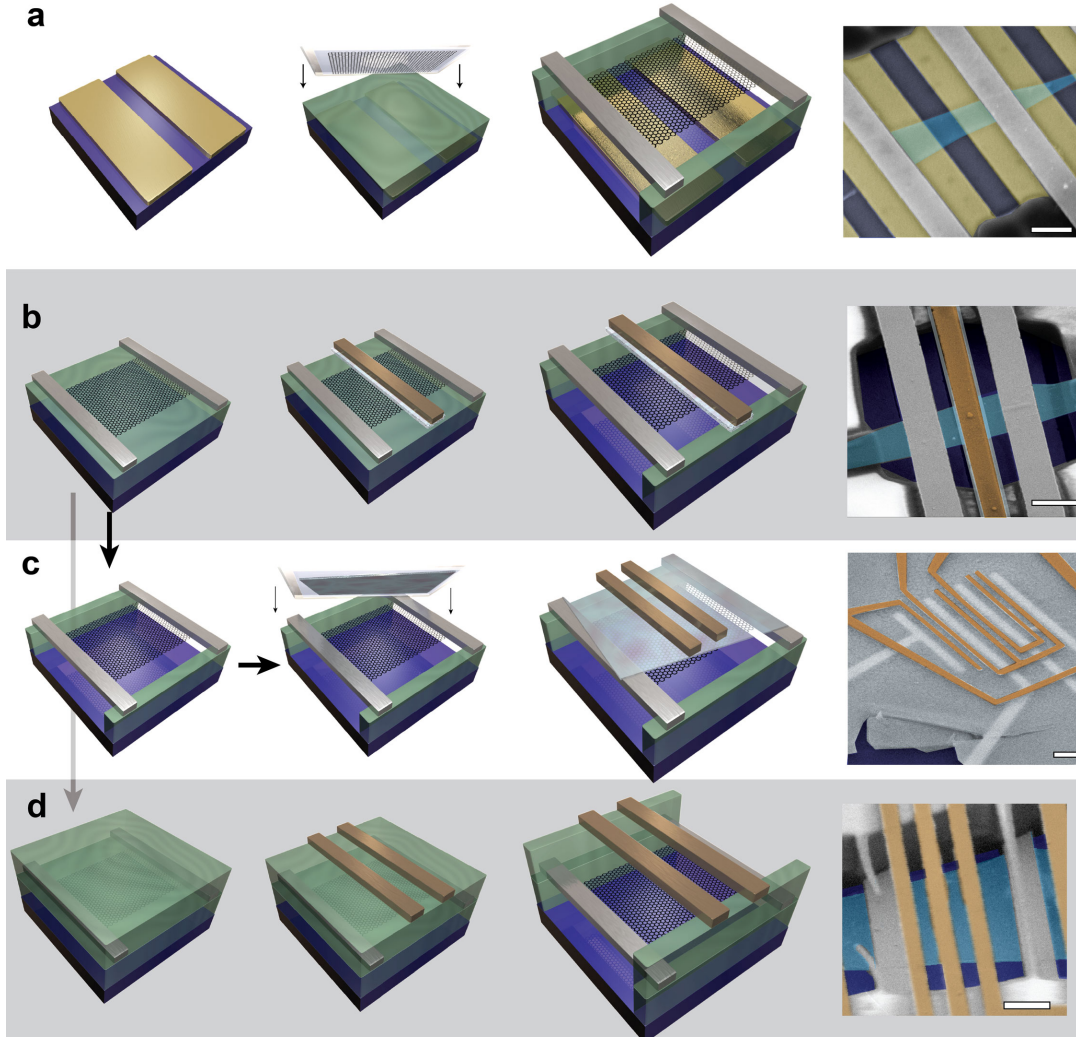
Figure 4.3.: Fabrication of gated structures, where the final images in each row are the false colored SEM images of the finished devices. The scalebar corresponds to $1\,\mu$m, the bottom and top gates are colored yellow and orange, respectively, the contacts gray and graphene light-blue. **a**, Fabrication of suspended devices with bottom gate structures. **b-d**, Fabrication of top gates. **b**, The top gates are separated from graphene with a thin layer of MgO. **c**, An additional layer of hBN is transferred onto graphene on which the gates are patterned. **d**, The graphene is covered with an additional layer of LOR, which is used to suspend the gates.

dissolves. The floating PMMA layer (with the graphene flake on top) is carefully fished out with a glass slide containing a metallic rim (which will support the PMMA layer) and a hole on the glass slide, where the water can flow out [54]. We call this tool "volcano".

If the stack is treated with UVO in order to increase the graphene flake size and quality, the process needs to be modified. First, we replace PVA by Dextrane, since PVA is hardening in UVO and cannot be dissolved in water anymore. Second, the PMMA thickness is increased to $500 - 600\,\mathrm{nm}$ in order to avoid cracking of the layer during the transfer process.
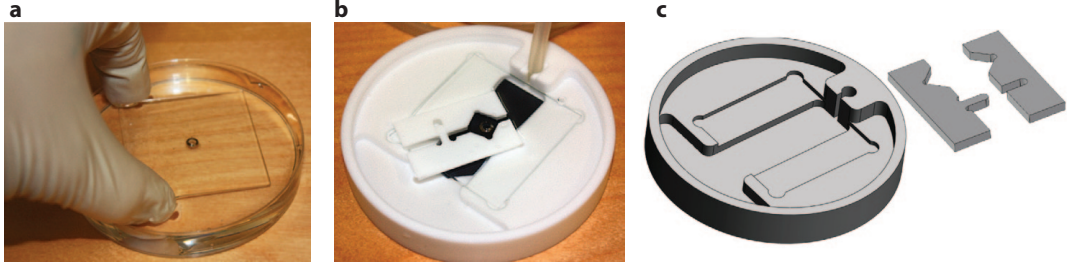
Figure 4.4.: Optimization of the PMMA "fishing" technique **a**, Before we built an adequate tool, we used to manually capture the PMMA/graphene layer, floating on the water, with a glass slide. The glass plate with the metallic rim (diameter $3\,\mathrm{mm}$) is called "volcano". **b**, We currently use a tool where the PMMA skin is fixed between two clamps that can be moved on top of the volcano. Then we pump water out of the bath until the PMMA is attached to the volcano. **c**, CAD image of the bath and the clamps. The tool is made out of teflon.

We optimized the transfer to the volcano by using a tool that facilitates the positioning of the PMMA layer. In Figure 4.4a the non-optimized "fishing"-process is shown, where the glass-plate with the volcano (diameter 3 mm) is moved by hand below the floating PMMA layer and then raised. It is very challenging to place the chosen graphene flake in the middle of the volcano. To improve the yield we designed a tool with which we can fix the position of the glass-slide, clamp the PMMA layer and move it on top of the volcano, as shown in Figure 4.4b. The graphene flake can then be accurately aligned to the middle of the volcano by using a stereomicroscope. Once aligned, water is pumped out from the bath with a pipette. If the PMMA layer is attached to the metallic rim, the clamps are removed and the glass slide can be taken out of the bath. The tools (a CAD picture is shown in Figure 4.4c) are made from teflon. We require a hydrophobic material to avoid that the PMMA attaches to the clamps.

After leaving the PMMA layer to dry overnight, the glass slide is transferred to a modified MJB3 mask aligner or to a transfer stage (as described in Reference [97]) to realize the alignment between the graphene flake and the pre-designed bottom gates

coated with LOR (second sketch of Figure 4.3a). The chip with the bottom gates is heated to 95 °C to avoid any water on the LOR surface and to ease detaching of PMMA from the volcano. Once PMMA is released from the glass slide, the stack is heated to 150 °C. Once graphene is transferred, PMMA is removed in hot xylene and the sample is finished following the previously described method. The last sketches in Figure 4.3a show the finished devices and a false-colored scanning electron micrograph of graphene with local bottomgates.

4.4. Top gates

Alternatively, the carrier density in graphene can be locally tuned by top gates. However, their realization is not straightforward. The most natural way is to grow a dielectric between graphene and the gate electrodes. For this purpose we evaporated 5-10 nm of MgO onto graphene. The design and a false colored SEM image of such a device are shown in Figure 4.3b, where the top-gate is colored orange. We managed to current-anneal the device, with a Dirac point visible in $G(V_{gate})$ similar to Figure 4.2c. However, we found that the yield of current annealing is decreased, because the middle top gate acts as a heat sink. Moreover, the top gates seem to introduce noise, possibly because of trap states in MgO.

Instead of using an evaporated oxide as dielectric, a layered material, e. g. hexagonal boron nitride (h-BN), can act as a spacer. It was shown already that h-BN can be used for top gates in substrate supported samples and that stable gating can be realized [98]. Therefore, we transferred h-BN flakes on top of the contacts of an already suspended device (Figure 4.3c) and fabricated the top gates on h-BN. A false-colored SEM image of a device is displayed in Figure 4.3c where the boron-nitride flake covering the whole structure is colored light blue. We found, however, that the yield of current annealing, similarly to the oxide-defined top gates, decreased significantly. The encapsulation inhibited evaporation of contaminants from graphene and hBN acted as a heat sink during annealing. Although we managed to clean some of the devices, the decrease of the yield suggested looking for a different technique.

The problems of the previous two approaches can be circumvented if the top gates are also suspended above graphene. To this end, after the fabrication of metallic contacts on graphene, another layer of LOR resist (thickness 500-600 nm) is spin-coated onto the device, as shown in Figure 4.3d. This technique was mainly developed by Clevin Handschin at the University of Basel. Between the two layers of LOR, a thin (80 nm) layer of PMMA is added. Without this protection layer the contacts can be deformed during spin-coating of the second LOR layer. Top gates are designed by e-beam lithograph. Finally, the whole device (containing graphene, contacts to graphene and the top gates) is suspended by exposing the suspension mask with a dose of $1100\,\mu\text{C/cm}^2$ and development in ethyl-lactate. An SEM micrograph in Figure 4.3d shows such a device after fabrication, with the top gates displayed in orange. If the gates cover a substantial part of the graphene flake, the suspension

cannot be done in the final lithography step. In this case, the suspension mask is exposed before the fabrication of the top gates, but not developed. To finalize the device, after the lift-off of the top gates, the device is suspended by developing the suspension mask in ethyl-lactate.

The versatility of the fabrication method allows the combination of top and bottom gates to realize complex gated structures. For example, a local perpendicular electrical field to the graphene flake, created by local bottom and top gates, can be used to exploit the different ground states of ultra-clean bilayer graphene [49, 50].

4.5. Multi-terminal devices
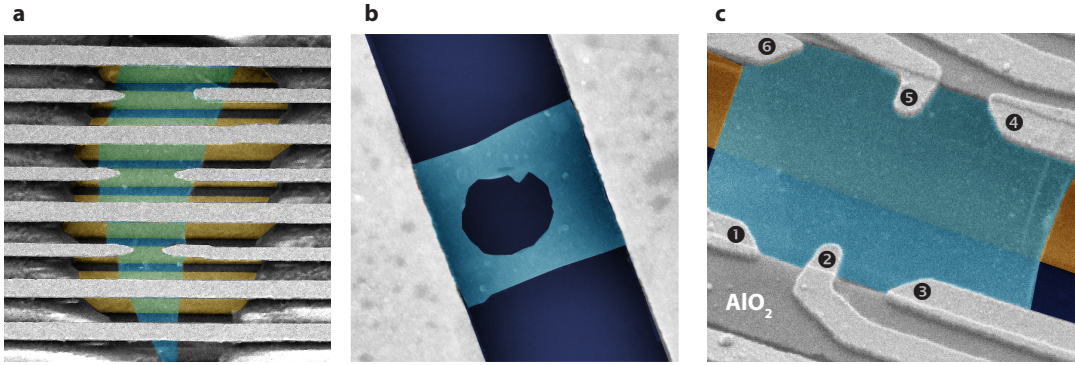
Figure 4.5.: False-colored SEM images of more complicated structures. The scale bar corresponds to $1\,\mu$m. **a**, Multi-terminal device with side contacts and bottom gates. **b**, Suspended Aharonov-Bohm ring, defined by plasma etching. **c**, Multi-terminal device with "finger-shaped" electrodes and bottom gates.

To emphasize the versatility of this fabrication method, we present more complex and interesting multi-terminal devices. Figure 4.5a shows an SEM micrograph of a suspended graphene flake with side contacts and pre-defined bottom gates, which is designed to explore the effect of electron guiding by a gate-defined potential [99]. We found that these devices can survive current annealing between the major contacts and graphene can be cleaned also around the side contacts. Figure 4.5b presents an SEM micrograph of a suspended graphene flake, where a hole has been realized prior to suspension by oxygen plasma etching to realize a suspended Aharonov-Bohm ring. This reveals that graphene can be pre-shaped before suspension without the apparent collapse of the flake. However, the yield of successful current annealing is substantially decreasing. Figure 4.5c shows another multi terminal device where we have defined six contacts (1-6) to graphene, four contacts at the edge, and "finger-shaped" injectors in the middle of the flake. The injectors (2,5) are separated from

graphene by an aluminum oxide layer and only touch graphene in a small region. The structure is complemented with a bottom gate, shown in yellow. These structures allow to conduct electron-optics experiments in ultra-clean, ballistic graphene. We discuss measurements of such multi-terminal-devices in Chapter 7 and 8.

4.6. Superconducting Contacts

For the devices we have shown so far, we used palladium as a contacting material. The combination of superconducting (S) contacts with graphene (G) [100] is more difficult, however highly desirable. From the viewpoint of electron optics, ballistic SG interfaces offer completely new possibilities. For instance, an SG interface can exhibit retro- or specular reflection [101], depending on how close to the Dirac point the device is being operated. Using the magnetic field as a lens, electron and hole states along the SG interface emerge [102, 103] that resemble the snake states discussed in Chapter 6. Furthermore, the superconductor can act as a source for entangled electrons. By using the tools of electron optics (waveguides, lenses, mirrors, collimators), the interference of those entangled electrons might be studied. The entangled Cooper pairs, however, have to be split beforehand. The most successful geometry uses Coulomb blockade to achieve this [104] which yielded a splitting efficiency of up to 90% in carbon nanotubes [105]. Cooper-pair splitting using Coulomb blockade has been also achieved in graphene recently [106, 107]. Other proposals try to use a *p-n* interface to split Cooper pairs [108], the requirements on residual doping and uniformity close to the contacts are, however, out of reach.

Recent results reported on the successful realization of ballistic SGS junctions using encapsulated graphene by showing that the critical current follows a Fabry-Pérot oscillation pattern [109–111]. In the scope of this thesis, several attempts were made to combine ballistic suspended graphene with complex gating structures and superconducting (S) contacts. Figure 4.6 summarizes these efforts.

We deposit $40-50\,\text{nm}$ aluminum (Al) with a $5\,\text{nm}$ thin contacting layer of palladium as S contact. We use Al mainly for fabrication reasons: Since it can be evaporated thermally, the LOR substrate is not exposed to an electron beam during the evaporation process, in contrast to sputter-deposition. Three distinct device architectures are explored. First, we fabricate Pd/Al contacts only, yielding junctions with two S contacts and local Au bottom gates, as shown in the schematics of Figure 4.6a1 and the SEM image of Figure 4.6a2. By in-situ current annealing at $4\,\text{K}$ through the S contacts, a rather narrow Dirac dip is obtained for several junctions. This is shown in Figure 4.6a3, where the conductivity σ as a function of gate voltage shows a dip around $0\,\text{V}$. For large gate voltages, σ saturates at around $2.7\,e^2/h$ only, which corresponds to a comparably high contact resistance of $R_c \approx 9\,\text{k}\Omega$. In Figure 4.6a4, the resistance as a function of source-drain current I_{SD} at $B = 10\,\text{mT}$ and $B = 70\,\text{mT}$, is given at a temperature of $60\,\text{mK}$. At $10\,\text{mT}$, two features that resemble a critical current seen at $\approx 0.9\,\text{mA}$ and $\approx 0.1\,\text{mA}$. This shows on one hand, that the supercon-
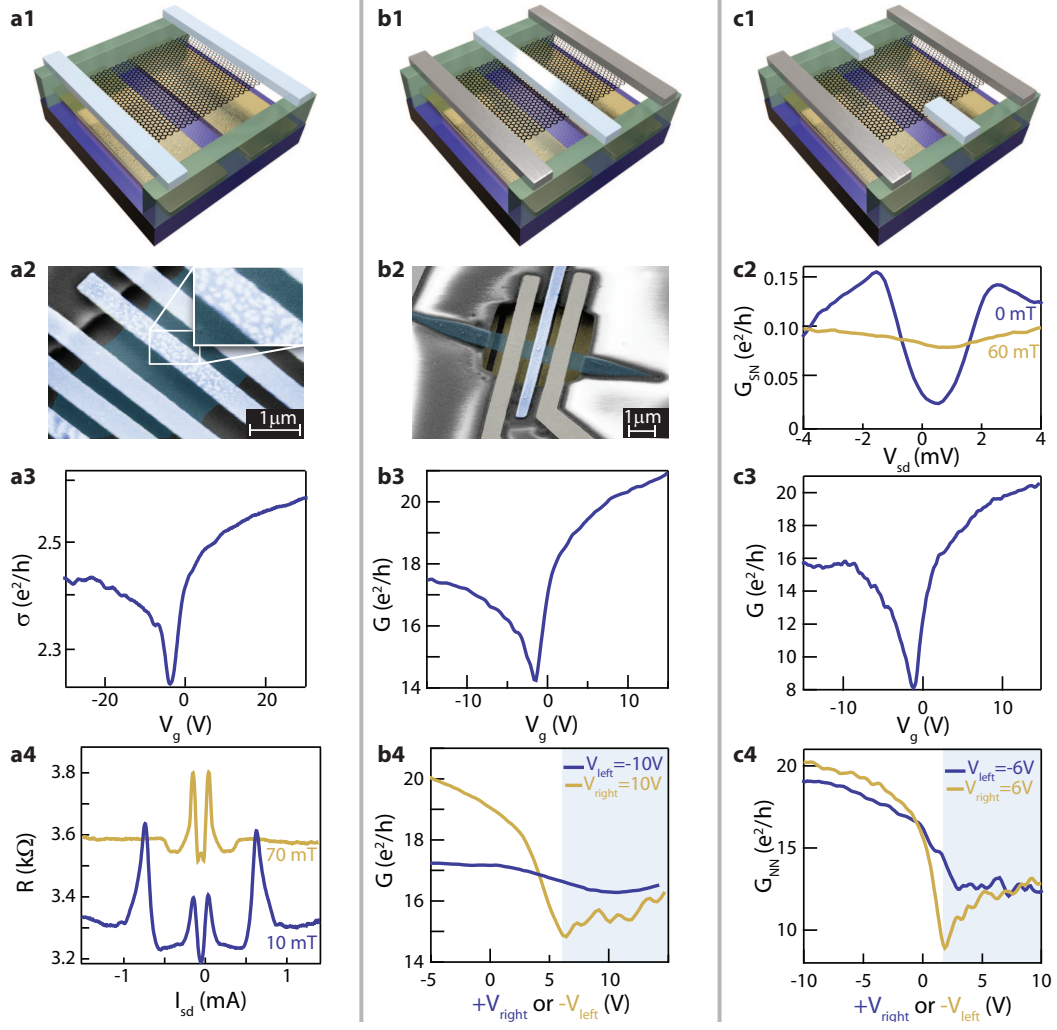
Figure 4.6.: Three distinct geometries combining S contacts with suspended, locally tunable graphene. **a1**, Three-dimensional design of a suspended graphene device tuned by local gates (gold) and contacted with Al (light blue). **a2**, SEM micrograph after current annealing. **a3**, σ as a function of both gates $V_{\mathrm{g}} = V_{\mathrm{left}} + V_{\mathrm{right}}$. **a4**, $R(I_{\mathrm{SD}})$ at small magnetic fields. **b1**, Design and **b2**, SEM image of a hybrid device with Pd (gray) and Al (light blue) contacts. **b3**, Field effect $G(V_{\mathrm{g}})$. **b4**, By tuning the left and right gate voltage independently, the device can be in the unipolar or bipolar (blue shaded) region. Tuning with V_{right} (blue curve) shows almost no change in G, whereas the formation of the *p-n* junction can be clearly seen on the yellow curve where V_{left} is tuned. **c1**, Design of the third architecture where the middle S electrode is split into two side contacts. **c2**, G as a function of source drain voltage V_{SD} measured between the S and the normal (N) Pd contact reveals a soft gap that disappears at $B = 60\,\mathrm{mT}$ ($T = 50\,\mathrm{mK}$). **c3**, $G(V_{\mathrm{g}})$. **c4**, By tuning the two bottom gates individually, the formation of a *p-n* junction is possible.

39

ductors are coupled to graphene. On the other hand, the Al contacts are partially molten during the process of current annealing, as given in the inset of Figure 4.6a1, which was recorded after the last transport measurement. Therefore, one of the two or even both gap-like features could originate from weakly coupled S-islands in the Al contact itself. For many devices, in fact, we lost the contact to the Al strip during the process of current annealing.

Apparently, it is problematic to perform current annealing through Al contacts, which have a bulk melting point of $\approx 660\,\mathrm{K}$ only. As an improvement, we therefore fabricate three-terminal devices with Pd and Pd/Al contacts, as sketched in Figure 4.6b1. The corresponding SEM micrograph is shown in Figure 4.6b2. Several attempts to clean such junctions by passing current from one Pd contact (gray) to the other while the Al contact (light blue) is floating, yielded a field effect behavior as the one shown in 4.6b3. Even though the minimum conductance is rather high, a relatively narrow Dirac dip is observed close to zero gate voltage. For this measurement, both gates, i. e. the one tuning the left cavity (between the left Pd and the Al contact) and the one tuning the right cavity, are coupled together. All of the devices with this geometry show very non-uniform cleanliness, i. e. one of the cavities is clean and the other remains disordered. This can be seen in Figure 4.6b4. If the gate voltage of the left cavity is fixed at $V_{\mathrm{left}} = -10\,\mathrm{V}$ and V_{right} is increased from $-5 \rightarrow 10\,\mathrm{V}$, G is changing only very little (blue curve). On the other hand, by tuning V_{left} and fixing V_{right} the conductance is decreasing in the *n-n*-region and oscillates in the *n-p* region (yellow curve). This observation leads to the conclusion, that in the left device, a Fabry-Pérot cavity can be formed (for more details see Chapter 5), whereas the right cavity remains disordered after current annealing. Further current-annealing steps, eventually also through the Al contact, did not improve the quality of the device.

Last, the middle S contact is split into two side contacts (Figure 4.6c1) to allow more uniform cleaning. Even though the S contact is rather resistive after current annealing, a soft gap is visible at $50\,\mathrm{mK}$ and $0\,\mathrm{T}$ and disappears at $60\,\mathrm{mT}$ as visible in the $G_{\mathrm{SN}}(V_{\mathrm{sd}})$ graph of Figure 4.6c2. G_{SN} is measured between one of the S and an N contact. The field effect measured between the two N contacts (Figure 4.6c3) shows a strong depletion of carriers around $0\,\mathrm{V}$, indicating very clean graphene. In this device, the formation of a Fabry-Pérot cavity is possible with both the left and the right bottom gate, as revealed in Figure 4.6c4, where a reduction of conductance and an oscillating pattern occurs in the *p-n* region (blue shaded). We conclude that it is possible to combine suspended, ballistic graphene with local gate structures and superconducting contacts. Unfortunately, further measurements in these devices were inconclusive. More work is needed to perform electron-optical experiments with superconducting contacts.
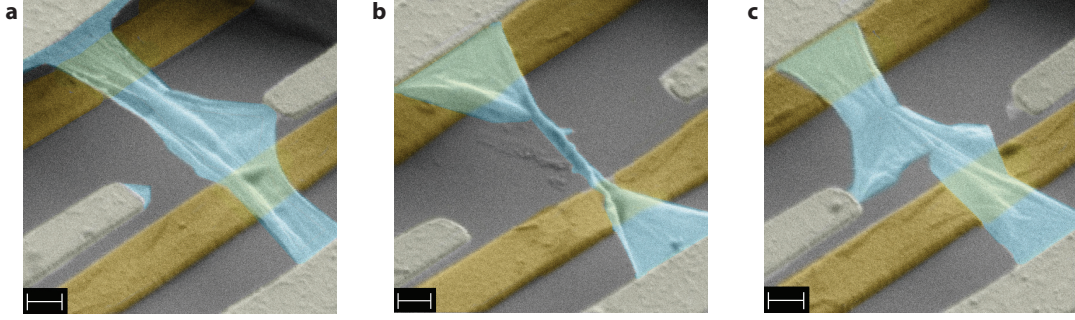
Figure 4.7.: Typical problems occurring to suspended graphene flakes: **a**, breaking, **b**, rolling up and **c**, cracking. Scale bar: 200 nm.

4.7. Device stability

A one-atom thick suspended layer is delicate to handle. Often, devices collapse after suspension or they break apart as the flake shown in Figure 4.7a. In many cases, graphene rolls up during the process of current annealing (Figure 4.7b), or cracks form (Figure 4.7c).Therefore, an important part of this work was to find conditions for mechanically stable devices and reproducible current annealing. Using CVD graphene turned out to be helpful for this purpose, since large areas can be pattern with test structures. The CVD graphene used here was grown and transferred by Kishan Thodkar from the University of Basel.

We exploited the stability of various designs , as shown in Figure 4.8. Graphene was shaped using an oxygen plasma in a reactive ion etcher (details are given in Appendix B.6). Two-terminal samples are presented in Figure 4.8a where the suspended graphene flake is colored blue. Due to the exposure to UV light during the etching process, deep trenches are seen in the LOR where the etching mask was defined. For the design of the structure, it has to be taken into account that the LOR in the parts exposed during the etching process will be developed. The stability of two-terminal quadratic samples depends on their length L and width W. We therefore created a pattern with various suspended junctions, having L and W ranging from $1 - 4\,\mu$m. The array shown in Figure 4.8b is repeated 12 times. Figure 4.8a gives a tilted view on one of the arrays in Figure 4.8b, where all the junctions remain suspended. We can therefore find the probability P for a junction of given L and W to collapse. Results are shown in Figure 4.8c, where it becomes apparent that P mainly depends on L. For $L = 4\,\mu$m, almost all junctions collapse, whereas the stability is high for $L < 3\,\mu$m. Wide junctions seem to be slightly more stable.

The stability of long junctions can be increased by attaching additional contacts. For instance, the distance between the two contacts crossing graphene in Figure 4.8d is $3\,\mu$m, but none of the designed structures collapsed (72 devices). This is true as long as the width w of the side contacts is large enough, i. e. $w > 500$ nm. Adding multiple terminals in different geometries, as it is e. g. done in Figure 4.8e-f, provides

additional stability, such that structures as long as $80\,\mu$m can be suspended (Figure 4.8g).
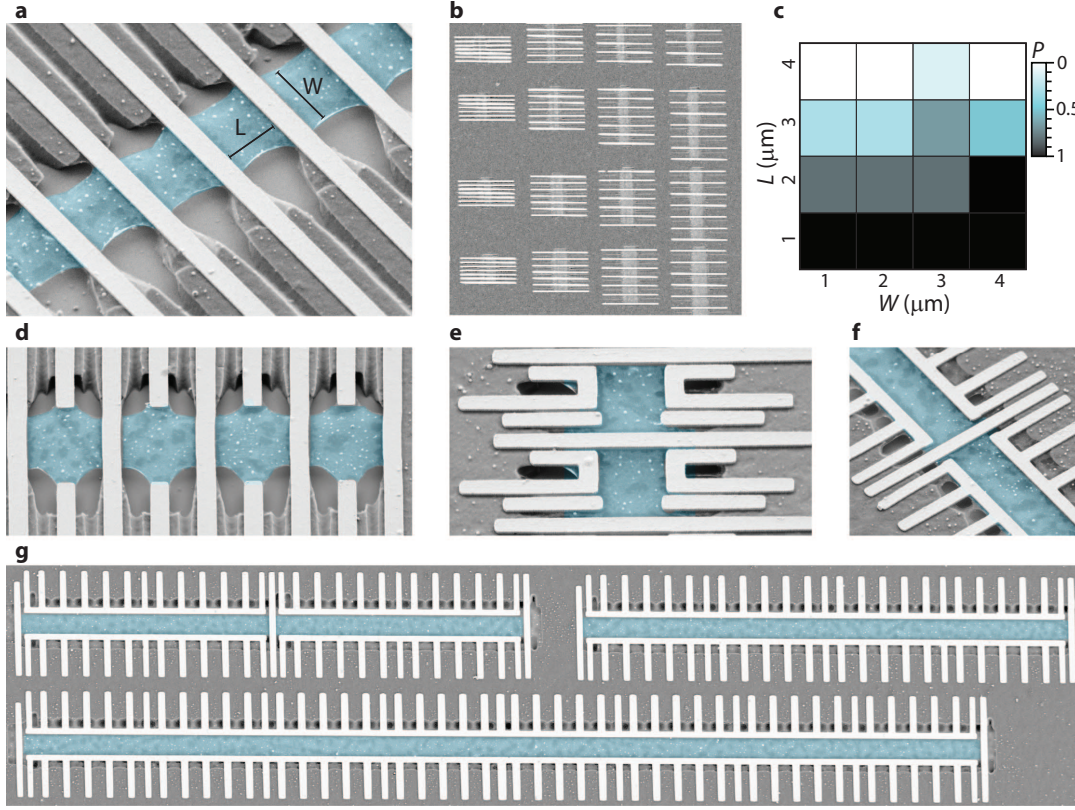
Figure 4.8.: Tests for mechanical stability after suspension of CVD graphene. **a-b**, An array of square devices with varying width W and length L and in **c**, the corresponding probability P that the graphene collapses after suspension. In **d-f** we show that devices get stabilized by adding contacts and can be suspended over up to $80\,\mu$m (**g**).

The mechanical stability after suspension is a requirement for successful current annealing, however additional complications start to become important. A systematic study of successful current annealing is extremely involving. We can therefore discuss only our experience with few distinct structures. For squared devices, the width becomes important. Whereas narrow junctions tend to roll up easily, very wide junctions ($> 4\,\mu$m) get extremely hot during annealing, such that we even observed melting of the Pd contacts in several cases (the melting temperature of Pd is $\approx 1550\,°$C). Ideal dimensions are $L = 2\,\mu$m and $W = 2 - 3\,\mu$m. For multi-terminal devices, the cooling-effect of the contacts needs to be considered. Residual dopants tend to accumulate close to these contacts. However, in the middle of the samples such devices can be cleaned with a very high yield. Additionally, we noticed that bi- and few-layer graphene is more stable during current annealing and yields higher

success rates. Furthermore, etched devices are less stable than devices where the original shape of the exfoliated graphene flake is preserved.

4.8. Conclusion

In conclusion, we have shown that the method based on LOR can be supplemented with local gating to realize complex structures. As the contacts are also suspended, cleaning of the graphene flake with current annealing can be performed with a high yield, and ultra-high mobilities can be obtained. Graphene can be supplemented with bottom and top-gates to form *p-n* junctions, which are the building blocks of more complex designs. Further abilities of the technique, such as side contacts and pre-shaping of the flake were shown. We discussed the implementation of superconducting contacts and finalized the chapter with information on mechanical stability.

5

Ballistic interferences in suspended graphene

In this chapter and Reference [67], we report on the characterization of ballistic suspended graphene *p-n* junctions. By local electrostatic gating, resonant cavities can be defined, leading to complex Fabry-Pérot (FP) interference patterns in the unipolar and the bipolar regime. The amplitude of the observed conductance oscillations accounts for quantum interference of electrons that propagate ballistically over long distances exceeding $1\,\mu\mathrm{m}$. We also demonstrate that the visibility of the interference pattern is enhanced by Klein collimation at the *p-n* interface [36, 37]. In addition to our publication [67], we demonstrate Fabry-Pérot oscillations in a *p-n-p* device that exhibit a visibility close to theoretically expected maximum and we discuss related studies that were published after our work.

5.1. Gate map of two Fabry-Pérot cavities

We focus on a graphene FP cavity that consists of two segments: left and right. We assume that in both segments the carrier density and its sign (*n* and *p*) can be controlled independently by two gate voltages V_{left} and V_{right} with identical efficiency. Figure 5.1 shows in a schematic 2D conductance map the expected FP interference pattern as a function of V_{left} and V_{right}. This map has four quadrants corresponding to the four polarity configurations [92, 93, 112, 113]. If the left and right segments have the same polarity (*n-n* or *p-p*), the cavity is in the unipolar regime. In contrast, in the case of opposite polarities (*n-p* or *p-n*), the cavity is in the bipolar regime. In the unipolar regime only interferences of electrons bouncing back and forth between the two outer contacts are expected (lower left and upper right panel in Figure 5.1).The corresponding beating pattern evolves along $V_{\mathrm{left}} = V_{\mathrm{right}}$ and is indicated by the purple lines in the central panel of Figure 5.1. In the bipolar case, assuming a semi-transparent *p-n* interface between the segments, the junction can be considered as two cavities in series, each controlled by its respective gate. Resonances in the left (right) cavity depend only on V_{left} (V_{right}) and are represented by green (blue) lines. Another distinct set of resonances in the bipolar regime can arise from charge carriers
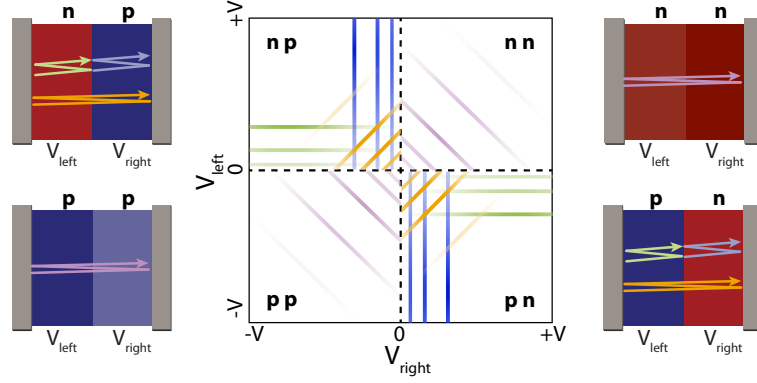
Figure 5.1.: Schematic representation of all possible resonance conditions (central panel) in a FP resonator that consists of two segments of equal size (left and right panels). The carrier density and carrier type (*n* or *p*) in both segments can be tuned independently by V_{left} and V_{right}. FP resonances may occur due to reflection at the outer contacts or at an internal *n-p* (*p-n*) interface between the two segments. The possible resonant conditions are indicated by color-coded lines for the respective cases in the middle part.

that tunnel through the central *p-n* interface in the middle and bounce back and forth between the outer contacts. The corresponding pattern should evolve along the condition $k_{\text{left}} \approx k_{\text{right}}$. In terms of gate voltages this condition corresponds to $V_{\text{left}} \approx -V_{\text{right}}$ as indicated in Figure 5.1 by the orange lines.

5.2. Device architecture

To realize experimentally such a tunable FP cavity, devices were prepared by combining a mechanical transfer process [54] with a hydrofluoric acid-free suspension method proposed by Tombros *et al.* [65]. A complete description of the fabrication process is given in Chapter 4. Figure 5.2b shows a colored optical image of several junctions realized within the same graphene flake indicated by white dashed lines. An SEM micrograph of three *p-n* junctions is presented in Figure 5.2c. A voltage applied on the bottom gate (V_{right}, yellow electrodes in Figure 5.2b-c) will tune the charge carrier density on the right side of a junction, while a voltage applied on the back gate (V_{left}) will act on the left side. The device was measured in a ^{4}He cryostat at a temperature of $T = 1.5$ K. Differential conductance, $G = dI/dV$ was measured by standard lock-in techniques with a voltage bias of 100 μV at 77 Hz. Series and contact resistances were not subtracted from the data.
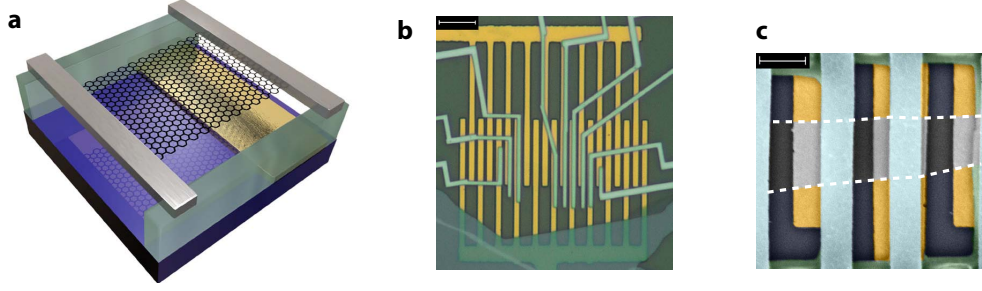
Figure 5.2.: **a**, Three dimensional illustration of the device architecture. The bottom-gate is in gold and ohmic contacts in gray. The LOR resist appears in light green. **b**, Optical picture of several *p-n* junctions. Scale bar, 5 μm **c**, Scanning-electron microscopy image of three graphene *p-n* junctions next to each other. Bottom gates are shown in yellow and contacts in gray. Scale bar: 1.2 μm.

5.3. Electronic transport characteristics

Figure 5.3 shows the main experimental result of this chapter. In part **a**, the differential conductance between the two contacts as a function of V_{right} and V_{left} is presented for a junction of length $L = 1.2$ μm and width $W = 3.2$ μm. As expected, this 2D plot reveals four regions indicated by the labels *p-p*, *n-n*, *n-p* and *p-n* corresponding to different carrier types in the two sides of the sample. The borders between the unipolar and bipolar regions coincide with the charge neutrality point of the left and right graphene segments (indicated by blue and green arrows respectively). The border lines between the different regions are not perpendicular to each other for two reasons. First, both the back gate and the bottom gate are at a distance to the graphene sheet that is comparable to the length of the device. This leads to a cross coupling between the two gates i.e., the right gate also affects the left graphene segment and *vice versa*. Second, the back gate (left gate) is below the bottom gates and therefore strongly screened, leading to a much weaker gate coupling from the back gate to the graphene than from the bottom gate.

A slice through the 2D conductance plot along the white dashed line is shown in Figure 5.3b as a function of carrier density n which we estimated from a parallel plate capacitor model. A positive sign refers to the *n*-region and a negative sign likewise to the *p*-region. A change in gate-voltage of 1V along the white dashed line induces a change in density of $n \approx 9 \cdot 10^9$ cm^{-2}. The graph exhibits a remarkably sharp conductance dip, corresponding to the charge neutrality in the entire graphene sheet. The fact that this dip also occurs close to zero gate-voltage reflects the high quality of the graphene sample. The conductance saturation and the asymmetry at high carrier density suggest an *n*-type doping of the graphene below the palladium contacts [114,115]. With Equation 3.4 we estimated a mobility of $\mu \approx 150 \cdot 10^3$ cm^2/Vs at $n = 4 \cdot 10^9$ cm^{-2}. The junction reaches a minimal conductivity of $\sigma_{\text{min}} \approx 2e^2/h$

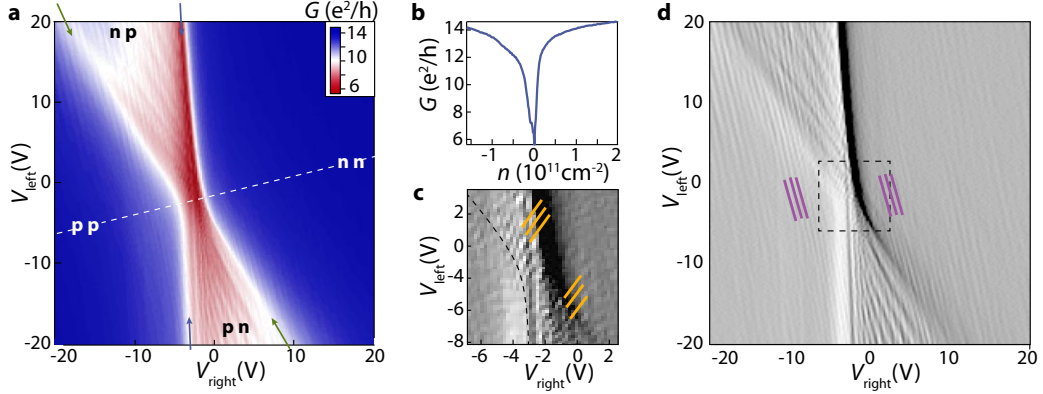Figure 5.3.: **a**, Two terminal differential conductance $G = dI/dV$ as a function of V_{right} and V_{left} at $T = 1.5$ K, demonstrating independent control of carrier type and density in the left and the right side of the graphene sheet. Labels in each of the four conduction regimes indicate the carrier type. **b**, Conductance as a function of charge carrier density n along the dashed white line of (a). **c**, Zoom into the transconductance map presented, in (d), around the charge neutrality point. **d**, Transconductance obtained from the numerical derivative with respect to V_{right} of (a) emphasizing conductance oscillations. Color-coded lines link the observed conductance oscillations with the FP interference pattern expected from the simple picture of Figure 5.1: light blue lines in the unipolar regime, green and blue lines for interferences on either side of the graphene in the bipolar case and orange lines for full length interference in the bipolar regime.

close to the ballistic limit of $4e^2/\pi h$ [79] indicating a weakly disordered graphene sheet [64,84].

5.4. Signatures of quantum interferences

The most striking features in the conductance map are, however, the oscillation patterns visible in both the unipolar and bipolar configuration. To emphasize these features, the transconductance dG/dV_{right}, numerically calculated from the data in Figure 5.3a, is presented in Figure 5.3d. The different interference patterns expected from the simple picture of Figure 5.1 are well revealed in this map. In the unipolar case, one global interference pattern is visible (highlighted in a small region by light-blue lines) corresponding to FP interferences of electron waves that bounce back and forth between the outer metallic contacts. In the data the density separation equals $\Delta n \approx 10^{10}$ cm^{-2} between constructive interference peaks at around $n = 10^{11}$ cm^{-2}. Based on the equation $n = \text{sgn}(E)k^2/\pi$ and the resonance condition $\Delta k L_{cavity} = \pi$

we derive the relation $\Delta n = 2\sqrt{\pi n}/L_{\text{cavity}}$. This yields an effective cavity length $L_{\text{cavity}} \approx 1.1~\mu\text{m}$ in good agreement with the geometrical length $L = 1.2~\mu\text{m}$ of the junction. In the bipolar regime at high doping two clear oscillation patterns are visible. One pattern is mainly tuned by V_{right}, indicating that resonances arise from the cavity created at the right side of the *p-n* interface. This pattern is highlighted by blue lines in Figure 5.3d. The other pattern marked by green lines is predominantly tuned by V_{left}, indicating that it originates from the cavity formed at the left side of the *p-n* interface. The area in the transconductance map marked by the dotted square is enlarged in Figure 5.3c. It shows yet another oscillation pattern (orange lines) which follows gates values such that $n_{\text{left}} \approx -n_{\text{right}}$. With an interference period $\Delta n \approx 3 \cdot 10^9~\text{cm}^{-2}$ at $n = 10^{10}~\text{cm}^{-2}$ the cavity length is $L_{\text{cavity}} \approx 1.2~\mu\text{m}$. We conclude that these oscillations must arise from quantum interference over the full device length, i.e. charge carriers that tunnel through the *p-n* interface, changing their character from n to p and back.

We emphasize at this point that there is no evidence of disorder in the transconductance plot of Figure 5.3d. All patterns are regular and can be ascribed to distinct FP cavities, some of which extend in length over the whole device. The occurrence of FP interference patterns implies that the phase-coherence length exceeds twice the system size. Random disorder would generate further interference patterns, but these are never regular. The fact, that we can deduce from the interference pattern effective cavity-lengths from contact to contact, and that we do not see any irregular features, are strong signs for ballistic coherent transport over distances exceeding $2~\mu\text{m}$.

5.5. Simulation and comparison with experiment

To confirm the ballistic origin of the observed interference patterns, the charge transport through the graphene device is simulated in the phase-coherent ballistic regime using the actual geometrical parameters of the device. The computed conductance is shown in Figure 5.4d, which presents a purely ballistic tight-binding transport simulation using a real-space Green's function method within the Landauer-Büttiker formulation [116] combined with the quantum capacitance model for carrier density computation [42]. Since no dephasing or energy averaging has been incorporated, the obtained conductance modulations show the maximal possible visibility for this device geometry. In contrast to the method presented in Chapter 2.3 the two-dimensional graphene flake was reconstructed using the Bloch theorem on a nanoribbon. The correspondence between theory and experiment is remarkably good and supports the picture of ballistic motion drawn from experiment.

As pointed out before, we do see all the expected FP resonance patterns due to the formation of distinct cavities having different doping and different types of mirrors. However, the strength of the oscillation pattern (the visibility, as defined in Equation
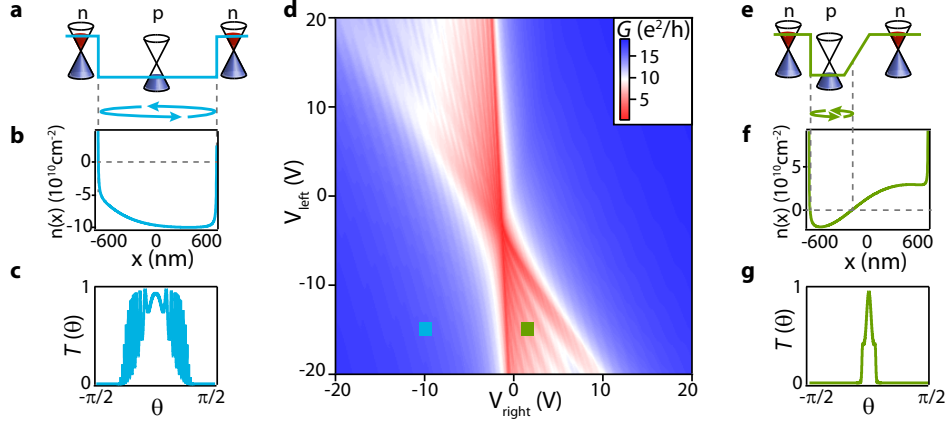
Figure 5.4.: **a**, Schematic view of charge carrier configuration at the unipolar point $(V_{\text{left}}, V_{\text{right}}) = (-15, -10)$V indicated by a blue square in (d). **b**, Calculated charge carrier profile at this point, and **c**, associated simulated transmission function *versus* incident angle θ. **d**, 2D conductance map obtained by tight-binding simulation as a function of V_{left} and V_{right}. **e-g**, Same as a,b,c but for parameters at the bipolar point $(V_{\text{left}}, V_{\text{right}}) = (-15, 2)$V indicated by a green square in **d**.

2.28) varies in different regions. This is linked to the reflection properties of our mirrors, determining the cavity finesse. Cavities can be created either by sharp or smooth unipolar or bipolar potential steps which have been compared in Chapter 2.2.3.

Suppression of backscattering due to pseudospin conservation implies that effectively all unipolar potential steps are highly transmissive for almost every incident angle [117] (only electrons with incident angles close to $\pi/2$ have an appreciable backscattering probability). Cavities created by unipolar interfaces have consequently a small finesse and will display small visibilities.

We turn now to the reflection properties of a *p-n* junction. We assume that the carrier densities on both sides are of opposite sign but equal in magnitude and that k_F denotes the wavevector in the homogeneous region outside the junction. In the case of a sharp *p-n* interface with $k_F d \ll 1$ the transmission probability is given by $T(\theta) = \cos^2(\theta)$ [38] as shown in Chapter 2.2.2. The corresponding cavities have a small finesse for electron waves over a large range of incident angles around $\theta = 0$ and will therefore have a small visibility (see Chapter 2.2.6). The situation is different for a smooth *p-n* junction. Since the charge carrier density evolves smoothly through zero, essentially all electron trajectories are adiabatically refracted off the interface (total reflection) except for the normal one, which can Klein-tunnel through the junction [36, 38]. The transmission probability through such a smooth *p-n* junction is given by the expression $T(\theta) = \exp(-\pi k_F d \sin^2 \theta)$ (Equation 2.23) which also predicts perfect transmission at normal incidence. Similar to the sharp interface one could expect the

visibility of the interference pattern to be small. However, Klein tunneling does not only yield full transmission at normal incidence but also leads to a strong collimation in transmission. Therefore, almost all trajectories that are incident under a small angle ($\theta \neq 0$) are exponentially suppressed and do not add to the total conductance. This suppression of the background current increases the overall visibility. Although the finesse vanishes for $\theta = 0$ the contribution from small angles (with $\theta \neq 0$) yield a higher visibility than for unipolar or sharp bipolar cavities.

5.6. Visibility of the interference

Based on the preceding discussion, we now compare the observed visibilities for two particular cases in a) the unipolar and b) bipolar regime at gate voltages $(V_{\text{left}}, V_{\text{right}}) = (-15, -10)$V and $(-15, 2)$V, respectively. These two points are marked in Figure 5.4d by light-blue and green squares. For both cases, the reflection properties at the contacts are important parameters and need to be known. The full comparison of the simulation with the experiment reveals that the contacts dope graphene as n-type. In addition to this doping the simulation includes a small mass term in the contacted region [118]. For the unipolar case, the simulation yields the charge carrier density profile plotted in Figure 5.4b. In this configuration the interior of the FP cavity is p-type with mirrors created by the p-n interfaces close to the Pd contacts. The latter can be considered to be relatively sharp due to the rapid decay of the contact-induced screening potential [44]. Consequently, these interfaces are almost transparent and give rise to low finesse for the FP interferences as found in the experimental and the numerical conductance map with respective average visibilities of 0.5% and 2%.

In the bipolar case the simulation yields the carrier density profile plotted in Figure 5.4f. It presents an extremely smooth p-n interface created electrostatically in the middle of the graphene sheet. The two cavities created on the right and left side will present a much higher finesse than in the unipolar configuration which consistently leads to higher visibilities in both the experimental and numerical conductance maps. The average visibility for the experiment is around 5%, whereas the simulation yields 20%. The calculated angle dependent transmission probabilities for both regimes are plotted in Figures 5.4c and g respectively, which clearly demonstrate that the visibility difference between the unipolar and bipolar regime is a direct consequence of the exponential collimation of Klein tunneling [36, 38, 117].

5.7. Increased finesse in a *p*-*n*-p cavity

The finesse of the cavity is further increased in a structure that exhibits two smooth p-n interfaces. This is realized in a p-n-p geometry, where the electrons in the middle cavity will oscillate between two smooth interfaces. We fabricated such a device using two sets of bottomgates that can be tuned independently. In Figure 5.5a its
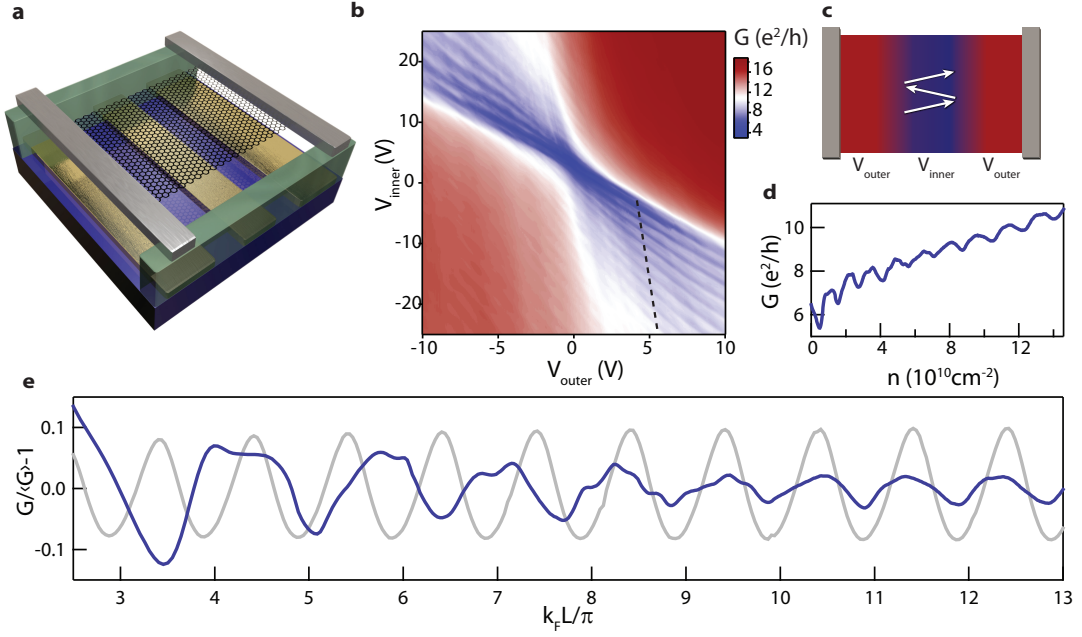
Figure 5.5.: **a**, 3-dimensional design of a device featuring a *p-n*-p junction. The middle gate and the two outer gates can be tuned independently. **b**, Fabry-Pérot color-scale map where the conductance as a function of inner (V_{inner}) and outer (V_{outer}) gate voltage is shown. The strongest oscillations are parallel to the inner gate. They are sketched in **c**. **d**, A slice taken in **b** showing the strong oscillations in the middle part. These are replotted in **e** as a function of $k_F L/\pi$ yielding a visibility close to the analytically expected 20% and a periodicity of $k_F L/\pi$ for larger values of k_F. The first oscillations do not follow the periodicity since the cavity size L is changing drastically there.

architecture is shown in a three-dimensional image. The bottomgates are 600 nm wide and 600 nm spaced. The graphene flake is suspended over $3\,\mu$m.

With current-annealing we could achieve an extraordinary clean material, as can be seen in Figure 5.5b. The interferences that occur in the unipolar regime are due to electron trajectories bouncing between the contacts, showing $3\,\mu$m ballistic transport. In the conductance map the lines parallel to the Dirac-point of the inner region are much more pronounced than the lines parallel to the outer Dirac-point. This already reveals that the Fabry-Pérot etalon formed in the inner cavity (Figure 5.5) has a higher finesse than the outer cavity. Indeed the visibility we could measure in this device exceeds the numbers measured in the *p-n* geometry by far. In Figure 5.5d we show a slice along the black dashed line in the conductance map. This data is divided by its background conductance $\langle G \rangle$ and plotted as a function of $k_F L/\pi$ in Figure 5.5e. The experimental data is compared to values obtained from the analytical Equation 2.26.

Despite the simplicity of the model, the experimental data matches the theory well (as it has been stressed also in Chapter 3.2.2). We therefore demonstrate that scattering and transmission at our smooth *p-n* junctions is close to ideal. The discrepancy at small $k_F L/\pi$ originate from the fact, that the cavity size is strongly changing at small gate voltages, which is not taken into account in the analytical formula. It has to be noted that the visibility of the interference is with 20%, best to our knowledge, the highest reported so far for graphene *p-n* cavities. Due to Klein tunneling, a large background current (80% of the conductance) persists, but this current is strongly collimated. Since reflection and transmission at the interface are close to ideal we can a conclude also, that our smooth *p-n* junction acts as very efficient angular filter (compare to e. g. Figure 2.9).

5.8. Related studies

Since the release of the herein discussed findings [67], related results have been published. At the same time and in a similar geometry, Grushina et. al. [66] demonstrated tunable Fabry-Pérot oscillations in *p-n* junctions. As an additional information, temperature dependence of the Fabry-Pérot oscillations revealed, that the oscillation pattern washes at $T = 40\,\mathrm{K}$ or $3.5\,\mathrm{meV}$. This energy scale is in agreement with the particle in a box picture. The visibility and collimation were, however, not in the focus of Reference [66].

Later, longitudinal and transverse interference patterns have been revealed by Fourier analysis technique and shot noise detection in Reference [119]. The measurements were performed on a suspended graphene device with large aspect ratio $W/L \approx 4$, and the *p-n* junction was created by the contact doping solely.

Fabry Pérot oscillations have been observed in encapsulated bilayer graphene by Varlet et. al. [120]. It was revealed that in gapped bilayer graphene, the Berry phase can be tuned, and can, in principle, take any value between 0 and 2π. One could expect that high finesse cavities can be created with bilayer graphene due to the suppression of the zero incidence angle (anti-Klein tunneling). The demonstrated oscillations however occured at larger displacement fields where a gap in bilayer graphene is opened and the transmission for zero incidence is no longer zero. The observed visibility in this case is of the order of 1%. It has to be taken into account however, that the topgate in this device was much closer to the graphene, leading to a much sharper *p-n* interface. In our experiments on bilayer graphene, even in very clean devices, we were never able to observe any Fabry-Pérot oscillations for the low densities and displacement fields achievable in our devices.

By studying a trilayer graphene (TLG) Fabry-Pérot interfereometer, a large visibility (20%) was demonstrated in a certain regime [121]. The Bernal-stacked TLG exhibits single- and bilayer 'flavor' which can be addressed by out-of plane electric fields. The conductance oscillations were achieved in an interflavor regime where the leads exhibit monolayer-like holes and the cavitiy bilayer-like electrons.

A standing wave pattern in a circular *p-n* junction has been demonstrated recently [122] and named after the acoustic phenomena of whispering gallery modes. The *p-n* potential in this case was created by an STM tip. Furthermore, ballistic interference patterns where studied in high-quality encapsulated graphene, contacted with superconducting electrodes of MoRe [109], Nb [110] or Al [111] demonstrating oscillating supercurrents with large mean free paths.

5.9. Conclusion

In conclusion, we have fabricated and characterized clean suspended graphene that allowed the formation of *p-n* junctions. Fabry-Pérot type conductance oscillation patterns visible in both unipolar and bipolar regimes point to an extremely long mean free path and phase-coherence length > 2 μm accessible in these devices. Moreover we have shown that the visibility difference between the unipolar and the bipolar regime is due to Klein collimation occurring at a smooth *p-n* interface in graphene. The visibility could be enhanced from 1% between two sharp interfaces to 5% by adding one smooth interface and to above 20% for two smooth interfaces. This last value is close to ideal, demonstrating thereby that reflection and transmission at such a *p-n* interface are well controlled and that the interface can be used as a collimator.

6

Snake Trajectories in Ultraclean Graphene *p-n* Junctions

Snake states are trajectories of charge carriers curving back and forth along an interface. There are two types of snake states, formed by either inverting the magnetic field direction or the charge carrier type at an interface. Whereas the former has been demonstrated in GaAs-AlGaAs heterostructures, the latter has become conceivable only with the advance of ballistic graphene where a gapless *p-n* interface governed by Klein tunneling can be formed. Such snake states were hidden in previous experiments due to limited sample quality. Our extremely clean devices however allow the observation of these states. In this Chapter and Reference [123] we discuss magneto-conductance oscillations due to snake states in a ballistic suspended graphene *p-n*-junction which occur already at a very small magnetic field of 20 mT. We will show that the visibility of 30% is enabled by Klein collimation. Our finding is firmly supported by quantum transport simulations. We demonstrate the high tunability of the device and operate it in different magnetic field regimes. In Section 6.6 we go beyond Reference [123] and analyze a resonance pattern that is formed by stable trajectories bouncing off the boundaries of a *p-n* cavity in weak magnetic field. Such cavity resonances obey the Bohr-Sommerfeld quantization rule and resemble scar-states.

6.1. Evolution of electron trajectories in magnetic field

A magnetic field fundamentally modifies the transport properties of an electronic conductor by acting on its charge carriers via the Lorenz force. The most prominent magnetotransport effect is the quantum Hall effect in a two-dimensional electron gas (2DEG). A strong perpendicular magnetic field forces the charge carriers into one-

dimensional conduction channels that flow along the edges of a sample. At moderate magnetic fields however electron trajectories can be understood in a quasiclassical picture where the Lorenz force bends charge carriers into cyclotron orbits. At the boundary of a conductor charge carriers are not localized and can propagate via so-called skipping orbits. Magnetic focusing experiments [10, 46] represent a direct proof of the skipping orbit picture. In such experiments an increase of conductance is observed if the distance between two contacts is an integer multiple of the diameter of a cyclotron orbit. One condition for the observation of such trajectories is ballistic transport over the relevant device dimensions. This has limited the observation of skipping orbits to the cleanest available semiconductor samples.
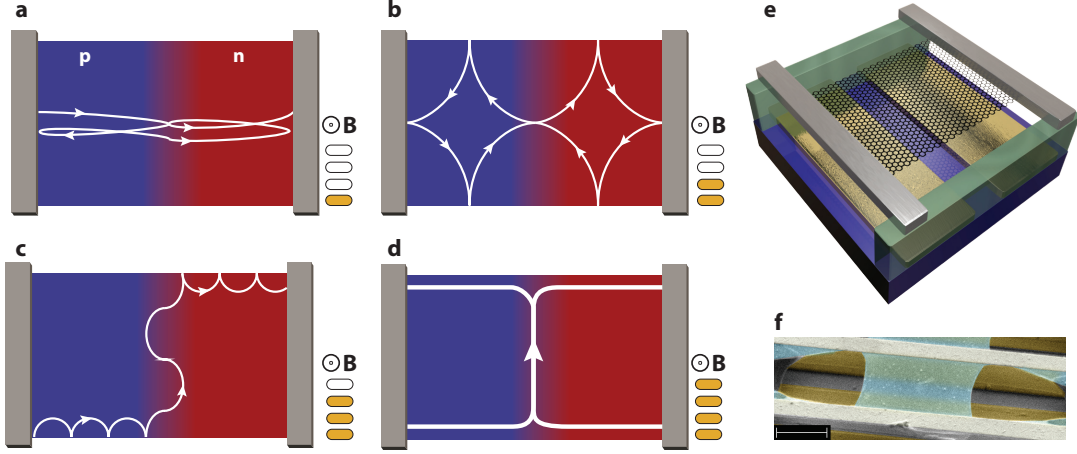

Figure 6.1.: **Evolution of electron states in increasing magnetic field and design of a graphene *p-n* junction. a**, A two-terminal graphene device consisting of a hole (blue) and an electron (red) cavity is sketched. By applying a weak field, the electron trajectories in the p- and n-cavities bend, leading to dispersing Fabry-Pérot resonances. **b**, The field is increased until the cyclotron orbit becomes comparable to the cavity size, where resonant scar states can occur. **c**, The field is further increased and transport is still described by quasiclassical cyclotron orbits. Snake states along the *p-n* interface form. **d**, Finally, quantum Hall edge states propagate in opposite direction in the p- and n-region at higher fields. **e**, 3D design of the measured device. The SiO$_2$ substrate is colored in blue and the bottom-gates in gold. The contacts, supported by the lift-off resist LOR (green) are colored in gray. **f**, Scanning electron microscope image of a device similar to the measured sample. The graphene is colored in blue and the bottom-gates in gold. The scale bar corresponds to 1 μm.

The possiblity to form gap-less *p-n* interfaces (Chapter 2.2) in ballistic graphene (Chapters 3 and 5) gives rise to new quasi-classical trajectories in magnetic field: The

snake states. If electrons that propagate via skipping orbits encounter a *p-n* interface, they turn into snake states. These states consist of alternating half circles with opposite chirality and they transport current along the interface. Similar snake states have first been realized in GaAs/AlGaAs 2DEGs by defining regions of alternating magnetic field direction [124]. These states share the condition of commensurability (similar to the above described magnetic focusing experiments) with *p-n* snake states but they do not propagate along a single and tunable interface. Snake states in graphene *p-n* junctions were claimed to have been observed in disordered substrate supported samples [125] but the experiment lacked of direct evidence for snaking trajectories.

In Figure 6.1a-d we illustrate schematically how trajectories under increasing perpendicular magnetic field evolve in such a device. Figure 6.1a describes the low-field situation where transport is still dominated by Fabry-Pérot oscillations with slightly bent trajectories [37]. As the field is increased, resonant scar states (Figure 6.1b) may occur, as observed in semiconductor quantum dots [126]. At higher fields (Figure 6.1c), snake states at the *p-n* interface govern the electronic properties. Finally (Figure 6.1d), the system enters the quantum Hall regime [11, 127] where transport is dominated by edge states and Landau level mixing at the *p-n* interface can occur [93, 128]. Even though this Chapter is focusing on snake states, we will discuss the phenomenology of the mentioned magnetic field regimes. By doing so we present an integral picture of graphene *p-n* physics in magnetic field.

6.2. Device Characterization

Figure 6.1e shows the design of the measured device and Figure 6.1f a scanning electron microscope picture of a similar sample. In a suspended $2 \times 2\,\mu$m graphene sheet a *p-n* junction is formed by applying different voltages on the left (V_{left}) and right (V_{right}) bottom-gates, resulting in different charge carrier concentrations n_{left} and n_{right}. The device and its fabrication is similar to the previously discussed sample.

In the following we characterize the measured device in the zero, low- and high-field regimes. Figure 6.2a shows a two-dimensional color map of the electrical conductance $G(V_{\text{right}}, V_{\text{left}})$. As soon as a *p-n* interface is formed, G is lowered drastically. Regular Fabry-Pérot resonances in the left/right cavity are visible as oscillations perpendicular to the zero density line in the left/right cavity (horizontal/vertical white dashed line in Figure 6.2a, indicating ballistic transport [66, 67]. We extract the cavity length L used in Figure 6.2d-e from the spacing Δn between resonant Fabry-Pérot peaks in the bipolar situation $\Delta n = 2\sqrt{\pi n}/L$ and obtain $L \approx 0.8\,\mu$m which is consistent with the designed cavity. The inset in Figure 6.2a is a slice along the *pp-nn* diagonal (blue dashed). In Chapter 3, we estimated the mobility to be $\mu = \frac{1}{e}\frac{d\sigma}{dn} \approx 470 \cdot 10^3$ cm^{2}V^{-1}s^{-1} and the residual doping $\delta_n = 5 \cdot 10^8$ cm^{-2}.

In Figure 5.1b we show cuts along the *pp-nn* diagonal at different magnetic fields B and obtain quantum Hall plateaus at $G = G_0 \cdot \nu$, where $\nu = 2, 6, 10, \ldots$ is the
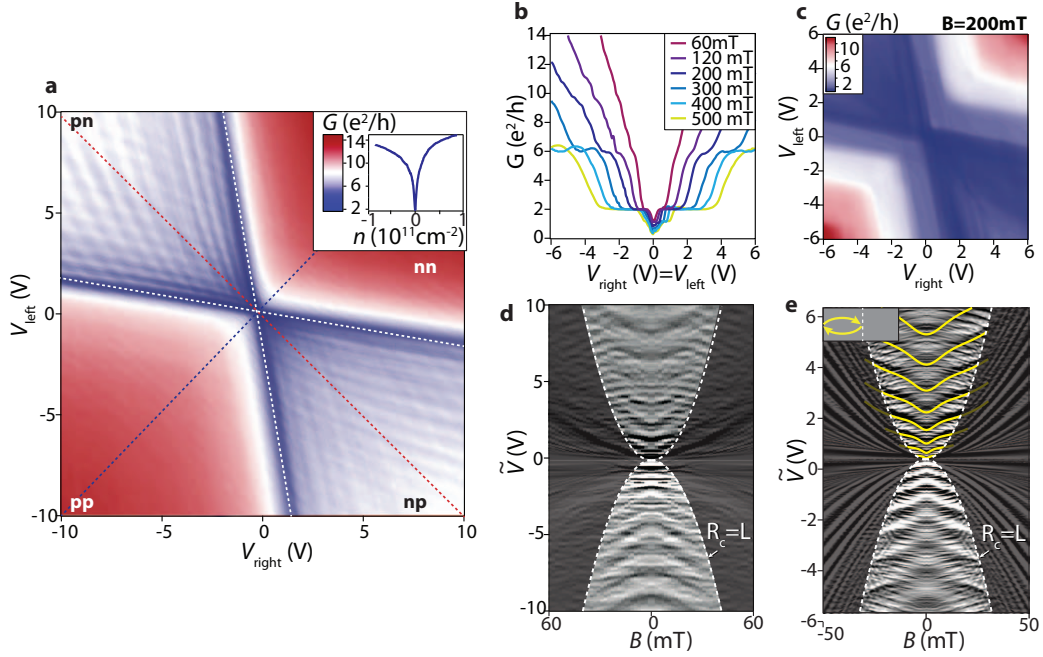
Figure 6.2.: **Device characterization in the Fabry-Pérot and in the quantum Hall regime.** **a**, Two-terminal conductance as a function of left and right gate voltage shows regular Fabry-Pérot oscillations at zero magnetic field. The inset reveals the narrow Dirac dip along the pp-nn diagonal (blue dashed line) from which a mobility of $\mu \approx 470 \cdot 10^3$ cm^{2}V^{-1}s^{-1} is deduced. **b**, Cuts along the same diagonal at different magnetic field strengths exhibit the expected quantum Hall plateaus at $2, 6, 10\, \text{e}^2/\text{h}$. The $G = 2\, \text{e}^2/\text{h}$ plateau is already visible at 60 mT. **c**, The color plot as a function of V_{left} and V_{right} at 200 mT shows quantum Hall plateaus in the unipolar region. **d**, The numerical derivative $dG/d\tilde{V}$ (in arbitrary unit) is recorded as a function of gate voltage $\tilde{V}$ and B displaying the dispersion of the Fabry-Pérot oscillations. $\tilde{V}$ is the magnitude of gate voltage in the situation of antisymmetric charge densities $n_{\text{left}} = -n_{\text{right}}$ (red dashed line in **a**. i. e. the *np-pn* diagonal). The white dashed curve indicates the line along which the cyclotron radius R_c is equal to the cavity length $L = 0.8\, \mu$m, the region $R_c < L$ is darkened and will be discussed in the main text. **e**, The measured pattern is reproduced by a tight-binding quantum transport calculation based on the designed geometry of the measured device. The small inset shows a resonant electron trajectory at low magnetic field. Constructive interference occurs if the phase along this trajectory is an integer of 2π, leading to the numerical solution of the yellow lines.

filling factor [11, 127] and $G_0 = e^2/h$ is the conductance quantum. We subtracted a contact resistance of 1.2 kΩ. Even at fields as low as 60 mT, the $\nu = 2$ plateau is visible. The colorscale map in Figure 6.2c taken at 200 mT shows that plateaus develop in the unipolar region with conductance values given by the lowest number of edge modes in the left or right cavity, i. e.. $G = G_0 \cdot \min(\nu_{\text{right}}, \nu_{\text{left}}) = 2, 6, 10\, e^2/h$. This observation compares well to experiments of Reference [93], even though we apply only 0.2 T instead of 4 T. In the bipolar region the conductance stays well below $2\, e^2/h$. In the case of Reference [93], higher Landau levels mix, leading to fractional conductance values in the bipolar situation. Due to the smoothness of the *p-n* interface in our case, edge states with higher filling factors do not come close enough to the *p-n* interface to mix, therefore we observe $G < 2\, e^2/h$.

In a further step we study the dispersion of the Fabry-Pérot interference pattern in low magnetic field [37]. Figure 6.2d shows the numerical derivative $dG/d\tilde{V}$ as a function of B and $\tilde{V}$, where $\tilde{V}$ represents the magnitude of gate voltage in the situation of antisymmetric charge density (red dashed line in Figure 5.1a, i. e. the *n-p-p-n* diagonal). In this configuration the device consists of two Fabry-Pérot cavities of equal length $L \approx 0.8\ \mu$m. The darkened region where the cyclotron radius $R_c < L$ will be discussed later. In Figure 5.1e a tight-binding transport calculation is shown which reproduces the measured interference pattern very well (for details see Reference [45]). We highlight the quality of the measured graphene and the ability of the simulation to capture the complex oscillation pattern of this micron-sized system in magnetic field.

The dispersion of the Fabry-Pérot oscillations can be described by bent electron trajectories such as the one sketched in the inset of Figure 6.2e [37, 67]. The yellow lines are numerically obtained from solving the resonance condition $\Delta\Phi = 2j\pi$, arising from the path difference between the directly transmitted and twice reflected trajectories within the p cavity as sketched in the inset of Figure 6.2e, which is found to be the major interference contribution. For such a simplified model the phase difference is given by $\Delta\Phi = \Phi_{\text{WKB}} + \Phi_{\text{AB}} + \Phi_{\text{Berry}} + \Phi_0$, where $\Phi_{\text{WKB}} = \sqrt{k_F^2 - (eBL/2\hbar)^2} \cdot 2L$ is the kinetic WKB-phase,[1] $\Phi_{\text{AB}} = \delta A \cdot eB/\hbar$ is the Aharanov-Bohm phase[2] due to the flux enclosed by the bent orbit segments, $\Phi_{\text{Berry}} = -\pi(1 - e^{-B/B_c^2})$ is the Berry phase, and $\Phi_0 = \pi$ is a constant phase due to reflections off the two *p-n* junction interfaces of the p cavity (smooth at middle and sharper at the contact side). Here at the critical field B_c, closed loops become dominant in transport, such that the Berry-Phase is picked up.[3] The contours sketched in Fig. 2e correspond to $j = 1, 2, \cdots, 8$.

---

[1]We calculate k_F as the numerical average of $\sqrt{\pi|n(x, y=0)|}$ within the p cavity. The cavity size L is numerically determined and is about half of the flake length $L/2 = 840$ nm.

[2]The loop area is given by $\delta A = R_c^2(\phi - \sin\phi)$ with $\phi = 2\arcsin(L/2R_c)$, and $R_c = \hbar k_F/eB$.

[3]The form of the Berry phase follows from the consideration of [129] with the critical field estimated by $B_c = (2\hbar k_F/eL)\sqrt{1 - T_c}$, where the critical transmission value T_c is a parameter close to one and does not significantly influence the shape of the contours; $T_c = 0.95$ is chosen.
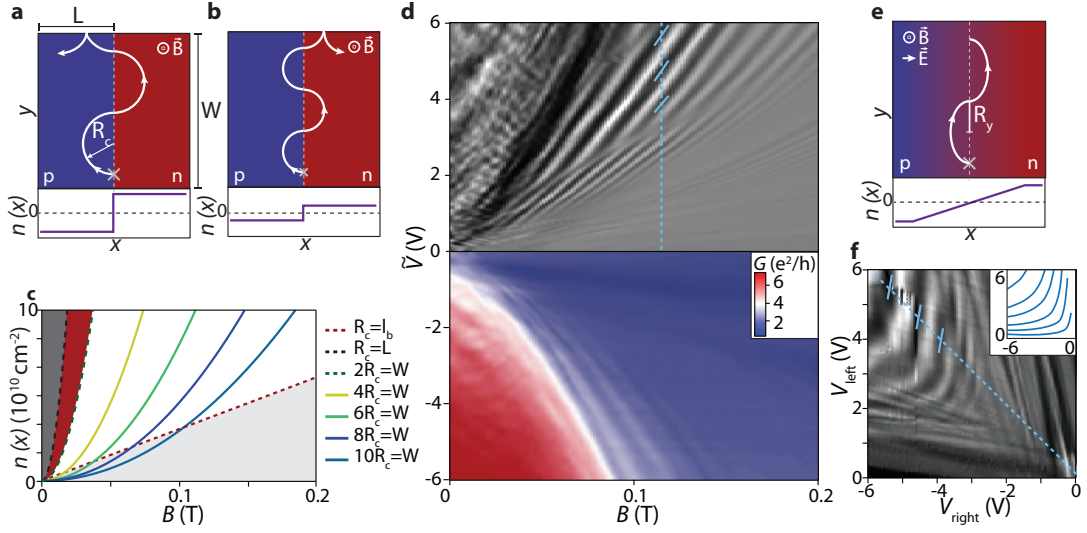
Figure 6.3.: **Parabolic-like conductance oscillations as a signature of snake states. a,** Charge carrier trajectory (white) along a sharp *p-n* junction in perpendicular magnetic field starting at the gray cross, where R_c is the cyclotron radius and $n(x)$ is the electron density. **b,** At lower p- and n-density R_c is reduced. In contrast to **a**, the trajectory results in current flow towards the right contact. **c,** Curves of constant R_c as a function of n and B. The continuous lines are given by the condition that the cyclotron diameter $2R_c$ is commensurate with the sample width $W = 2\ \mu$m. Snake states occur between the green dashed $2R_c = W$ and the red dashed $R_c = l_B$ line. The black dashed line indicates up to which field transport is dominated by bent Fabry-Pérot patterns (dark gray area). In the red area scar states can occur. Below the red dashed line R_c is smaller than the magnetic length l_B and Landau-levels start to dominate the transport (light gray area). **d,** Conductance as a function of antisymmetric gate tuning $\tilde{V}$ and magnetic field is shown in the lower panel, and its derivative dG/dB (in arbitrary unit) in the upper panel. Striking lines of high and low conductance with a parabolic like B-dependence can be observed. **e,** In a smooth *p-n* junction (here: linear $n(x)$) the cyclotron orbits become elongated along the *y*-direction due to the additional electric field caused by the density gradient. **f,** $dG(V_{\text{right}}, V_{\text{left}})/d\tilde{V}$ at 120 mT. The blue dashed lines in **d** and **f** are equivalent. The inset shows lines of constant electric field $\mathbf{E}_x$ at the *p-n* interface as a function of $V_{\text{right}}, V_{\text{left}}$ taken from electrostatic simulations.

6.3. Measurement of snake states

We now discuss the regime where snake states emerge. In Figure 6.3a a snake state at a sharp *p-n* junction is sketched. Consider a charge carrier trajectory starting at the gray cross with momentum **k** in $-x$ direction. Due to the magnetic field the trajectory is bent towards the *p-n* interface within the cyclotron diameter $2R_c = 2\hbar k/eB = 2\hbar\sqrt{n\pi}/eB$. If the trajectory hits the *p-n* interface, the hole will be transmitted to the n side with high probability due to Klein tunneling [38]. At the upper edge of the sample, the snake trajectory scatters at the left side, resulting in a current towards the left contact. At lower n, R_c is reduced. As sketched in Figure 6.3b, the snake trajectory scatters to the right at the upper edge, resulting in a net current towards the right contact. With this mechanism one expects conductance oscillations that depend on B and n, and constant conductance along curves where R_c is constant. In Figure 6.3c we display calculated functions $n(B)$ for constant R_c. Snake states occur once the cyclotron diameter $2R_c$ is smaller than the sample width W (green dashed curve) and can be described by quasiclassical trajectories as long as R_c is larger than the magnetic length $l_B = \sqrt{\hbar/eB}$ (red dashed line). In the regime $W > 2R_c > l_B$ additional parabolic lines show the condition for which the number of oscillations in the snake pattern is fixed and commensurate with W, i. e.. $m \cdot 2R_c = W$ with $m = 1, 2, 3, \dots$.

In Figure 6.3d we show the measured conductance $G(B, \tilde{V})$ (bottom) and its numerical derivative dG/dB (top). The measurement exhibits strong oscillations that follow parabola-like curves. We notice that the oscillations occur on a background of strongly decreasing conductance from $G \approx 6\,e^2/h$ to $G < 2\,e^2/h$. The steep decrease indicates that the transport becomes dominated by the low density region close to the *p-n* interface and this happens when $2R_c < W$.

In a real *p-n* interface the density does not sharply jump from the p to the n side but evolves smoothly. An electron trajectory in such a smooth *p-n* interface is sketched in Figure 5.2e. Here the density gradient leads to an electric field $\mathbf{E}_x$ and its interplay with the perpendicular magnetic field results in the so-called E×B drift (here along y), leading to elongated cyclotron orbits. The condition $R_y = const.$ can be studied in the measurement of Figure 6.3f where we show $dG(V_{\text{right}}, V_{\text{left}})/d\tilde{V}$ at $B = 120$ mT. The measured interference pattern follows curves of constant $\mathbf{E}_x$ at the *p-n* interface (obtained from electrostatic simulations) as shown in the inset.

6.4. Detailed analysis

So far we have seen that the oscillation pattern occurs in the regime where snake states are expected (i. e.. $2R_c < W$) and that the oscillations are related to transport along the *p-n* interface. We now present a quantitative comparison between experiment and theory. Figure 6.4a shows a quantum transport simulation of $G(B, \tilde{V})$ and $dG(B, \tilde{V})/d\tilde{V}$ based on a scalable tight-binding model [45] that fully takes into

account the device geometry. The simulation compares very well to the measurement shown in Figure 5.2d. The parabola-like patterns are reproduced and a similarly steep decrease of conductance is obtained. In Figure 6.4b a slice following the white dashed line in Figure 6.4a is shown. The visibility $\Delta G/G$ of the oscillations reaches 30% in theory and experiment and is enabled by the strong Klein collimation at the smooth *p-n*-interface.
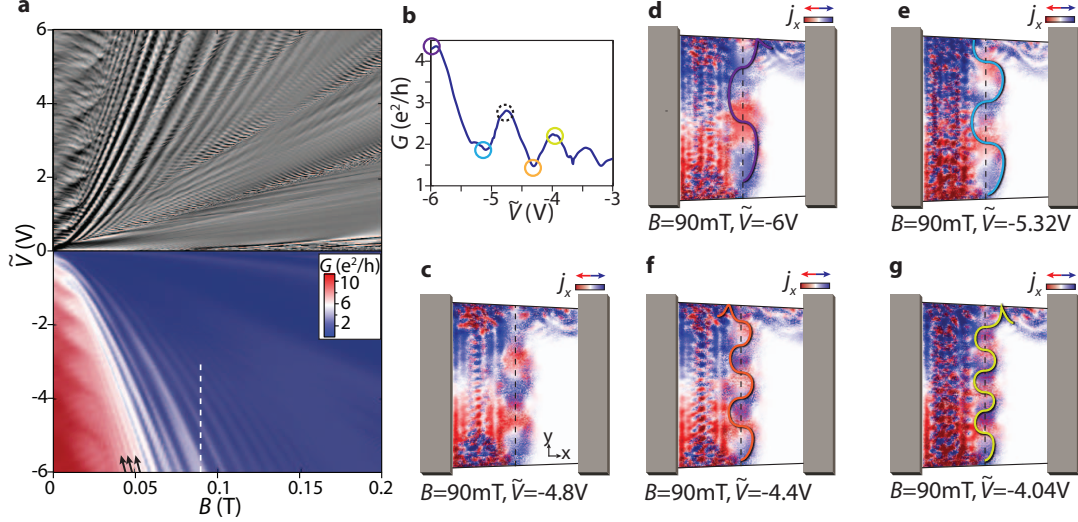

Figure 6.4.: **Tight-binding transport calculation reproducing the experimental results and local current density profiles revealing the snake states. a**, Tight-binding calculation of conductance $G(B, \tilde{V})$ (bottom) and its numerical derivative dG/dB (top, in arbitrary unit). The parabola-like lines seen in experiment are well captured. **b**, $G(\tilde{V})$ along the white dashed line in **a** at $B = 90$ mT. (**c**, Calculated x-component of the local current density distribution, j_x, for electrons injected from the left contact with a small DC-offset at $B = 90$ mT and $\tilde{V} = -4.8$ V (black dashed circle in **b**). The complex resonance pattern in the left cavity consists of "bubbling" trajectories that do not contribute to conductance. At the *p-n* interface (dashed line) an alternating current pointing to left (red) and right (blue) is observed. **d-g**, Current density profiles at different $\tilde{V}$ corresponding to the circles in **b**. As a guide to the eye, a snaking trajectory following j_x is added. From one conductance maximum to the next (i. e.. **c** to **g**) one snake period is added. The snake state in **e** and **f** corresponds to a conductance minimum and **c,d,g** to a maximum.

Next we apply the Keldysh-Green's function method to extract local current density profiles (see Appendix A.2) at high and low conductance along this line. In Figure 5.3c we show the x-component of the current density j_x, taken at $\tilde{V} = -4.8$ V (black

dashed circle in Figure 5.3b). The current is injected from the left contact using a small DC offset. In the left cavity a complex resonance pattern appears, given by so-called "bubbling" trajectories [130] which are reflected before reaching the *p-n* interface and do not contribute to current between the contacts. The pattern relevant for transport is located at the *p-n* interface (dashed line). We observe that j_x changes sign along the *p-n*-interface and that the blue and red regions penetrate the dashed line, indicating that transport is dominated by Klein-collimated snake trajectories. As a guide to the eye we added a curve in Figures 6.4d-g that follows the snake state. This is done for different $\tilde{V}$ values for which G is maximal/minimal at a fixed magnetic field of 90 mT (colored circles in Figure 6.4b). In Figure 6.4d for example, the current density profile corresponds to a conductance maximum where the current points to the right at the upper edge of the *p-n* interface. One period is added by changing $\tilde{V}$ from one maximum to the next. More current density profiles evolving with $\tilde{V}$ at fixed $B = 90\,\mathrm{mT}$ are shown in Supplementary Movie 1 of Reference [123]. By tracing along one of the parabolic-like patterns, the current density profile of the snake state stays constant (an example is given in Supplementary Movie 2 of Reference [123]).

The conductance oscillates as a function of the ratio $W/2R_y$, the exact snake period corresponding to $4R_y$ is, however, difficult to determine using quasiclassical trajectories, since current is injected from many points under various angles resulting in a complex cusp structure similar to what was predicted in References [131–134]. The excellent agreement between measurement and calculated conductance for which we could determine local current density profiles clearly indicates that the oscillations result from snake state trajectories.

To summarize, we investigated magneto-conductance of a ballistic graphene *p-n*-junction in the different magnetic field regimes. We have observed resonance patterns occurring in the intermediate quasi-classical regime in experiment and theory which result from the formation of snake states at the *p-n* interface. Among many other possibilities these states can be used to guide electrons on predefined paths with a high efficiency even at very low magnetic fields. This could be used to guide electrons away from sample edges to suppress uncontrolled momentum or spin-scattering. The directional scattering at the sample boundaries could be used to implement multi-terminal switches [133, 135]. Furthermore, the similarity between Andreev reflection and Klein tunneling is stressed in theory [136] leading to a correspondence of snake states and Andreev edge states which are of theoretical [102] and experimental [137] interest. Our work points out that snake states are highly tunable, occur at low fields and that ballistic graphene *p-n*-junctions in magnetic field reveal novel and intriguing phenomena.

6.5. Related studies

At the same time as the here presented work about snake states was published [123], ballistic snake states have been revealed in hBN encapsulated graphene in Refer-

ence [138]. The therein presented data was recorded at much higher fields ($B > 1\,\text{T}$) and carrier densities, which allowed the observation of snake states in a more disordered device ($\mu = 40,000\,\text{cm}^2\text{V}^{-1}\text{s}^{-1}$) on a longer scale. Additional temperature dependence could show that the conductance oscillations are stable up to $120\,\text{K}$ supporting that they are due to snake states rather than quantum interferences. In contrast, we supported our claims by tight-binding simulations, which are possible for the lower energy and B-field only in our case. The *p-n* interface has to be considered as a sharp in the case of Reference [138] since R_c is much larger than the smoothness of the *p-n* junctions, at least for the first few oscillations. For this reason, the magneto-conductance oscillations follow parabolic lines in their case since the cyclotron orbits are not elongated. For the same reason, the visibility of the interferences is much lower, i. e.. $\Delta G/G \approx 1\%$ compared to $\Delta G/G \approx 30\%$ in our case. This is on one hand due to the fact that the sharp *p-n* interface is rougher, washing out the conductance oscillations. On the other hand, the smooth *p-n* interface in our geometry provides strong filtering, enhancing the visibility by angular selection (similar to Chapter 5). In terms of electron-optics, we combine an array of lenses and filters along the *p-n* interface. The *p-n* collimators (or filters) correct for the imperfections of the magnetic lense.

Parabolic magneto-conductance oscillations have been further observed in *p-n*-p junctions in the high-magnetic field regime $B > 2\,\text{T}$ [139]. They were attributed to a Aharanov-Bohm like interference of edge states that travel on the left and right side of a *p-n* interface.

6.6. Conductance fluctuations related to Quantum Scars

We will now discuss a resonance pattern observed in the *p-n* cavity at weak magnetic field that has not been in focus of our publication [123]. Since we find that the pattern follows the Bohr-Sommerfeld quantization and that the corresponding closed loops are bouncing at the edges of the cavity we will discuss the possible relation to Quantum Scar states. These scar states have been discoverd in 1979 by McDonald and Kaufman who studied trajectories of a free particle moving in two dimensions with stadium-shaped boundaries [140]. They discovered that the eigenstates are highly concentrated on few orbits which are classically instable. Such orbits form due to quantum interference and are called scar states [141]. They obey a Bohr-Sommerfeld quantization rule [142], i. e. the accumulated phase is $\Delta\Phi/2\pi = \frac{1}{h}\oint \boldsymbol{p}\cdot d\boldsymbol{q} = N$, where N is an integer. In perpendicular magnetic field, $\boldsymbol{p} = \hbar\boldsymbol{k} + e\boldsymbol{A}$, and for an orbit of length L and area S, the interference condition is:

$$N = \frac{k \cdot L}{2\pi} + \frac{B \cdot S}{\phi_0},\tag{6.1}$$

where ϕ_0 is the magnetic flux quantum.

Experimental manifestations of scarred states were reported in microwave cavities [143,144] and in resonant tunneling diodes in large tilted magnetic fields [145,146]. Furthermore, in ballistic 2DEGs the stadium-shaped geometry was rebuilt. Scar states were identified by contacting the stadium with QPCs and measuring conductance fluctuations as a function of a weak perpendicular magnetic field [147]. With the rise of graphene, the question whether scar states would be also present in systems described by the Dirac rather than the Schrödinger equation was posed. By modeling a stadium shaped graphene quantum dot, scars could be identified [148, 149]. As a novel feature of graphene scars, their linear dependence on energy and the existence of chiral scars [150] was discussed. Chiral scars are due to electrons bouncing an odd number of times at the boundaries. They have to travel twice the trajectory to acquire a phase of 2π, whereas even scars travel only once.

Quantum interferences in graphene quantum dots in the presence of magnetic field have been discussed in Reference [151]. The dependence of interferences on magnetic field and energy and the transition from regular to irregular patterns in Reference [151] is very comparable to measurements that we present in the following. In Figure 6.5a, $dG/d\tilde{V}(B,\tilde{V})$ is shown for low magnetic fields, and in Figure 6.5b, the corresponding tight-binding calculation is revealed.[4] Large parts of this rich interference pattern have been already adressed, i. e.. the parabolic structure due to snake states and the Fabry-Pérot pattern at low fields. Here we focus on the intermediate regime.

In Figure 6.5c we show the oscillation amplitude $\Delta G(B)$ at $\pm 6\,\mathrm{V}$ and observe a transition from an irregular to a regular interference pattern at around $100\,\mathrm{mT}$. However, in contrast to Reference [151], the regular pattern is caused by the formation of snake states rather than the presence of only one LL in the system. We can see a regular pattern in our device even in the presence of many LLs due to the strong angular selection at the *p-n* interface. Even though a complex resonance pattern might be present in the cavities, only few trajectories are transmissive.

The irregular pattern in Figure 6.5c is caused by the coexistence different of interfering trajectories in the cavity. By looking at the grayscale of Figure 6.5a-b, their distinct behavior to gain additional insight. We have already explored the Fabry-Pérot pattern in weak magnetic field, however two additional sets of interferences can be identified. On the one hand, there are parabola-like structure, indicated with red arrows. The parabola-like behavior is a sign that the states are commensurate with a cavity dimension. They are therefore not due to trajectories forming closed loops since their transmission is influenced by the cyclotron radius only, similar to the snake states discussed above.

Very striking are the features that we indicate by yellow lines. Similar patterns are visible in the simulations of Reference [151]. The yellow lines are calculated using the interference condition 6.1 for a line length $L = 6.4\,\mu\mathrm{m}$ and enclosed area $S = 0.24\,\mu\mathrm{m}^2$. S and L have been identified by the periodicity of the oscillations

---

[4]Experimental and theoretical data was recorded for positive B only. It has been mirrored numerically around zero B to ease the understanding.
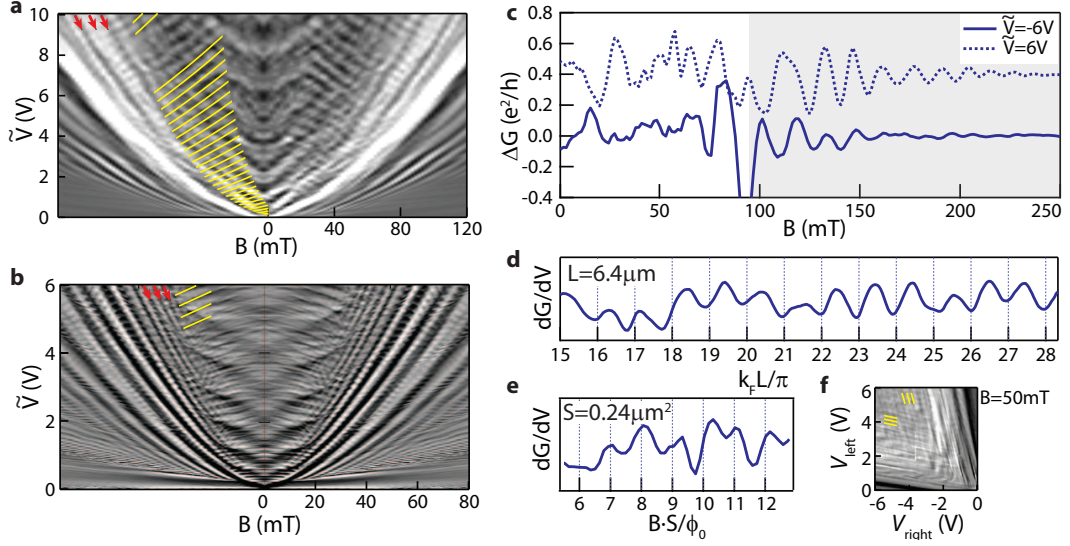
Figure 6.5.: **Measurement of scar states. a**, Two sets of resonances are indicated in this bipolar $dG/d\tilde{V}(\tilde{V}, B)$ measurement: Negatively dispersing states with yellow lines (calculated with Equation 6.1) and parabolic-like lines with red arrows. **b**, These resonances are reproduced in the corresponding tight-binding simulation. **c**, Oscillation amplitude $\Delta G(B)$ at $\tilde{V} = -6\,\text{V}$ and, offset by $0.4\,\text{e}^2/\text{h}$, at $\tilde{V} = 6\,\text{V}$. A transition from chaotic to regular oscillations (due to snake states) is observed. **d**, Cut in **a** perpendicular to the yellow lines and plotted as a function of $k_F L/2\pi$. A cavity length of $L = 3.2\,\mu\text{m}$ is observed. **e**, From the same oscillation pattern plotted as a function of $B \cdot S/\phi_0$ an area of $S = 0.24\,\mu\text{m}^2$ is extracted. **f**, The $dG/d\tilde{V}(V_{\text{left}}, V_{\text{right}})$ grayscale map at $B = 50\,\text{mT}$ shows that the tightly spaced resonances, labeled with yellow lines, are tuned by either the left or the right gate, i. e.. they are parallel to the dirac point in the left (right) cavity.

in k_F and in B, both of which are very regular as revealed in Figure 6.5d and e. From their occurrence in a gate-gate map $dG/d\tilde{V}(V_{\text{left}}, V_{\text{right}})$ we conclude that these resonances occur in either the left or the right cavity, since they are tuned by the two gates independently. The resonances are marked with yellow lines in Figure 6.5f.
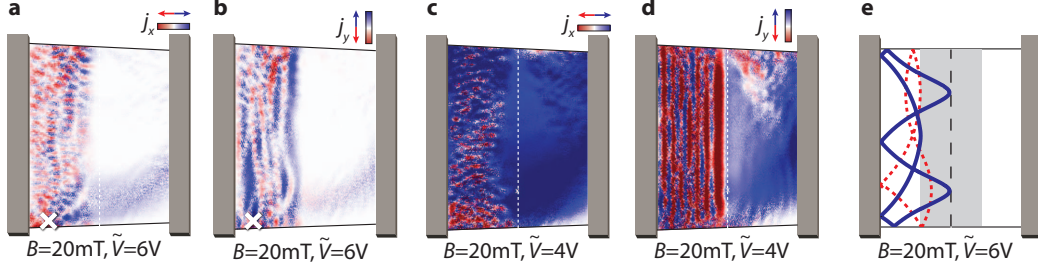

Figure 6.6.: **Current density simulations. a**, Local current density simulation at $B = 20\,\text{mT}$, $\tilde{V} = 6\,\text{V}$ for current injected at the white cross, showing current flowing in x-direction and in **b** the corresponding current in y-direction. **c**, In contrast to **a**, current is injected along the L contact. Nodes are observed both in j_x and in j_y in **d**. **e**, Numerically calculated quasiclassical trajectory forming a closed loop with $S = 0.24\,\mu\text{m}$ and $L = 6\,\mu\text{m}^2$. The density is smoothly changing from p to n in the gray area, the dashed line shows the *p-n* interface.

Scar states are typically studied regarding the spatial distribution of a given wavefunction. In Reference [148] for example, the electron concentration in a stadium shaped graphene reveals a nodal pattern. The scars are identified by connecting the spots of highest electron concentration with straight lines. Naturally, the number of nodes N along such a path is given by the interference condition in Equation 6.1. We have already used the local current density distribution to characterize snake states. Here we can use the same tool to visualize the interfering states, therefore j_x and j_y in the regime of the yellow interference pattern are shown in Figure 6.6. In Figure 6.6a-b current is injected at the white cross only, whereas in c and d injection is from the left contact. There is a complex and elongated nodal pattern building up in the left cavity. The nodes are indicative for scarred trajectories, i. e.. along closed loops, such nodes appear.

In order to extract possible loops, we calculated quasi-classical trajectories for the corresponding densities and magnetic fields, one of which we show in Figure 6.6e. To model the smoothness of the junction, the density is linearly changing from n to p in the gray area. The area and length of the shown trajectory is of the right order, i. e. $L = 6\,\mu\text{m}$ and $S = 0.24\,\mu\text{m}^2$, it forms a closed loop and it could be sufficiently transmissive, since it comes close enough to the *p-n* interface. There are apparently a multitude of closed trajectories possible, most of which however are not seen in the transmission from left to right contact since they bounce only in the left cavity without transmitting. The extracted long L and small S indicates that the

corresponding trajectories bounce at all boundaries and encircle areas both clock- and counterclockwise, such as the trajectory we presented. Such intersecting loops are dominant in this region where R_c is still large but small enough such that direct trajectories from the contact to the *p-n* interface are non-transmissive. In contrast to the Fabry-Pérot resonances, which bend "upwards" in the $(\tilde{V}, B)$-map (Figure 6.5a-b), the here discussed resonances bend "downwards" since the magnetic flux is encircled in the opposite direction. This is due to bouncing off all four boundaries in the latter case, which becomes dominant if B is sufficiently large. As an additional indication we observed that if the injecting contact is non-reflective in the simulation the resonances disappear.

To conclude this part, we have observed single-cavity resonances in weak magnetic field that follow the Bohr-Sommerfeld quantization and we have extracted an area and a length for these patterns. Despite the fact that it is difficult to identify the right trajectory we show here that trajectories fulfilling the requirements (with respect to L, S, closed loop, sufficiently transmissive) exist and that such trajectories form a nodal pattern as seen in Figure 6.6a-d. The discussion about the underlying classical dynamics (chaotic, integrable, mixed) is beyond the scope of this thesis. However the observation of this cavity-bound state in weak magnetic field as well as the detection mechanism using the *p-n* interface is novel. We use the strong angular selection of the smooth *p-n* interface to select few trajectories that can be seen in transport from left to right contact.

7

Guiding of Electrons in a Few Mode Ballistic Graphene Channel

In this chapter and in Reference [152] we demonstrate control of graphenes' charge carriers by an electron-optical element: a waveguide, in which the transmissivity is tuned by the wavelength. The reflection, refraction and transmission behavior of graphene's massless charge carriers in a spatially varying potential is analogous to the propagation of an electromagnetic wave in media with varying refractive index. Optical fibers (OFs) consist of materials that are assembled in a way that the refractive index in the light-carrying core is larger than the refractive index in the coating. Similar conditions can be achieved in graphene using local gates. The possibility to form electronic waveguides in graphene has attracted a lot of theoretical interest [13, 136, 153–158]. However, experiments were performed only in rather diffusive samples [99], making the comparison to optics difficult. In addition, a graphene waveguide is expected to show a distinct behavior once a *p-n* interface is involved. Due to the additional confinement of such an interface it is possible to transport one or few modes in a waveguide. In optics, single mode fibers are used for long distant communication since they are not limited by modal dispersion. In a similar way single or few-mode electron-optic fibers can be beneficial for quantum information communication.

So far, confinement of charge carriers has been mainly achieved with hard-wall potentials, as provided by the edges in graphene-nanoribbons [159–163] or the induced gap in bilayer graphene [94,164]. Whereas the former suffers from irregular edges, the latter is performed in gapped bilayer graphene which does not host the relativistic Dirac particles. Even though electrons were successfully guided in the bulk of single-layer graphene by making use of snake states (Chapter 6 and [123, 125, 138]) their transport properties is significantly altered by the involved perpendicular magnetic field. It is a different and very challenging task to confine graphene charge carriers in an electrostatic waveguide [156, 158]. In this chapter we report on the formation of a narrow tunable ballistic electrostatic channel in graphene, that can be operated

as an optical fiber. By depleting the channel, a reduction of mode number and steps in the conductance are observed, until the channel is completely emptied. The measurements are supported by tight-binding transport calculations including the full electrostatics of the sample.
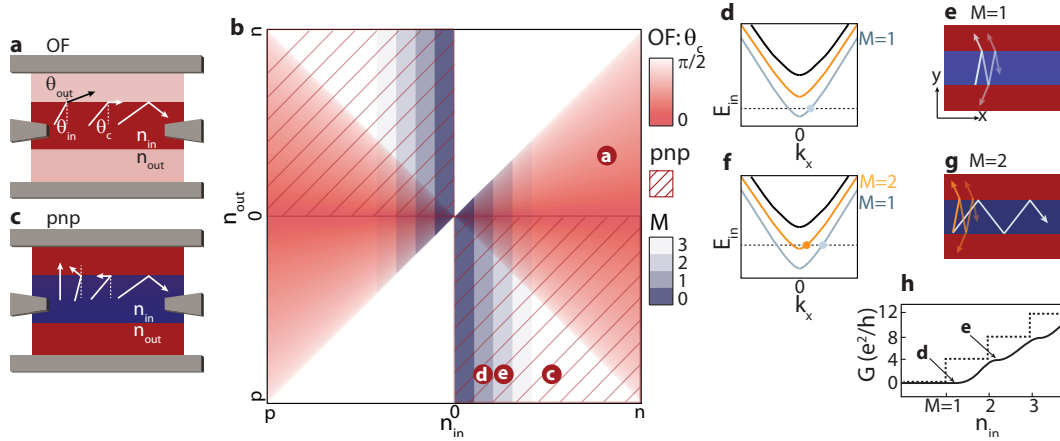
7.1. Basic considerations

Figure 7.1.: **Guiding mechanisms related to densities in n_{in} and outside n_{out} of an electrostatic channel. a**, Possible design of a guiding channel where the gray areas are electrical contacts. If the electron density inside a channel is larger than outside $n_{in} > n_{out}$, electron trajectories reaching the interface under an angle θ_{in} larger than the angle of total internal reflection θ_c stay in the channel, similar to an optical fiber (OF). **b**, The different guiding mechanisms are sketched depending on n_{in} and n_{out}. In the red shaded triangles OF guiding is present. The shading visualizes $\theta_c(n_{in}, n_{out})$. The hatched quadrants indicate the regions of *p-n* guiding and the blue steps correspond to different mode number M in the channel. **c**, The formation of a *p-n* junction helps to keep charge carriers in the channel; loss is due to trajectories with (almost) zero angle of incidence. **d**, Sketch of a band diagram in the channel for the situation, when the first mode ($M = 1$) is populated. The small value for k_x will lead to leakage as sketched in **e**. **f**, By increasing the Fermi-energy E_{in} the second mode becomes available and k_x of the first mode is increased. The first mode can be guided in the channel, as illustrated in **g**. **h**, Due to this mechanism, the expected conductance plateaus will be smoothened and shifted with respect to M compared to the situation of a hard-wall channel (dashed line). They are still expected to occur at values of $4e^2/h$.

As introduced in Chapter 2.2.1, the Fermi energy E_F in graphene takes the role

of the refractive index. By changing this energy using local gates, a waveguide can be formed. This guiding principle and a possible geometry is shown in Figure 7.1a. With Snell's law $E_{\text{in}} \cdot \sin(\theta_{\text{in}}) = E_{\text{out}} \cdot \sin(\theta_{\text{out}})$, the critical angle for total internal reflection is simply given by $\theta_{\text{c}} = \arcsin(E_{\text{out}}/E_{\text{in}}) = \arcsin(\sqrt{|n_{\text{out}}|/|n_{\text{in}}|})$. For small density ratios $|n_{\text{out}}|/|n_{\text{in}}|$, the resulting small θ_{c} will keep electron trajectories very efficiently in the channel. In Figure 7.1b we plot θ_{c} as a function of the densities in- and outside of a channel. Negative densities correspond to hole-like, positive to electron-like transport. The resulting red shaded triangles correspond to the region where OF guiding is possible.

In addition to this OF guiding, charge carriers in graphene can also propagate in a channel that has interfaces at which the polarity of the charge carrier is inverted. Such a channel can be formed by tuning the channel region to electron-like (n) and the outer region to hole-like (p) doping, or *vice versa* as indicated by the hatched quadrants in Figure 7.1b [125]. Since at a *p-n* interface the density is zero, it is naturally reflective. If the transition from *p-* to *n*-doping is gradual, the low-density region is increased in size leading to an even more reflective interface. In other words, a smooth *p-n* interface can guide electrons more efficiently than a sharp one. Losses out of a *p-n* channel are in both cases mostly caused by trajectories perpendicular to the interface that are transmitted with probability one as sketched in Figure 7.1c.

At low densities n_{in}, the wavelength in the channel is such that $\lambda/2$ becomes larger than the channel width W. This situation of a depleted channel is sketched in the dark blue region in Figure 7.1b. By increasing n_{in}, the local Fermi-energy E_{in} increases such that the first mode $M = 1$ in the channel can be populated, as shown in the sketch of the band-diagram in Figure 7.1d. Yet, due to the low value of the wavevector k_{x} in propagation direction x, the angle of incidence at the *p-n* interface is close to perpendicular and the mode will leak out of the channel (Figure 7.1e) and cannot be observed in transport along the channel. Nevertheless, by increasing E_{in}, k_{x} increases and the angle of incidence towards the *p-n* interface becomes larger. A corresponding band-diagram is sketched in Figure 7.1f, where already the second mode ($M = 2$) is available. In this situation, the first mode can be guided and the second mode leaks out of the channel since the Fermi-energy crosses this band at low k_{x}. Compared to a channel where the outer regions are forbidden for electrons, the expected conductance plateaus for transport along the channel will be smoothened due to the above discussed mechanism. We still expect conductance steps at $4e^2/h$, as sketched in Figure 7.1h. A more detailed analysis of the band structure is given in Section 7.6.2.
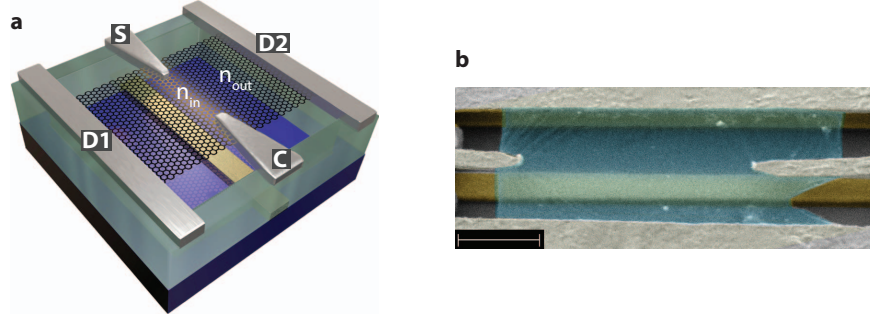
Figure 7.2.: **Realization of a guiding channel in a suspended graphene device. a**, 3-dimensional design of the device. Tuning the density in the channel (n_{in}) with the bottomgate (gold) and the density outside of the channel (n_{out}) with the backgate (blue), the electrons can be guided between the source (S) and the collector (C) contacts. The losses are recorded at side drain contacts D1 and D2. **b**, False-colored SEM image of the measured device; scale-bar: $1\,\mu$m.

7.2. Design and characterization of the device

We realized an electrostatic channel in a four-terminal suspended graphene device. A 3-dimensional design is shown in Figure 7.2a. By applying a voltage to the backgate (blue) and bottomgate (gold), the density can be tuned locally to guide electrons between the source (S) and collector (C) contact. The guiding losses can be measured at the side drain contacts (D1, D2). A scanning electron micrograph of the measured device is given in Figure 7.2b. The graphene flake is roughly $4 \times 2\,\mu\text{m}^2$ in size. The fabrication is given in Chapter 4. Graphene is cleaned by in-situ current annealing between the D1 and D2 contact.

As a first characterization the conductance G_{D1D2} between D1 and D2 is measured while the S and C contacts are floating. We correct for the capacitive cross talk between backgate and bottomgate voltage and plot the data as a function of channel densities n_{in} and n_{out}. The conversion from voltage to density is given by the gating efficiency which we extracted from the electrostatic simulation (for details, see Appendix A.4). In the colorscale-map of Figure 7.3a, the conductance drops drastically once a *p-n* junction is formed (i. e. the blue regions). Figure 7.3b shows the field effect along uniform doping which reveals a pronounced Dirac point. The very sharp transition from the unipolar to the bipolar region occurs within $n_{in} \approx 10^9$ cm^{-2}. This demonstrates the very high quality of the graphene. In addition, the regular Fabry-Pérot pattern (marked with arrows and sketched in the inset of Figure 7.3a) indicates ballistic transport in the channel [66,67].
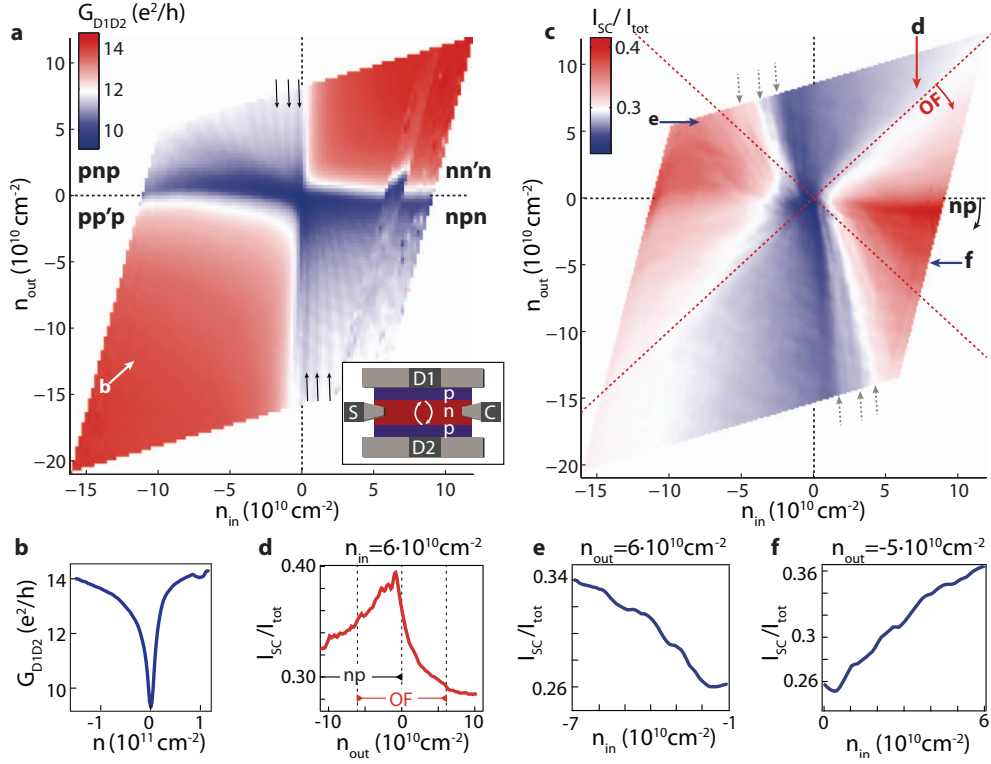
Figure 7.3.: **Experimental results: Fabry-Pérot interferences across the channel and guiding efficiency along the channel. a**, Two-terminal conductance G_{D1D2} between D1 and D2 as a function of the densities n_{in} and n_{out} (S and C are floating). The resonances marked with black arrows are due to Fabry-Pérot interferences in the channel as sketched in the inset. **b**, Field-effect as a function of uniform doping (cut along white arrow in **a**). **c**, Guiding efficiency $I_{\text{SC}}/I_{\text{tot}}$ as a function of n_{in} and n_{out}. Here, an AC voltage is applied to the S contact and current is measured simultaneously at C and D1, D2. **d**, Cut in **c** at fixed $n_{\text{in}} = 6 \cdot 10^{10} \, \text{cm}^{-2}$. The guiding efficiency increases drastically in the OF regime and is highest when *p-n* and OF guiding coexist. **e**, The cut in **c** around $n_{\text{out}} = 6 \cdot 10^{10} \, \text{cm}^{-2}$ reveals steps in the guiding efficiency that are due to mode filling of the channel. Shown is an averaged curve of $n_{\text{out}} = 5...7 \cdot 10^{10} \, \text{cm}^{-2}$. The steps are seen in the 2D plot in **c** and are marked there with gray vertical arrows. **f**, A similar cut at $n_{\text{out}} = -4... - 6 \cdot 10^{10} \, \text{cm}^{-2}$ reveals steps also for inverted polarity.

72

7.3. Measurement of Guiding efficiency

We now discuss the guiding efficiency measurement (Figure 7.3c). An AC voltage is applied to the S contact and current is measured at C, D1 and D2 using an IV-converter and a Lock-In detector on each terminal. The guiding efficiency $\gamma = I_{SC}/I_{tot}$ is then given by the current I_{SC} measured at C divided by the total current $I_{tot} = I_{SD1} + I_{SD2} + I_{SC}$. It is important to notice that γ includes the injection efficiency into the channel which is limiting the overall maximum efficiency to 42% in this device. In this complex geometry it is not possible to discriminate the losses of the channel itself from losses due to poor coupling of the charge carriers into the channel. The colorscale map $\gamma(n_{in}, n_{out})$ shows high guiding efficiency in the expected regions: A large γ is observed in the OF triangles, and the efficiency is even increased once a *p-n* junction is formed. This is best seen by taking a cut at $n_{in} = 6 \cdot 10^{10}$ cm^{-2} shown in Figure 7.3d and indicated by a red arrow in Figure 7.3c. Charge carriers cannot be guided for $n_{out} > n_{in}$, and for uniform doping ($n_{out} = n_{in}$) roughly 29% of the charge carriers reach the C contact. In the OF regime, the efficiency increases drastically and reaches its maximum if the outer region is depleted, i. e. $n_{out} \approx 0$. The formation of a *p-n* interface leads to an increased γ compared to the regime where only OF guiding is present. Even though OF and *p-n* guiding mechanisms have been discussed for a diffusive sample in Reference [125] here we demonstrate their occurrence in the expected regions in a density-density map of a ballistic sample.

The lowest efficiency in the colorscale map (Figure 7.3c) is observed in the empty-channel region (dark blue). A step-wise increase of γ starting from the depleted channel towards larger n_{in} is seen in the colorscale map. By taking cuts around $n_{out} = 6 \cdot 10^{10}$ cm^{-2} plateaus corresponding to a change in mode number M become apparent (Figure 7.3e). For this cut we averaged the curves between $n_{out} = 5...7 \cdot 10^{10}$ cm^{-2} to wash out features that are changing with n_{out}. More details on these features are given later in the manuscript. The plateaus are also present at the opposite polarity, i. e. an *n*-doped channel and a *p*-doped outer region. They can be seen for example in cuts around $n_{out} = -5 \cdot 10^{10}$ cm^{-2} in Figure 7.3f.

7.4. Tight binding simualtion

For a comprehensive understanding, we compare the experiment to transport calculations based on an ideal electrostatic model obtained by finite-element simulations following the gating and graphene flake geometry of our device. Using the scalable tight-binding model for graphene [45], the full 4×2 μm^2 flake with realistic on-site energy profiles $V(x, y)$ from the electrostatics can be considered (Appendix A.2). The main features of the guiding efficiency map can be reproduced by applying the real-space Green's function method to compute the conductance (Section 2.3.3). The results of the simulations are shown in Figure 7.4a. The main features of the measurement are well captured: There is a high guiding efficiency in the OF triangles
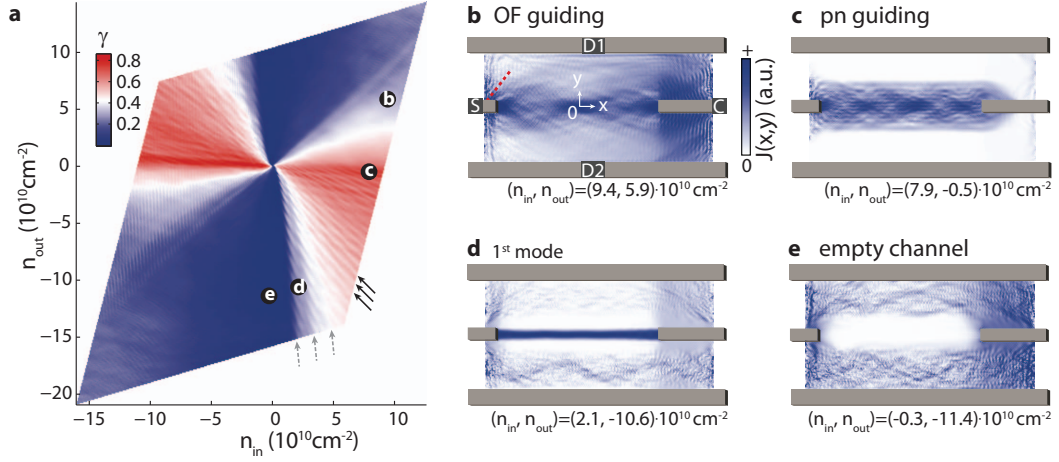
Figure 7.4.: **Simulated guiding efficiency and local current density profiles based on tight-binding model. a**, Calculated guiding efficiency following the same definition as the experiment, $\gamma = I_{SC}/I_{tot}$, using 3-dimensional electrostatics given by the geometry of the device. Sequential mode filling of the channel is indicated by gray dashed lines. Black arrows mark a resonance pattern involving the inner cavity formed by the narrow channel and an outer cavity given by one outer contact D1, D2 and the channel. **b**, Local current density distribution for a small applied voltage on the source contact S. The densities are tuned to the optical fiber regime. The red dashed line shows the angle of total internal reflection. **c**, In the *p-n* regime, the electrons are kept inside the channel very efficiently and complex resonance patterns are observed. Close to the S contact, current is lost towards D1 and D2 due to Klein tunneling. **d**, Local current distribution for the first mode. **e**, At vanishing n_{in}, the channel can be emptied, i. e., the local current density is zero inside the channel.

which is even increased in the *p-n*-p-regime. We see a very low efficiency at low n_{in} where the channel is empty.

The emerging modes confined in the channel are observed along lines indicated by gray dashed arrows in Figure 7.4a. Additional resonances (indicated by black arrows) in the *p-n-p* regions appear and will be referred to as two-cavity resonances. They are related to states spatially extending over both the inner channel and the cavity regions confined by D1 and D2. They are therefore influenced by both n_{in} and n_{out} and are roughly parallel to the anti-diagonal in the density map.

From the simulations we further extract the space-resolved local current density $\mathbf{J} = J_x\mathbf{e}_x + J_y\mathbf{e}_y$ in the different guiding situations by applying a small DC voltage difference between the S and C contact with D1 and D2 grounded. In Figure 7.4b we plot $J(x, y) = [J_x^2(x, y) + J_y^2(x, y)]^{1/2}$ in the optical fiber regime ($|n_{\text{in}}| > |n_{\text{out}}|$). Most current propagates in a channel towards the right contact. The loss (i. e. current towards D1 or D2) is given by trajectories injected at S that reach the interface close to normal incidence. For the given densities we obtain $\theta_c = 52°$ and we sketch a corresponding dashed line in the Figure. By the formation of a *p-n*-interface this loss is reduced drastically as shown in Figure 7.4c. Outside the channel, the current is almost completely suppressed. Only close to the injector contact a loss current is observed, corresponding to trajectories aligned perpendicular to the channel border. For smooth *p-n*-junctions, this is exactly what is expected [38] due to strong Klein collimation. Inside the *p-n* channel, a complex interference pattern forms. By reducing the density in the channel only the first mode is filled (Figure 7.4d) and as a consequence the complex interference pattern of Figure 7.4c disappears. Even though the channel appears to be lossless, the injection into the single-mode channel is rather inefficient, i. e. there is a number of modes outside the channel that can be populated. For this reason the current density in the outer cavity does not disappear completely. By further reducing n_{in}, the channel can be emptied completely, as it becomes apparent in Figure 7.4e.

7.5. Conductance steps due to mode filling

We now show in Figure 7.5a-c the conductance between source and collector in the interesting region of biploar doping where the channel is close to full depletion and plateaus in the conductance can be expected due to quantized filling. In Figure 7.5a and b several curves $G_{\text{SC}}(n_{\text{in}})$ are given for values of $n_{\text{out}} = 5...7 \cdot 10^{10}$ cm^{-2}. They are offset from the red curve by multiples of $n_{\text{in}} = 0.4 \cdot 10^{10}$ cm^{-2}. The plateaus due to mode-filling are indicated by dashed lines and we mark the additional two-cavity resonances by the black arrows. A similar structure is observed for opposite polarity (Figure 7.5b).

Although Fabry-Pérot resonances and mode filling occur on the similar length and energy scale they can be distinguished by their different gate behaviour. The observed pattern is reproduced clearly in the tight binding simulation for $G_{\text{SC}}(n_{\text{in}})$ shown in
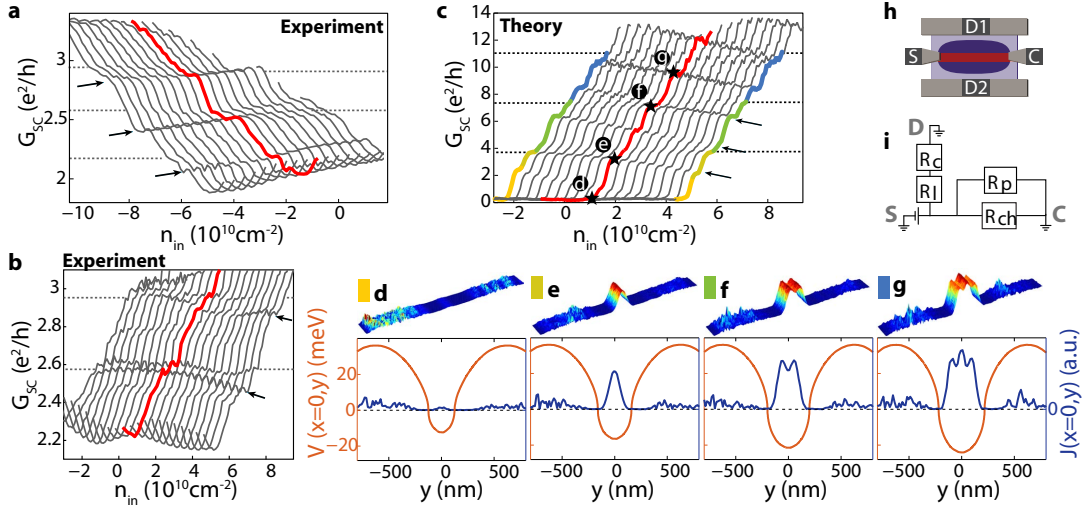
Figure 7.5.: **Discrete change of the number of modes in experimental and theoretical conductance data. a**, Steps corresponding to mode-filling are seen in the experimental $G_{SC}(n_{in})$ data at fixed $n_{out} = 5...7 \cdot 10^{10} \text{cm}^{-2}$. The curves are offset from the red line by $n_{in} = 0.4 \cdot 10^{10} \text{cm}^{-2}$. Mode filling (see Figure 7.1h) occurs along the dashed lines and an additional two-cavity resonance pattern is indicated by the black arrows. **b**, A comparable pattern, yet less clear, is observed for inverted polarity. **c**, The calculated $G_{SC}(n_{in})$ curves reveal the plateaus, indicated by black dashed lines, and the two-cavity resonance pattern (black arrows). **d**, Local band offset $V(y)$ (orange curve) in the middle of the channel $x = 0$. Blue curve: corresponding local current density $J(x = 0, y)$. Top panel: $J(x, y)$ for x close to 0. For the given density profile the channel could carry one single mode $M = 1$, which however is leaking out drastically such that almost no current is transported. The plots **d-g** are taken at the density marked by a star in **c** but are representative for the respective conductance regimes marked by colors in the outer two curves in **c**. **e**, As the channel gets deeper and wider, the first mode can be transported in the channel. **f,g**, The second and third mode appear when $|n_{in}|$ increases further. **h,i**, A model explaining the occurrence of the conductance plateaus at 2.2, 2.6 and $2.9e^2/h$ in **a**. Regions that are doped by absorbates are colored in light blue. The channel resistance R_{ch} is then not only given by $1/(N \cdot 4e^2/h)$ but modified by a transmission probability t into and out of the channel. Additionally, current can flow from S to C through the outer cavities, which is modeled by a parallel resistor R_p. The measured resistance between S and C is then given by $R = (1/(t^2 \cdot N \cdot 4e^2/h) + R_p)^{-1}$. The loss resistance from S to D, R_l, is modified by a contact resistance in series R_c. If we calculate $G'_{SC} = 1/R_{ch}$ at $n_{out} = 5 \cdot 10^{10} \text{cm}^{-2}$ for $R_p = 13.4 k\Omega$ and $t = 0.32$ the plateaus occur at 0, 4, 8 and $12e^2/h$.

Figure 7.5c. Again the flat plateaus are marked with dashed lines and the dispersing resonances are indicated by arrows. Comparing to Figure 7.4a we confirm that the resonances indicated by the black arrows correspond to the above mentioned two-cavity resonances whereas the plateaus indicated by horizontal dashed lines are due to an increase of the channel mode-number. These plateaus occur at roughly 4, 8 and 12 e^2/h here. Compared to the two-cavity resonances they do not disappear if the side contacts (D1 and D2) are transparent, as we will discuss in Section 7.6.1. The number of modes M in the middle of the channel ($x = 0$) can be read off from the number of peaks in $J(x = 0, y)$ in Figures 7.5d-g, where the potential landscape $V(x = 0, y)$ from the electrostatics is also shown. On top, the $J(x, y)$ profiles for x close to 0 are given. The positions where the profiles were imaged are labeled with stars in Figure 7.5c, and their shape is representative for the whole respective conductance range marked by colored lines in Figure 7.5c. The $V(x = 0, y)$ profiles reveal that the density is gradually changing from n outside to p inside of the channel. The smoothness in the potential landscape is due to the large distance of ≈ 400 nm between the graphene and gate electrodes. The channel formed by the potential in Figure 7.5d can transport only one mode, but since k_x is small and since the channel is very leaky for small angles as explained in Figure 7.1d-e., only a vanishing current is observed in the middle. By increasing the voltage on the inner gate, the minimum in the potential profile $V(x = 0, y)$ decreases and the channel grows wider such that electrons gain momentum in x-direction and the first mode can be transported along the waveguide (Figure 7.5e). By further increasing the inner gate voltage, the second mode, $M = 2$ (Figure 7.5f), and third mode, $M = 3$ (Figure 7.5g), also become available for charge transport along the channel.

Having confirmed the origin of the non-dispersing features in the experiment we now compare the conductance values. In the experiment, the plateaus do not occur at $G'_{\text{SC}} = N \cdot 4\,e^2/h$ (with $N = 0, 1, 2, ...$) but rather at $G_{\text{SC}} = 1.9$, 2.2, 2.6 and $2.9\,e^2/h$ in Figure 7.5a. A simple model, depicted in Figure 7.5h-i, explains this deviation by taking into account non-uniform cleanliness of the graphene. In Figure 7.5h regions that are presumably doped by absorbents on the surface are shaded with light-blue color. Such a distribution of dopants is likely to occur after current annealing since the contacts act as heat sinks and therefore attract residual absorbents when graphene is hot [49]. In a simple resistor network (Figure 7.5i) we therefore model an additional resistor R_{p}, due to trajectoires from S to C that do not penetrate the channel, in parallel to the channel resistance R_{ch}. In addition, the injection into the channel and the detection at the collector will be modified by a transmission probability t which is the transmission from the contact into and out of the channel. Therefore, $R_{\text{ch}} = 1/(t^2 \cdot N \cdot 4\,e^2/h)$ and the measured resistance between S and C will be $R = (1/R_{\text{ch}} + 1/R_{\text{p}})^{-1} = 1/G_{\text{SC}}$. For the $G_{\text{SC}}(n_{\text{in}})$ curve at $n_{\text{out}} = 5 \cdot 10^{10}\,\text{cm}^{-2}$ plateaus at $G'_{\text{SC}} = 0$, 4, 8 and $12\,e^2/h$ are obtained for $R_{\text{p}} = 13.4\,\text{k}\Omega$ and $t = 0.32$. By subtracting a contact resistance $R_{\text{c}} = 2.9\,\text{k}\Omega$ from the loss conductance G_{SD1D2}, we find guiding efficiencies $\gamma = G'_{\text{SC}}/(G'_{\text{SC}} + G'_{\text{SD1D2}})$ of $26\%, 41\%$ and 51% for the first, second and third plateau. R_{c} is extracted for high, unipolar densities in the G_{SD1D2} map (shown in the Appendix A.4). The values compare well to the simulation (Figure
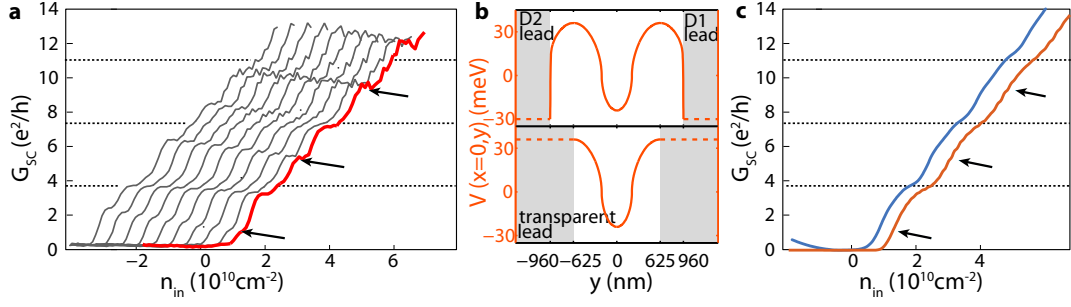
Figure 7.6.: **The two-cavity resonances disappear once the outer leads D1 and D2 are transparent. a**, A similar plot as shown in the main text (Figure 5c) showing calculated conductance G_{SC}. The plateaus due to mode-filling occur along the dashed grid lines, the two-cavity resonances are marked with black arrows. **b**, Potential profiles $V(x = 0, y)$ as used in the main text (upper) and idealized such that reflections at the outer D1 and D2 contacts are suppressed (lower). **c**, For an idealized profile the two-cavity resonances do not occur anymore. The plateaus for mode-filling are seen for a 3 μm (orange) and a 500 nm (blue) long channel.

7.4a) where $28\%, 39\%$ and 46% are obtained.

Apparently the main limitation in the experiment is the injection and detection efficiency, which is parametrized in t. In the simulation we find $t = 0.96$ by applying the same resistor model which is a factor of 3 larger than in the experiment, where $t = 0.32$ is found Improvements would focus on creating excellent contact to the graphene. This would, on one hand, increase t both at the source and collector contact. On the other hand, a reduction of R_p could be expected since the D1, D2 contacts would be less reflective, i. e. trajectories from S that get reflected at D1 and enter C could be suppressed. A strategy to increase t by shaping the graphene is discussed in the Section 7.6.3.

In the simulation, however, t is large meaning that the ideal channel very efficiently transports modes once k_x is sufficiently large. This efficient guiding is only possible due to the smooth *p-n* interface in our device [156] which is very reflective for larger angles of incidence θ. For comparison, a sharp *p-n* interface transmits trajectories with $\theta = 45°$ with 50% probability [38] such that the mode sketched in Figure 7.1g could not be guided. For our smooth interface, on the other hand, 50% transmission is obtained for only $\theta \approx 20°$, and at 45° the transmission is close to zero. These values are taken for $(n_{in}, n_{out}) = (5, -10) \cdot 10^{10} \, \text{cm}^{-2}$. For details see Figure 2.6 in Chapter 2.2.3.

7.6. Additional information

7.6.1. Two-cavity resonances

The two-cavity resonances, which we mark with black arrows in Figures 7.4a-b and Figure 7.6a are due to resonances that are tuned by both densities n_{in} and n_{out}. For these resonances, reflections at the side contacts D1 and D2 are required. By modifying the potential profile as shown in Figure 7.6b and simulating transparent (non-reflective) leads, the two-cavity resonances on the G_{SC} curves indeed disappear (Figure 7.6c). The position where they appear in the realistic device simulation are marked with black arrows. The shoulders close to 4,8 and $12\,e^2/h$ remain clearly visible. In this idealized simulation, the source and collector contacts are set to be μm apart similar to the real device (orange curve). Additionally we also show a test where the S and C contacts are 500 nm apart (blue curve).

7.6.2. Bandstructures

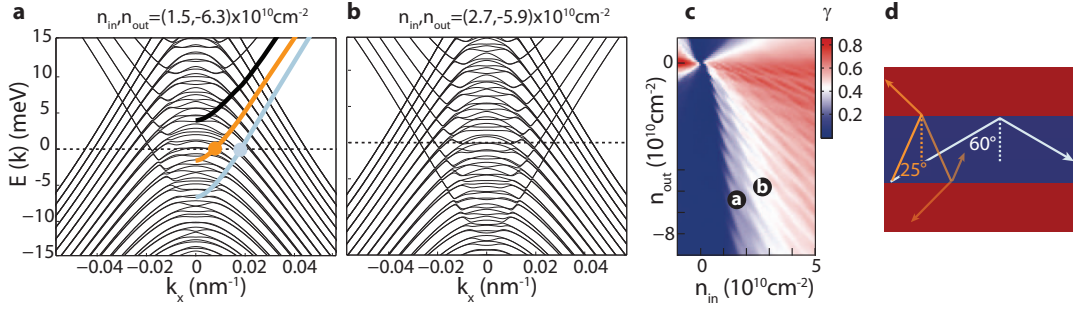

Figure 7.7.: **Calculated band structures for translational invariance along x. a-b**, Band structures $E(k_x)$ when the first mode appears in transport (a) and for two modes (b). **c**, The corresponding positions are labeled on the calculated $\gamma(n_{in}, n_{out})$ map. **d**, The maximum angles of incidence to the *p-n* interface are sketched for the two different modes.

In Figure 7.1f we sketched a simplified band structure for the modes in order to illustrate the leakage of the guided modes with short k_x. A more evolved picture is presented in Figure 7.7a-b, where we show band structures $E(k_x)$ calculated by taking a unit cell laterally cut (along y) from the simulated graphene lattice at around $x = 0$. The flake is oriented such that the armchair edge is parallel to the *p-n* interface. The band structures are given for different densities n_{in}, n_{out} and the corresponding position is labeled in the guiding efficiency map, shown in Figure 7.7c. The band structures mainly consist of two Dirac cones. The one for hole-like transport at the Fermi energy corresponds to the outer cavities. Since n_{out} is changing only little from Figure 7.7a-c, this part of the band-structure remains unchanged. Due to the rather high density, there is a large number of modes available. More interesting are the

modes that appear in the inner cavity, corresponding to electron-like transport. In Figure 7.7a we overlay curves that lead to the simplified picture shown in 7.1f by neglecting the fine-structure at low k_x. We would expect to observe two modes in transport along the channel for Figure 7.7a due to the orange and the blue branch. However, by calculating $k_y = \sqrt{k^2 - k_x^2}$ for $k = \sqrt{n_{\text{in}}\pi} = 0.022$ nm^{-1} we obtain an angle of incidence of 60° for the blue and only 25° for the orange mode (Figure 7.7d). Comparing to the numbers given in Figure 2.6 for transmission at a smooth *p-n* interface it becomes apparent why in transport along the channel only one of the modes is seen: the smaller angle of incidence for the second (orange) mode leads to leakage out of the channel, whereas the first (blue) mode can be guided efficiently.

7.6.3. Measurements on further devices

In an effort to reduce the injection losses of the channel we also fabricated samples that were etched at the sides, such as the one shown in Figure 7.8a. Here the injection into the channel is better defined, but unfortunately after current annealing, the device is not uniformly clean. In the Fabry-Pérot map G_{D1D2} (Figure 7.8b), the outer region exhibits a much stronger depletion of carrier densities (lower conductance) at the Dirac point, i. e. the lowest conductance is found at $V_{\text{out}} = 0$.

Compared to the discussed in Figures 7.3-7.5, the one shown here exhibits a slightly higher absolute guiding efficiency of 49% compared to 42% before (Figure 7.8c). This is due to the optimized injection into the channel. The relative increase from the unipolar value of 27% to 49% in the *p-n*-guiding regime is with 81% much higher than the 50% relative increase in the older sample. The device was destructed by further attempts of current annealing. On the other hand, the OF guiding is much weaker than for the device shown before. In addition, steps due to mode filling can not be clearly observed in this device. This is also due to a different geometry: In this case, the channel was formed by three bottomgate electrodes instead of one electrode and a global backgate. The designed channel width was with 600 nm much larger than before, which further complicates the observation of single mode-filling. We conclude that, even though the device was in the channel region not as clean as the device shown in Figure 7.2, the injection properties were improved due to the optimized design.

The measured guiding efficiency of a third device is shown in Figure 7.8d. For geometrical reasons, this device exhibits less crosstalk between the gates, i. e. the white dashed lines are less tilted in this case. Even though the overall guiding efficiency is slightly lower, OF guiding and steps in the conductance $G_{\text{SC}}(V_{\text{in}})$ are visible. The features appear to be similar to the mode filling steps described before, i. e. almost equally spaced plateaus and additional resonances. With dashed lines we indicate features that are probably due to mode filling, and with arrows we mark what might be the two-cavity resonances. The plateaus are however less constant with increasing V_{out}. In order to distinguish mode filling from coherent two-cavity resonances, detailed comparison to a modified theoretical model would be required.
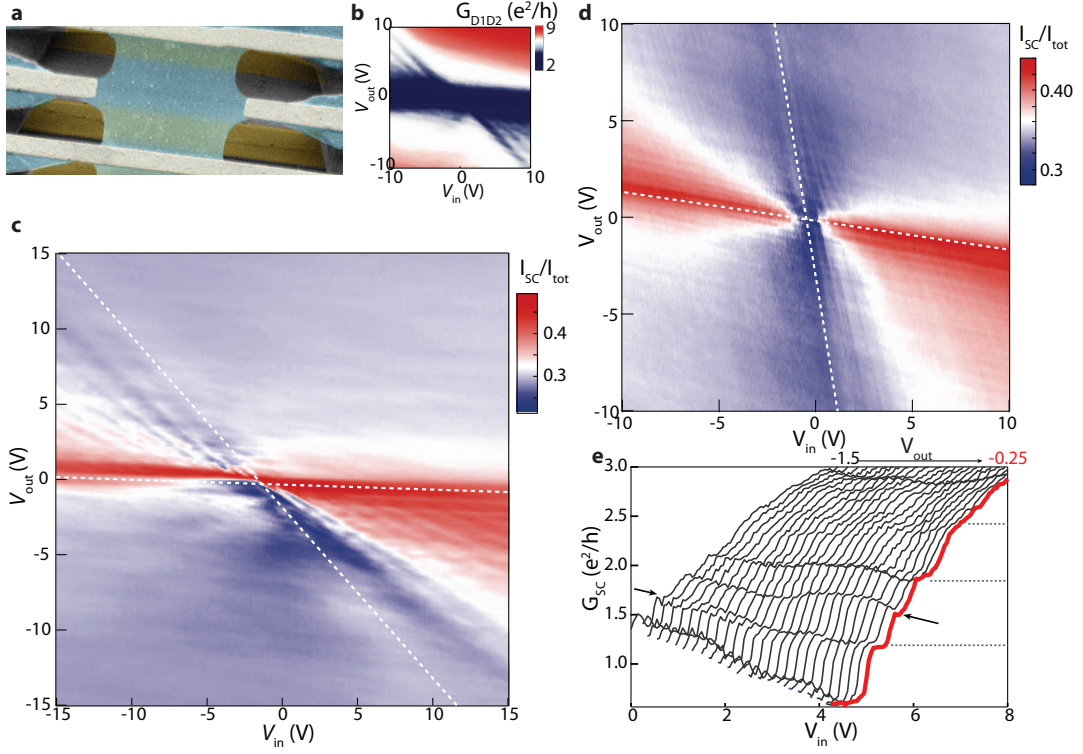
Figure 7.8.: **New measurement of electron guiding.** **a**, Scanning electron micrograph of an etched guiding device. **b** The Fabry-Pérot map $G_{D1D2}(V_{in}, V_{out})$ shows a low conductance in the outer region of the device. **c** Map of guiding efficiency I_{SC}/I_{tot}. The non-guiding value in the unipolar regime is around 27%, in the optical-fibre-guiding regime (e.g. at $V_{in} = 15V$ and $V_{out} = 2V$) the efficiency climbs to 32% and in the pn regime ($V_{in} = 15V$ and $V_{out} = -2V$) it increases by 22% to 49%. **d**, Guiding efficiency map of a third device with less crosstalk between the gates. The guiding efficiency is comparable to the former devices. OF guiding is clearly visible in this case. **e**, Steps as a function channel density appear in the conductance $G_{SC}(V_{in})$.

7.7. Conclusion

In conclusion, we have realized electrostatically defined electron waveguides in ballistic graphene with an aspect ratio >10 using a global and a channel gate. Typical channel parameters are $\approx 300\,\mathrm{nm}$ in width and $2.7\,\mu\mathrm{m}$ in length. The wavelengths of the charge carriers in- and outside of the channel can be tuned by the gates independently. Using this tunability, we can distinguish and control the regions of optical fiber- and *p-n* guiding. We observe an increased guiding efficiency if the two mechanisms coexist. Using *p-n* guiding, clear steps in the channel conductance appear whenever the mode number changes by one. All experimental results are supported by self-consistent theoretical simulations which also reveal that a smooth *p-n* interface and a sufficiently large momentum k_{x} along the channel is required to transport single modes. The simulation provides also a powerful guide for future device improvements. It shows, for example, that by using an even smoother *p-n* interface to confine the electrons in the channel, modes could be guided for $k_{\mathrm{x}} \ll k_{\mathrm{y}}$. In current devices the coupling from the injector contact to the channel and similarly from the channel to the detector contact is far from ideal. The injector and collector efficiencies of currently $\approx 35\%$ can be increased either by using a *p-n* interface as a collimator or by etching the graphene flake. With such improvements guiding efficiencies $> 80\%$, as demonstrated by the theory, are in reach. This then allows to explore one-dimensional transport in graphene without the need to etch nanoribbons. The difficulty of the required precise control over the sample edges at the atomic level in nanoribbons can then be circumvented. An electrostatically confined one-dimensional channel within the bulk of graphene could even be oriented intentionally into any preferred crystallographic direction allowing to study the symmetry of the one-dimensional bands. A high degree of confinement can further be used for fast switches with a potential visibility in excess of 80%.

8

Gate tuneable beamsplitter

Semi-transparent mirrors are an important building block of interference experiments. Graphene offers the unique possibility to mimick such optical systems once transport is ballistic. Especially the gapless *p-n* interface is of interest for the realization of a semi-transparent mirror. In this chapter we report on the fabrication and measurement of a ballistic, partially transparent mirror in ungapped bilayer graphene. We show that the mirror is tuned by two bottomgates and that we have the possibility to move the mirror by up to $1\,\mu$m. In addition, we discuss further requirements for the realization of electron-optic graphene multi-path interfereometers.

Semi-transparent mirrors act as beam splitters in optical experiments.They are important building blocks for many interference experiments, be it in a Fabry-Pérot etalon or in a two-path setup as realized in the Mach-Zehnder experiment where the position of the mirrors is varied. In two-dimensional electron gases (2DEGs) it is a challenge to construct such mirrors for the charge carriers. One successful realization of a beam splitter is using quantum point contacts that partially transmit quantum Hall edge states. The Mach-Zehnder experiment could be reconstructed like this [20] involving however strong magnetic fields that alter the transport properties of the 2DEG.

Graphene offers the unique possibility to mimic such optical systems once transport is ballistic. By using *p-n* interfaces Fabry-Pérot interferometers have been demonstrated in single-layer [37, 66, 67], gapped bilayer [120], and trilayer graphene [121]. Moreover, the observation of electron guiding, snake states [123, 138] or ballistic supercurrents [109–111] highlighted the possibilities of ballistic graphene *p-n* junctions.

P-n interfaces formed in graphene can be reflective, transparent or semi-transparent depending on the angle of incidence of the charge carriers and the shape of the potential that forms the interface. For smooth *p-n* junctions trajectories close to zero incidence angle are transmitted as a result of Klein tunneling, and electrons arriving under large incidence are reflected. This suggests that by using a tilted *p-n* interface, where the Klein-tunneling trajectories are not dominating, a partially transparent mirror can be achieved. In fact, measurements on short and tilted *p-n* interfaces
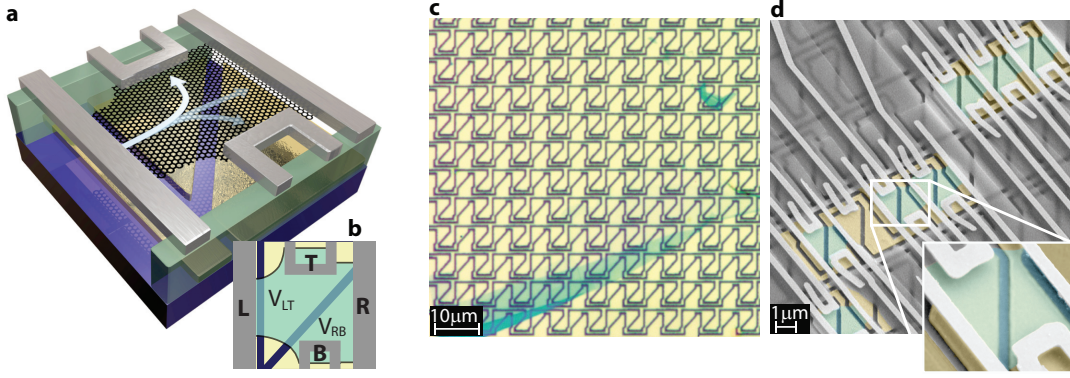
Figure 8.1.: **a-b**, Three-dimensional design and schematic representation of the mirror device. The Pd-contacts are gray, the bottomgates golden and the LOR pillars are colored green. The tilted bottomgate structure allows to form an oblique *p-n* interface. Electrons injected at the L contact will be either reflected towards T or transmitted towards the R or B contact. The efficiency of the mirror can be calculated by the measured currents at B, R and T. **c**, Optical image of an area covered with bottomgate structures. The turquoise parts are few-layer graphene on top of LOR. **d**, Scanning electron micrograph with a zoom-in window. Graphene is colored turquoise here, and the LOR resist is gray and semi-transparent.

on SiO$_2$ revealed an increase in two-terminal resistance by the use of a tilted interface [165, 166].

In this Chapter we present the measurement of a semi-transparent mirror, using a bottomgate structure tilted with respect to the current flow direction. The presented four-terminal device allows to measure reflectance and transmission of the mirror in a ballistic, ungapped bilayer sample. We show, that in the unipolar regime, the measured currents can be understood within a simple geometrical picture, whereas in the bipolar junction a partially reflective mirror is formed. We demonstrate that the transport in weak magnetic fields can be substantially altered upon moving the position of the mirror by up to 1 μm.

8.1. Design and Device preparation

In order to measure the reflectance of a bilayer *p-n* interface we designed a four-terminal sample as shown schematically in Figure 8.1a. Bilayer graphene is expected to give a more reflective interface [36,39]. For the use as a beam splitter it is important however to operate with gapless bilayer. On one hand we measured at high enough temperature (1.5 K) such that the spontaneous gap does not lead to zero conductance [49, 167], on the other hand the electric field present in our sample is far too low to

observe the induced gap [96,168]. The contacts and gates are labeled in the schematic top-view of Figure 8.1b. Using the two bottomgates V_{LT} and V_{RB} a tilted *p-n* interface can be formed and the reflectance of the mirror can be tuned. It is measured by injecting current at the left (L) contact and recording the reflected signal at the top (T) and the transmitted at the right (R) and bottom (B) contact by standard Lock-In technique.

We fabricate [65,87] such samples by patterning large areas with a tilted bottomgate structure on top of an undoped Si substrate. After spin-coating lift-off resist (LOR), graphene is transferred on top of the gate array (see Chapter 4). Due to the large patterned area, no special care needs to be taken during alignment. In Figure 8.1c an optical image of such a bottomgate array after LOR and graphene deposition is shown. The bottomgate array is tuned by three voltages, allowing to influence two interfaces for each device independently - a non-tilted interface close to the L contact and the tilted mirror interface. However, since the first interface is very close to the L contact for the measured sample, we did not see a change in the transport characteristics using this gate. For simplicity we therefore connect this gate to the first tilted gate and refer to it as V_{LT} in the following. The turquoise parts in the Figure 8.1c are few-layer graphene flakes (> 3 layers). Thinner flakes are not or only barley visible in the optical microscope after transfer, but their position is known from images recorded before. A scanning-electron micrograph after suspension is given in Figure 8.1d.

The design presented here offers few advantages. The U-shaped side contacts (T and B) are mechanically stable, i.e. they can be suspended over at least $3\,\mu$m using $80\,$nm of Pd. Since 70% of the perimeter of the etched graphene is attached to contacts and the longest suspended part is $< 1.5\,\mu$m this device is stabilized during current annealing and the risk of tearing the graphene is drastically reduced. And finally, the large distance between bottomgate and graphene allows to tune the position of the mirror by $1\,\mu$m as we will reveal later.

8.2. Reflectance of the mirror

For characterization after current annealing we measure the conductance across the device, i.e. from L to R (G_{LR}) and from T to B (G_{TB}), as a function of unipolar gate tuning, i.e. $V_{LT} = V_{RB}$. These field effect measurements are shown in Figure 8.2a to reveal the residual doping n_0 after current annealing. The field effect traces flatten in the range of $n_0 \approx 1...2 \cdot 10^9\,$cm^{-2} for the electron (turquoise) and hole (blue dashed) doping in both directions across the device, proving the high quality of the measured device.

We now discuss the reflectance of the mirror. In Figure 8.2b the conductance $G_{LT}(V_{LT}, V_{RB})$ is given. Apparently, upon the formation of a *p-n* interface, the current reaching the top contact is increased (red pn and np region) compared to the unipolar pp or nn situation (blue). For the transmitted charge carriers reaching the R and
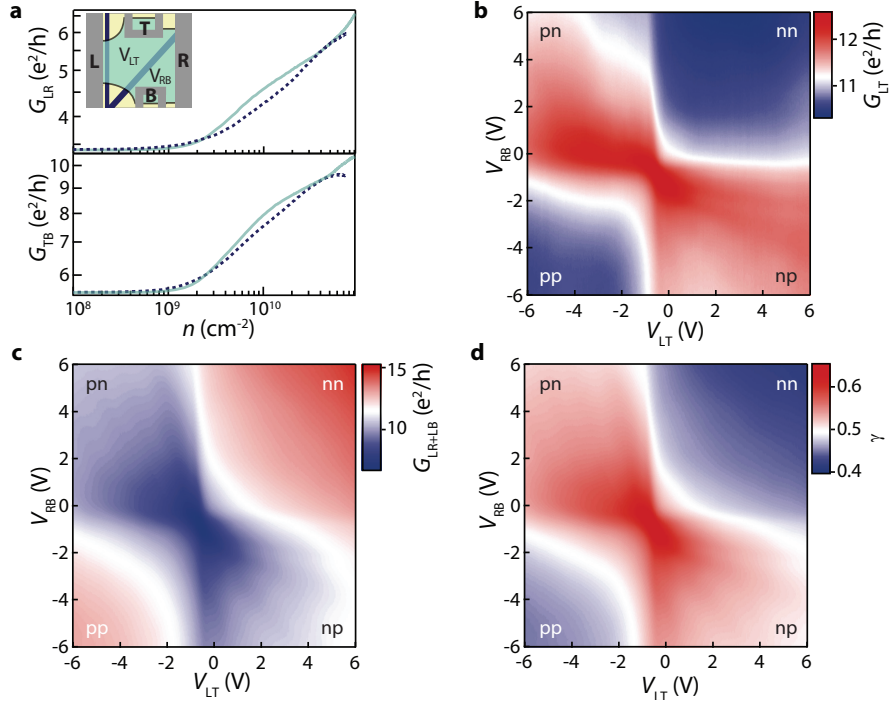
Figure 8.2.: **a**, The conductances G_{LR} and G_{BT} across the device as a function of unipolar gating ($V_{\text{LT}} = V_{\text{RB}}$) in a log-log plot reveal residual doping of $n_0 \approx 1...2 \cdot 10^9 \, \text{cm}^{-2}$ for the electron (turquoise) and hole-side (dashed). **b**, G_{LT} measured between L and T contact, as a function of the mirror gates V_{LT} and V_{RB} showing an increased conductance in the bipolar regime. **c**, In contrast, the conductance from the L to the R and B contact is higher in the unipolar regime. **d**, The reflectance of the mirror $\gamma = I_{\text{LT}}/I_{\text{tot}}$ is increased from 40% in the unipolar to above 60% in the bipolar regime.

B contact ($G_{\text{LR+LB}}(V_{\text{LT}}, V_{\text{RB}})$) the opposite is observed: The conductance is lowered when the *p-n* interface is present compared to the unipolar case (Figure 8.2c). Finally, the reflectance of the mirror is given by $\gamma = I_{\text{LT}}/I_{\text{tot}}$ with $I_{\text{tot}} = I_{\text{LT}} + I_{\text{LR}} + I_{\text{LB}}$ which is plotted in Figure 8.2d. For uniform (nn or pp) gating roughly $\gamma_0 := \gamma(6\,\text{V}, 6\,\text{V}) = 40\%$ of the current reaches the T contact. Upon the formation of a *p-n* interface, γ increases to 60%.

We further investigate the reflection properties of the pn interface by recording the reflected conductances for different injector contacts. The reflectance in different measurement configurations (explained in Fig. 8.3b) is shown in Figure 8.3a, where curves of $\gamma(V_{\text{LT}}, V_{\text{RB}} = 6\,V)$ are plotted. The blue curve corresponds to a cut in the colorscale plot of Figure 8.2d. For the blue dashed curve, current is injected at the T contact and γ is given by $I_{\text{TL}}/(I_{\text{TL}} + I_{\text{TB}} + I_{\text{TR}})$. In a corresponding way the (dashed) turquoise line corresponds to injection at the R (B) contact. As before,

86

γ_0 is the reference reflectance, without having an interface present. The obtained reflectances are roughly consistent with a simple geometric consideration, sketched in the schematics of Figure 8.3b. Ballistic charge carriers, injected from the middle of the L contact, reach the T contact under a solid angle of α and the R and B contacts under β. The ratio $\gamma'_{0,LT} = \alpha/(\alpha + \beta) = 0.35$ is roughly consistent with the measured $\gamma_{0,LT} = 0.41$. This holds also for the ratio of current reaching the R or B contact, i.e. $\gamma'_{0,LR} = 0.34$ and $\gamma_{0,LR} = 0.26$ and similarly $\gamma'_{0,LB} = 0.31$ and $\gamma_{0,LB} = 0.33$. Furthermore, the ratios for different measuring configurations are $\gamma'_{0,TL} = 0.31$ and $\gamma_{0,TL} = 0.33$, $\gamma'_{0,RB} = 0.41$ and $\gamma_{0,RB} = 0.48$, $\gamma'_{0,BR} = 0.41$ and $\gamma_{0,BR} = 0.47$. Deviations are due to the strong simplification of the model, contact doping and varying contact resistance.
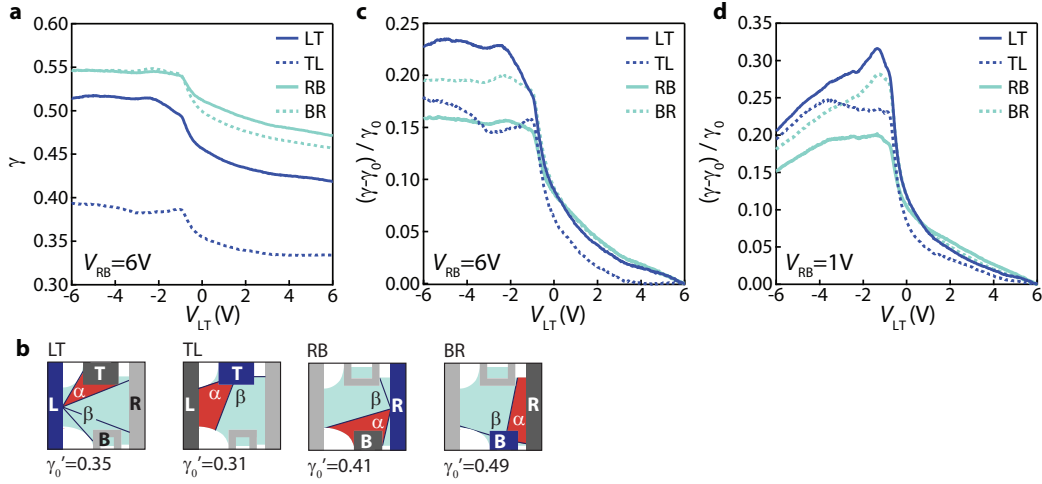

Figure 8.3.: **a**, $\gamma(V_{LT})$ at $V_{RB} = 6\,V$ for different device configurations. The dark blue curve for instance corresponds to a cut in the γ_{LT} colorscale plot of Figure 8.2d. **b**, Different measurement configurations. The injector contact is colored blue. **c**, Absolute increase of reflectance $(\gamma - \gamma_0)/\gamma_0$, where $\gamma_0 = \gamma((6,6)\,V)$ is a geometrical factor. **d**, Similar plot for $V_{RB} = 1\,V$.

In Figure 8.3c, the relative increase of reflectance $(\gamma - \gamma_0)/\gamma_0$ for $V_{RB} = 6\,V$ is shown. The highest value is reached by injecting at the L contact. The device is designed for this configuration since direct trajectories from L to T or B are minimized compared to the other configurations. The highest values of reflectance can be found close to the CNP as can be seen in Fig. 8.2b and in Fig. 8.3d, which shows the relative increase of the reflectance for $V_{RB} = 1\,V$. This is the result of short-cut currents flowing at the edges, which become prominent at low densities. First, the electric field at the sample edge is larger, leading to higher doping at the edges, since the bottomgate structure extends much further than the flake. Second, residual dopants tend to accumulate close to the contacts after current annealing [169], also leading to currents that remain unaffected by the formation of a *p-n* interface. And third, the doping of the contacts

becomes more significant. These effects lead to larger relative currents at the edges compared to the bulk, mostly pronounced at low densities. The effect of these edge currents are prominent for currents flowing from L to T and L to T, whereas it is reduced for currents from L to R, which results in the increase seen in Figure 8.3d.

Even if these currents could be drastically reduced, an efficiency of 100% cannot be achieved in our device, since electrons under a wide range of angles reach the (bilayer) *p-n* interface. This is the result of extended contact size, and a lack of collimation. Out of the trajectories reaching the interface, some always have finite transmission [36], i. e. trajectories with small, but non-zero incidence. At zero incidence the transmission is zero (anti-Klein tunneling), under larger angles, however, transmission becomes finite, but the smoothness of the junction leads to an exponential suppression [38].

8.3. Bent trajectories in magnetic field

By applying a perpendicular magnetic field B, the amount of electrons reaching the T contact (injected from L) can be increased using magnetic focussing. This is seen in Figure 8.4a and b, where we show the conductance increase with respect to zero field measurement, i.e. $G_{LT}(50\,\mathrm{mT}) - G_{LT}(0\,\mathrm{T})$ and $G_{LT}(100\,\mathrm{mT}) - G_{LT}(0\,\mathrm{T})$ respectively.

The structure of the maps are explained using the sketches in Figure 8.4c. In the case of unipolar nn doping, G_{LT} rises by $\approx 1\,e^2/h$ since the electrons are deflected towards the T contact due to the Lorentz force (1). The cyclotron diameter is with $1.4\,\mu\mathrm{m}$ at $V_{LT} = V_{RB} = 6\,\mathrm{V}$ in the range of the geometrical dimensions (the distance between L and T is $1.1\,\mu\mathrm{m}$), implying that we are in situation of magnetic focusing [9, 46]. A clear focusing signal is however not expected due to the large size of the contacts. The increase is most pronounced at small gate voltages, where the cyclotron radius is smallest. The additional current at the T contact is not influenced if an *n-p* interface is formed by lowering V_{RB}, as sketched in Figure 8.4c (2). For this reason, the conductance increases by the same amount in regions (1) and (2), as seen in the grayscale 8.4a. However, if V_{LT} is decreased, the cyclotron motion changes sign once the polarity of charge carriers is inverted (3). In this pp region, the holes are deflected towards the B contact, leading to a decreased conductance measured at T. This decrease persists in the *p-n* region (4) for large $|V_{LT}|$ and low $|V_{RB}|$. But surprisingly, the conductance is enhanced in the opposite case (5), i.e. low $|V_{LT}|$ and large $|V_{RB}|$.

The structure in the *p-n* region can be understood by considering two effects. First, once a *p-n* interface is present, current flows along this interface. In the case of single layer graphene, charge carriers are guided along snaking trajectories [123, 138] as described in Chapter 6. Despite the absence of Klein tunneling also in (ungapped) bilayer graphene, a current along the *p-n* interface builds up. The second effect takes into account the large graphene to bottomgate distance (600 nm) that allows to change the position Δ_{pn} of the *p-n* interface drastically by the gates. In Figure 8.4d, the position of the *p-n* interface for symmetric gating is drawn as a black
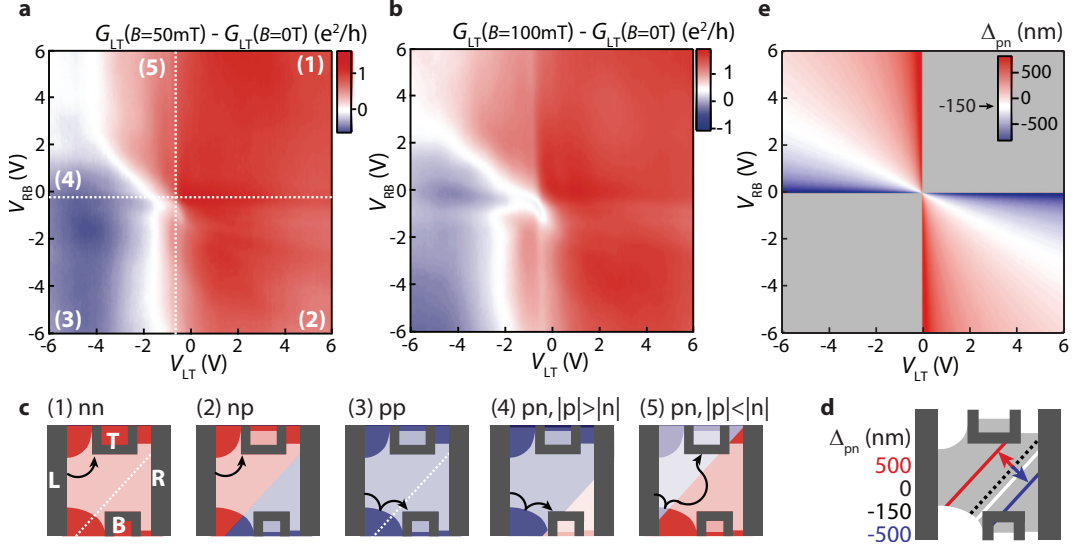
Figure 8.4.: **a**, Increase of the mirrored signal in magnetic field of $50\,\mathrm{mT}$: $G_{\mathrm{LT}}(B = 50mT)$ - $G_{\mathrm{LT}}(B = 0T)$. The plot shows a strong asymmetry as a function of V_{LT}. This asymmetry is due to the enhanced ($V_{LT} > 0$) or reduced ($V_{\mathrm{LT}} < 0$) conductance measured at the T contact as a result of bent trajectories in B field. The upper left quadrant is split into an enhanced and a reduced part along a diagonal line. **b**, Similar plot showing the difference of G_{LT} at $100\,mT$ an $0\,T$. **c**, The sketches explain the observed pattern. In region (1), current is bent towards T leading to an enhanced conductance G_{LT}. This enhancement remains unchanged upon the formation of an *n-p* interface for the same polarity in the LT region (2). However if this polarity is inverted (3), trajectories bend towards B reducing the current at T. As long as the interface is close to B (4) nothing changes, however by increasing $V_{\mathrm{LT}}/V_{\mathrm{RB}}$ the conductance at T is enhanced since current can flow along the interface (5). **d**, Geometry of the device showing the relative position of the *p-n* interface for different Δ_{pn} values. **e**, Colorscale map from electrostatic simulations, revealing that Δ_{pn} depends on the ratio of $V_{\mathrm{LT}}/V_{\mathrm{RB}}$. Our device offers a high tuning range ($\pm500\,nm$) due to the large distance between bottomgate and graphene.

dashed line. By lowering the density in the LT cavity (i.e. by lowering $|V_{\mathrm{LT}}|$) the interface can be shifted up to $500\,\mathrm{nm}$ towards the T contact (red line). On the other hand, by decreasing $|V_{\mathrm{RB}}|$, the interface is shifted towards the B contact by a similar amount (blue line). A colorscale map revealing $\Delta_{\mathrm{pn}}(V_{\mathrm{LT}}, V_{\mathrm{RB}})$ is given in Figure 8.4e. The white region marks the transition between (4) and (5) in Figures 8.4a,b and corresponds to $\Delta_{\mathrm{pn}} = -150\,\mathrm{nm}$. The corresponding position of the *p-n* interface is sketched as a white dashed line in Figure 8.4d, showing that for the corresponding gating ratio $|V_{\mathrm{RB}}|/|V_{\mathrm{LT}}|$ the interface crosses the B contact. For larger $|V_{\mathrm{RB}}|/|V_{\mathrm{LT}}|$, the *p-n* interface is negligible for the injected current in L, as sketched in Figure 8.4c (4), explaining the similarity to region (3). However, the interface transports charge carriers in direction of the T contact in the opposite case (5), leading to an increased G_{LT} at $50\,\mathrm{mT}$ and $100\,\mathrm{mT}$.

8.4. Discussion and Conclusion

The herein discussed device presents the realization of a semi-transparent graphene mirror with movable position. This device can be the fundamental building block of a Michelson-Morley or a Mach-Zehnder interferometer.
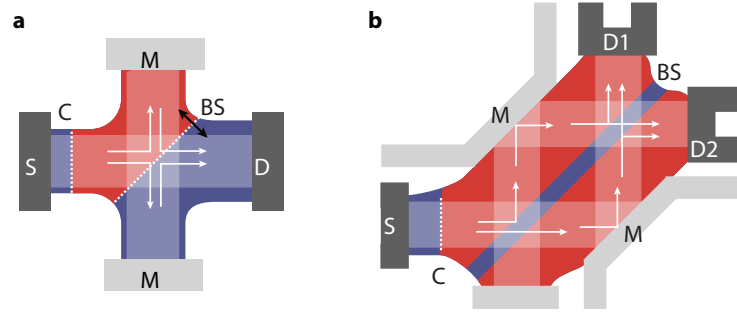

Figure 8.5.: **a**, In a Michelson-Morley interferometer, light is emitted from a source (S) and collimated (C) before reaching a beam splitter (BS). The two resulting paths are reflected from the mirrors (M) and an interference pattern will be measured at the detectors at D_1 and D_2. The realization in graphene uses a *p-n* interface as a collimator and a second *p-n* interface as beam-splitter. **c**, The Mach-Zehnder requires tilted mirrors and two beam splitters. Here we use a *p-n-p* interface as beam-splitter. The mirrors (M) can be either the edge of graphene or contacts.

We present a possible realization of a Michelson-Morley interferometer in single layer graphene in Figure 8.5a, where the source is denoted by S, the collimator by C, the beam splitter by BS, the mirrors by M and the detectors by D1. Note that, due to the negative refraction, the position of D and M are exchanged compared to the optical experiment. The most important modification to the here presented

beamsplitter is the collimator interface. The strong collimation offered by smooth *p-n* interfaces [38] can be harvested to create a plane-wave in graphene (denoted as C in Figure 8.5b). The second, tilted *p-n* interface in Fig. 8.5 acts as a beam splitter and can be tuned by the gates ideally such that 50% transmission is achieved.

The reflective mirrors (M) of the optical system can be replaced either by edges of the graphene flake, (reflective) contacts or additional *p-n* interfaces. The reflection at the graphene edges is mostly specular rather than diffusive, as it has been demonstrated by magnetic focusing experiments [46, 47]. The acquired phase in the left (right) cavity can be changed by the density in the left (right) cavity. As shown before, suspended samples allow to change the position of the *p-n* interface drastically. Therefore the interference can be tuned both by changing the wavelength and the path-length (not independently), leading to a distinct interference patterns in the $G_{SD}(V_{G1}, V_{G2})$) map.

Alternatively a Mach-Zehnder-like experiment could be realized in graphene as sketched in Figure 8.5b. This design would be more suited for hBN encapsulated devices, where sharp *p-n* interfaces can be formed. Here, the beam splitter would be based on a *p-n-p* junction, which can be tuned with the gate voltages to 50% transmission. The mirrors can be fabricated similarly to the Michelson-Morley interferometer and an interference pattern will be observed at D_1 and D_2 depending on the phase acquired along the path.

The ideas shown above demonstrate, that the herein presented device is the first building block of multi-pass interferometers in graphene.

9 Conclusion

The vast possibilities graphene offers as a platform for electron optics has been the subject of this thesis. One of the basic requirements allowing to perform electron optics experiments, is ballistic transport. For this reason, we compared several characterization methods in Chapter 3 which allow to demonstrate that the devices fabricated and measured in the scope of this thesis are among the cleanest reported so far.

This achievement has been made possible by adapting a fabrication technique proposed in Reference [65] and discussed in Chapter 4 and Reference [87]. High quality is achieved by in-situ current annealing of suspended graphene, passing currents of $\approx 350\,\mu\text{A}/\mu\text{m}$. A key improvement, allowing to achieve ballistic transport in μm-sized devices, lies in the removal of the LOR resist below the palladium contacts. We further demonstrated a modification of the fabrication process to implement local gates. This has been achieved by depositing graphene with a dry-transfer technique. The versatility of the method was demonstrated by creating complex multi-terminal devices, the inclusion of superconducting contacts and the use of CVD graphene.

In Chapter 5 and Reference [67], we reported on the creation of a μm-sized Fabry-Pérot interferometer. Constructive or destructive interference in the electrostatically defined *p-n* cavities was obtained by changing local gate voltages. We observed that the strong collimation effect provided by our extremely smooth *p-n* interfaces is responsible for the visibility of the interference pattern. This aspect is stressed by tight-binding transport simulations which showed an excellent agreement to the measured data, with which we could claim the absence of any disorder pattern causing density fluctuations (in the order of $10^9\,\text{cm}^{-2}$). In addition to the data presented in Reference [67], we analyzed the interference pattern of a *p-n-p* device in this thesis and showed that visibility can be gained by using two smooth interfaces. The experimentally observed visibility reaches values of 20%, similar to values predicted by analytical considerations. To our knowledge, this is probably the best interferometer achievable in graphene using parallel *p-n* interfaces, since Klein tunneling leads to a large background conductance. We proposed to harvest this Klein-tunneling background conductance for the creation of plane waves, or, in optical terms, to use the *p-n* interface as a collimator.

The transparency of the *p-n* interface is of importance for the formation of snake

states as we revealed in Chapter 6 and Reference [123]. At small (20 mT) perpendicular magentic fields, charge carriers form trajectories that bend towards a *p-n* interface, (Klein-)tunnel to the other side where they are deflected again towards the interface. Such snake-state trajectories can be described in the quasi-classical skipping orbit picture, requiring, however, cleanest possible devices. We reported on magneto-conductance oscillations that we could trace back to snake states by using tight-binding calculations. The similarity to electron-hole states at graphene-superconductor interfaces is a surprising connection to our former work [137]. Making the connection to electron optics, we stated that the magnetic field acts as a lens which focuses electrons to the left or right side of the *p-n* interface and thereby leads to the observed magneto-conductance oscillations. The *p-n* junction on the other hand acts as an angular filter in the same experiment. This combination presents a unique tool for controlled focusing and guiding experiments.

As an alternative approach to guide charge carriers in a controlled way, we presented an electrostatic few-mode channel in Chapter 7. We demonstrated that we could transport ballistic charge carriers by adjusting the refractive index inside and outside the channel as for an optical fiber. When trying to guide single modes, however, we were facing a difficulty that engineers of optical fibers had to overcome as well. First, particles need to be injected under flat angles and, second, the loss in the channel needs to be decreased by increasing the angle of total internal reflection. Whereas the injection remains a problem, we could make use of the strong collimation provided by a smooth *p-n* interface allowing to guide much steeper angles in the channel. By a careful comparison with tight-binding simulations we could demonstrate the successful transport of single modes in a $2.2\,\mu$m long channel.

Finally, we added another piece to the electron-optics toolbox by demonstrating in Chapter 8 that a *p-n* interface can be used as a mirror. By analyzing magentic field data, we showed that the position of the mirror can be adjusted by $1\,\mu$m or 1/3 of the sample size. Such mirrors could be used for complex interference experiments as represented by the Michelson-Morley setup. We stressed that the presented device requires only slight modification bringing a graphene Michelson-Morley experiment to the close future. Such an experiment would demonstrate a new level of control over graphene's quasi-relativistic particles, making it possible to harvest its advantages for ultrafast electronics and quantum computation.

Bibliography

[1] O. Klemperer, M. Barnett, *Electron Optics*, Cambridge University Press (1971).

[2] H. Busch, *Berechnung der Bahn von Kathodenstrahlen im axialsymmetrischen elektromagnetischen Felde*, Annalen der Physik Leipzig **81**, 974 (1926).

[3] M. Ardenne, *Das Elektronen-Rastermikroskop. Theoretische Grundlagen*, Zeitschrift für Physik **109**, 553 (1938).

[4] H. van Houten, C. Beenakker, *Analogies in Optics and Micro Electronics*, Springer Netherlands (1990).

[5] Y. Sharvin, *A possible Method for studying Fermi Surfaces*, JETP Letters **48**, 984 (1965).

[6] V. Tsoi, *Focusing of electrons in a metal by a transverse magnetic field*, JETP Letters **19**, 70 (1974).

[7] B. J. van Wees, H. van Houten, C. W. J. Beenakker, J. G. Williamson, L. P. Kouwenhoven, D. van der Marel, C. T. Foxon, *Quantized conductance of point contacts in a two-dimensional electron gas*, Physical Review Letters **60**, 848 (1988).

[8] D. A. Wharam, T. J. Thornton, R. Newbury, M. Pepper, H. Ahmed, J. E. F. Frost, D. G. Hasko, D. C. Peacock, D. A. Ritchie, G. A. C. Jones, *One-dimensional transport and the quantisation of the ballistic resistance*, Journal of Physics C: Solid State Physics **21**, L209 (1988).

[9] H. van Houten, B. J. van Wees, J. E. Mooij, C. W. J. Beenakker, J. G. Williamson, C. T. Foxon, *Coherent Electron Focussing in a Two-Dimensional Electron Gas*, Europhysics Letters **5**, 721 (1988).

[10] H. van Houten, C. W. J. Beenakker, J. G. Williamson, M. E. I. Broekaart, P. H. M. van Loosdrecht, *Coherent electron focusing with quantum point contacts in a two-dimensional electron gas*, Physical Review B **39**, 8556 (1989).

[11] K. S. Novoselov, *Two-dimensional gas of massless Dirac fermions in graphene*, Nature **438**, 197 (2005).

[12] V. V. Cheianov, V. Falko, B. L. Altshuler, *The focusing of electron flow and a Veselago lens in graphene p-n junctions*, Science **315**, 1252 (2007).

[13] F.-M. Zhang, Y. He, X. Chen, *Guided modes in graphene waveguides*, Applied Physics Letters **94**, 212105 (2009).

[14] C. Beenakker, H. van Houten, B. van Wees, *Skipping orbits, traversing trajectories, and quantum ballistic transport in microstructures*, Superlattices and Microstructures **5**, 127 (1989).

[15] K. Nakamura, D. C. Tsui, F. Nihey, H. Toyoshima, T. Itoh, *Electron focusing with multiparallel one-dimensional channels made by focused ion beam*, Applied Physics Letters **56**, 385 (1990).

[16] A. Yacoby, U. Sivan, C. P. Umbach, J. M. Hong, *Interference and dephasing by electron-electron interaction on length scales shorter than the elastic mean free path*, Physical Review Letters **66**, 1938 (1991).

[17] A. Yacoby, M. Heiblum, V. Umansky, H. Shtrikman, D. Mahalu, *Unexpected Periodicity in an Electronic Double Slit Interference Experiment*, Physical Review Letters **73**, 3149 (1994).

[18] A. Yacoby, M. Heiblum, D. Mahalu, H. Shtrikman, *Coherence and Phase Sensitive Measurements in a Quantum Dot*, Physical Review Letters **74**, 4047 (1995).

[19] R. Schuster, E. Buks, M. Heiblum, D. Mahalu, V. Umansky, H. Shtrikman, *Phase measurement in a quantum dot via a double-slit interference experiment*, Nature **385**, 417 (1997).

[20] Y. Ji, Y. Chung, D. Sprinzak, M. Heiblum, D. Mahalu, H. Shtrikman, *An electronic Mach-Zehnder interferometer*, Nature **422**, 415 (2003).

[21] A. T. Johnson, L. P. Kouwenhoven, W. de Jong, N. C. van der Vaart, C. J. P. M. Harmans, C. T. Foxon, *Zero-dimensional states and single electron charging in quantum dots*, Physical Review Letters **69**, 1592 (1992).

[22] N. Peres, *Colloquium: The transport properties of graphene: An introduction*, Reviews of Modern Physics **82**, 2673 (2010).

[23] T. T. Heikkilä, *The Physics of Nanoelectronics*, Oxford University Press (2013).

[24] A. Young, Y. Zhang, P. Kim, *Physics of Graphene*, Springer International Publishing (2014).

[25] A. H. Castro Neto, F. Guinea, N. M. R. Peres, K. S. Novoselov, A. K. Geim, *The electronic properties of graphene*, Reviews of Modern Physics **81**, 109 (2009).

[26] E. Hall, *On a New Action of the Magnet on Electric Currents*, American Journal of Mathematics **2**, 287 (1879).

[27] K. v. Klitzing, G. Dorda, M. Pepper, *New Method for High-Accuracy Determination of the Fine-Structure Constant Based on Quantized Hall Resistance*, Physical Review Letters **45**, 494 (1980).

[28] K. S. Novoselov, Z. Jiang, Y. Zhang, S. V. Morozov, H. L. Stormer, U. Zeitler, J. C. Maan, G. S. Boebinger, P. Kim, A. K. Geim, *Room-Temperature Quantum Hall Effect in Graphene*, Science **315**, 1379 (2007).

[29] D. A. Abanin, L. S. Levitov, *Conformal invariance and shape-dependent conductance of graphene samples*, Physical Review B **78**, 035416 (2008).

[30] J. R. Williams, D. A. Abanin, L. DiCarlo, L. S. Levitov, C. M. Marcus, *Quantum Hall conductance of two-terminal graphene devices*, Physical Review B **80**, 045408 (2009).

[31] E. H. Hwang, S. Adam, S. D. Sarma, *Carrier Transport in Two-Dimensional Graphene Layers*, Physical Review Letters **98**, 186806 (2007).

[32] O. Klein, *Die Reflexion von Elektronen an einem Potentialsprung nach der relativistischen Dynamik von Dirac*, Zeitschrift für Physik A Hadrons and Nuclei **53**, 157 (1929).

[33] C. Anderson, *The Positive Electron*, Physical Review **43**, 491 (1933).

[34] F. Sauter, *Zum "Kleinschen Paradoxon"*, Zeitschrift für Physik **73,7–8**, 547 (1932).

[35] I. Meric, M. Y. Han, A. F. Young, B. Özyilmaz, P. Kim, K. L. Shepard, *Current saturation in zero-bandgap, top-gated graphene field-effect transistors*, Nature Nanotechnology **3**, 654 (2008).

[36] M. I. Katsnelson, K. S. Novoselov, A. K. Geim, *Chiral tunnelling and the Klein paradox in graphene*, Nature Physics **2**, 620 (2006).

[37] A. F. Young, P. Kim, *Quantum interference and Klein tunnelling in graphene heterojunctions*, Nature Physics **5**, 222 (2009).

[38] V. V. Cheianov, V. I. Falko, *Selective transmission of Dirac electrons and ballistic magnetoresistance of n-p junctions in graphene*, Physical Review B **74**, 041403 (R) (2006).

[39] M.-H. Liu, J. Bundesmann, K. Richter, *Spin-dependent Klein tunneling in graphene: Role of Rashba spin-orbit coupling*, Physical Review B **85**, 085406 (2012).

[40] Q. Wilmart, S. Berrada, D. Torrin, V. H. Nguyen, G. Fève, J.-M. Berroir, P. Dollfus, B. Plaçais, *A Klein-tunneling transistor with ballistic graphene*, 2D Materials **1**, 011006 (2014).

[41] S. Dröscher, P. Roulleau, F. Molitor, P. Studerus, C. Stampfer, K. Ensslin, T. Ihn, *Quantum capacitance and density of states of graphene*, Applied Physics Letters **96**, 152104 (2010).

[42] M.-H. Liu, *Theory of carrier density in multigated doped graphene sheets with quantum correction*, Physical Review B **87**, 125427 (2013).

[43] P. A. Khomyakov, G. Giovannetti, P. C. Rusu, G. Brocks, J. van den Brink, P. J. Kelly, *First-principles study of the interaction and charge transfer between graphene and metals*, Physical Review B **79**, 195425 (2009).

[44] P. A. Khomyakov, A. A. Starikov, G. Brocks, P. J. Kelly, *Nonlinear screening of charges induced in graphene by metal contacts*, Physical Review B **82**, 115437 (2010).

[45] M.-H. Liu, P. Rickhaus, P. Makk, E. Tóvári, R. Maurand, F. Tkatschenko, M. Weiss, C. Schönenberger, K. Richter, *Scalable Tight-Binding Model for Graphene*, Physical Review Letters **114**, 036601 (2015).

[46] T. Taychatanapat, K. Watanabe, T. Taniguchi, P. Jarillo-Herrero, *Electrically tunable transverse magnetic focusing in graphene*, Nature Physics **9**, 225 (2013).

[47] V. E. Calado, S.-E. Zhu, S. Goswami, Q. Xu, K. Watanabe, T. Taniguchi, G. C. A. M. Janssen, L. M. K. Vandersypen, *Ballistic transport in graphene grown by chemical vapor deposition*, Applied Physics Letters **104**, 023103 (2014).

[48] L. A. Ponomarenko, R. V. Gorbachev, G. L. Yu, D. C. Elias, R. Jalil, A. A. Patel, A. Mishchenko, A. S. Mayorov, C. R. Woods, J. R. Wallbank, M. Mucha-Kruczynski, B. A. Piot, M. Potemski, I. V. Grigorieva, K. S. Novoselov, F. Guinea, V. I. Fal'ko, A. K. Geim, *Cloning of Dirac fermions in graphene superlattices*, Nature **497**, 594 (2013).

[49] F. Freitag, J. Trbovic, M. Weiss, C. Schönenberger, *Spontaneously Gapped Ground State in Suspended Bilayer Graphene*, Physical Review Letters **108**, 076602 (2012).

[50] W. Bao, J. Velasco, F. Zhang, L. Jing, B. Standley, D. Smirnov, M. Bockrath, A. H. MacDonald, C. N. Lau, *Evidence for a spontaneous gapped state in ultraclean bilayer graphene*, Proceedings of the National Academy of Sciences (2012).

[51] X. Du, I. Skachko, F. Duerr, A. Luican, E. Y. Andrei, *Fractional quantum Hall effect and insulating phase of Dirac electrons in graphene*, Nature **462**, 192 (2009).

[52] D.-K. Ki, V. I. Fal'ko, D. A. Abanin, A. F. Morpurgo, *Observation of Even Denominator Fractional Quantum Hall Effect in Suspended Bilayer Graphene*, Nano Letters **14**, 2135 (2014).

[53] M. Ishigami, J. H. Chen, W. G. Cullen, M. S. Fuhrer, E. D. Williams, *Atomic Structure of Graphene on SiO2*, Nano Letters **7**, 1643 (2007).

[54] C. R. Dean, Y. A. F., I. MeriI., C. Lee, L. Wang, S. Sorgenfrei., K. Watanabe., T. Taniguchi, P. Kim., K. L. Shepard, J. Hone, *Boron nitride substrates for high-quality graphene electronics*, Nature Nanotechnology **5**, 722 (2010).

[55] J.-H. Chen, C. Jang, S. Adam, M. S. Fuhrer, E. D. Williams, M. Ishigami, *Charged-impurity scattering in graphene*, Nature Physics **4**, 377 (2008).

[56] K. Nomura, A. H. MacDonald, *Quantum Hall Ferromagnetism in Graphene*, Physical Review Letters **96**, 256602 (2006).

[57] R. Decker, Y. Wang, V. W. Brar, W. Regan, H.-Z. Tsai, Q. Wu, W. Gannett, A. Zettl, M. F. Crommie, *Local Electronic Properties of Graphene on a BN Substrate via Scanning Tunneling Microscopy*, Nano Letters **11**, 2291 (2011).

[58] L. Wang, I. Meric, P. Y. Huang, Q. Gao, Y. Gao, H. Tran, T. Taniguchi, K. Watanabe, L. M. Campos, D. A. Muller, J. Guo, P. Kim, J. Hone, K. L. Shepard, C. R. Dean, *One-Dimensional Electrical Contact to a Two-Dimensional Material*, Science **342**, 614 (2013).

[59] J. Xue, J. Sanchez-Yamagishi, D. Bulmash, P. Jacquod, A. Deshpande, K. Watanabe, T. Taniguchi, P. Jarillo-Herrero, B. J. LeRoy, *Scanning tunnelling microscopy and spectroscopy of ultra-flat graphene on hexagonal boron nitride*, Nature Materials **10**, 282 (2011).

[60] G. L. Yu, R. Jalil, B. Belle, A. S. Mayorov, P. Blake, F. Schedin, S. V. Morozov, L. A. Ponomarenko, F. Chiappini, S. Wiedmann, U. Zeitler, M. I. Katsnelson, A. K. Geim, K. S. Novoselov, D. C. Elias, *Interaction phenomena in graphene seen through quantum capacitance*, Proceedings of the National Academy of Sciences (2013).

[61] S. Masubuchi, S. Morikawa, M. Onuki, K. Iguchi, K. Watanabe, T. Taniguchi, T. Machida, *Fabrication and Characterization of High-Mobility Graphene p–n–p Junctions Encapsulated by Hexagonal Boron Nitride*, Japanese Journal of Applied Physics **52**, 110105 (2013).

[62] S. Engels, A. Epping, C. Volk, S. Korte, B. Voigtländer, K. Watanabe, T. Taniguchi, S. Trellenkamp, C. Stampfer, *Etched graphene quantum dots on hexagonal boron nitride*, Applied Physics Letters **103**, 073113 (2013).

[63] K. Bolotin, K. Sikes, Z. Jiang, M. Klima, G. Fudenberg, J. Hone, P. Kim, H. Stormer, *Ultrahigh electron mobility in suspended graphene*, Solid State Communications **146**, 351 (2008).

[64] X. Du, I. Skachko, A. Barker, E. Y. Andrei, *Approaching ballistic transport in suspended graphene*, Nature Nanotechnology **3**, 491 (2008).

[65] N. Tombros, A. Veligura, J. Junesch, J. van den Berg, P. Zomer, I. Vera-Marun, H. Jonkman, B. van Wees, *Large yield production of high mobility freely suspended graphene electronic devices on a polydimethylglutarimide based organic polymer*, Journal of Applied Physics **109**, 093702 (2011).

[66] A. L. Grushina, D.-H. Ki, A. F. Morpurgo, *A ballistic pn junction in suspended graphene with split bottom gates*, Applied Physics Letters **102**, 223102 (2013).

[67] P. Rickhaus, R. Maurand, M.-H. Liu, M. Weiss, K. Richter, C. Schönenberger, *Ballistic interferences in suspended graphene.*, Nature Communications **4**, 2342 (2013).

[68] P. J. Zomer, S. P. Dash, N. Tombros, B. J. van Wees, *A transfer technique for high mobility graphene devices on commercially available hexagonal boron nitride*, Applied Physics Letters **99**, 232104 (2011).

[69] S. Engels, B. Terrés, A. Epping, T. Khodkov, K. Watanabe, T. Taniguchi, B. Beschoten, C. Stampfer, *Limitations to Carrier Mobility and Phase-Coherent Transport in Bilayer Graphene*, Physical Review Letters **113**, 126801 (2014).

[70] N. J. G. Couto, D. Costanzo, S. Engels, D.-K. Ki, K. Watanabe, T. Taniguchi, C. Stampfer, F. Guinea, A. F. Morpurgo, *Random Strain Fluctuations as Dominant Disorder Source for High-Quality On-Substrate Graphene Devices*, Physical Review X **4**, 041019 (2014).

[71] C. R. Woods, L. Britnell, A. Eckmann, R. S. Ma, J. C. Lu, H. M. Guo, X. Lin, G. L. Yu, Y. Cao, R. V. Gorbachev, A. V. Kretinin, J. Park, L. A. Ponomarenko, M. I. Katsnelson, Y. N. Gornostyrev, K. Watanabe, T. Taniguchi, C. Casiraghi, H.-J. Gao, A. K. Geim, K. S. Novoselov, *Commensurate-incommensurate transition in graphene on hexagonal boron nitride*, Nature Physics **10**, 451 (2014).

[72] M. Yankowitz, J. Xue, D. Cormode, J. D. Sanchez-Yamagishi, K. Watanabe, T. Taniguchi, P. Jarillo-Herrero, P. Jacquod, B. J. LeRoy, *Emergence of superlattice Dirac points in graphene on hexagonal boron nitride*, Nature Physics **8**, 382 (2012).

[73] C. R. Dean, L. Wang, P. Maher, C. Forsythe, F. Ghahari, Y. Gao, J. Katoch, M. Ishigami, P. Moon, M. Koshino, T. Taniguchi, K. Watanabe, K. L. Shepard, J. Hone, P. Kim, *Hofstadter/'s butterfly and the fractal quantum Hall effect in moire superlattices*, Nature **497**, 598 (2013).

[74] B. Hunt, J. D. Sanchez-Yamagishi, A. F. Young, M. Yankowitz, B. J. LeRoy, K. Watanabe, T. Taniguchi, P. Moon, M. Koshino, P. Jarillo-Herrero, R. C. Ashoori, *Massive Dirac Fermions and Hofstadter Butterfly in a van der Waals Heterostructure*, Science **340**, 1427 (2013).

[75] R. V. Gorbachev, J. C. W. Song, G. L. Yu, A. V. Kretinin, F. Withers, Y. Cao, A. Mishchenko, I. V. Grigorieva, K. S. Novoselov, L. S. Levitov, A. K. Geim, *Detecting topological currents in graphene superlattices*, Science **346**, 448 (2014).

[76] E. V. Castro, H. Ochoa, M. I. Katsnelson, R. V. Gorbachev, D. C. Elias, K. S. Novoselov, A. K. Geim, F. Guinea, *Limits on Charge Carrier Mobility in Suspended Graphene due to Flexural Phonons*, Physical Review Letters **105**, 266601 (2010).

[77] E. H. Hwang, S. Das Sarma, *Acoustic phonon scattering limited carrier mobility in two-dimensional extrinsic graphene*, Physical Review B **77**, 115449 (2008).

[78] M. Katsnelson, A. Geim, *Electron scattering on microscopic corrugations in graphene*, Philosophical Transactions of the Royal Society of London A: Mathematical, Physical and Engineering Sciences **366**, 195 (2008).

[79] J. Tworzydło, B. Trauzettel, M. Titov, A. Rycerz, C. W. J. Beenakker, *Sub-Poissonian Shot Noise in Graphene*, Physical Review Letters **96**, 246802 (2006).

[80] V. V. Cheianov, V. I. Fal'ko, B. L. Altshuler, I. L. Aleiner, *Random Resistor Network Model of Minimal Conductivity in Graphene*, Physical Review Letters **99**, 176801 (2007).

[81] S. Adam, E. H. Hwang, V. M. Galitski, S. Das Sarma, *A self-consistent theory for graphene transport*, Proceedings of the National Academy of Sciences of the United States of America **104**, 18392 (2007).

[82] A. S. Mayorov, R. V. Gorbachev, S. V. Morozov, L. Britnell, R. Jalil, L. A. Ponomarenko, P. Blake, K. S. Novoselov, K. Watanabe, T. Taniguchi, A. K. Geim, *Micrometer-Scale Ballistic Transport in Encapsulated Graphene at Room Temperature*, Nano Letters **11**, 2396 (2011).

[83] D. C. Elias, R. V. Gorbachev, A. S. Mayorov, S. V. Morozov, A. A. Zhukov, P. Blake, L. A. Ponomarenko, I. V. Grigorieva, K. S. Novoselov, F. Guinea, A. K. Geim, *Dirac cones reshaped by interaction effects in suspended graphene*, Nature Physics **7**, 701 (2011).

[84] A. S. Mayorov, D. C. Elias, I. S. Mukhin, S. V. Morozov, L. A. Ponomarenko, K. S. Novoselov, A. K. Geim, R. V. Gorbachev, *How Close Can One Approach the Dirac Point in Graphene Experimentally?*, Nano Letters **12**, 4629 (2012).

[85] M. Monteverde, C. Ojeda-Aristizabal, R. Weil, K. Bennaceur, M. Ferrier, S. Guéron, C. Glattli, H. Bouchiat, J. N. Fuchs, D. L. Maslov, *Transport and Elastic Scattering Times as Probes of the Nature of Impurity Scattering in Single-Layer and Bilayer Graphene*, Physical Review Letters **104**, 126801 (2010).

[86] J. Martin, N. Akerman, G. Ulbricht, T. Lohmann, J. H. Smet, K. von Klitzing, A. Yacoby, *Observation of electron-hole puddles in graphene using a scanning single-electron transistor*, Nature Physics **4**, 144 (2008).

[87] R. Maurand, P. Rickhaus, P. Makk, S. Hess, E. Tovari, C. Handschin, M. Weiss, C. Schöenberger, *Fabrication of ballistic suspended graphene with local-gating*, Carbon **79**, 486 (2014).

[88] N. Tombros, A. Veligura, J. Junesch, M. H. D. Guimaraes, I. J. Vera-Marun, H. T. Jonkman, B. J. van Wees, *Quantized conductance of a suspended graphene nanoconstriction*, Nature Physics **7**, 697 (2011).

[89] D. J. Burmeister, G. D.W., *Stages in axion formation: observations of growth of Aplysia axons in culture using video -enhanced contrast-differential interference contrast microscopy*, Journal of Cell Biology **103**, 1921 (1986).

[90] M. Drienovsky, F.-X. Schrettenbrunner, A. Sandner, D. Weiss, J. Eroms, M.-H. Liu, F. Tkatschenko, K. Richter, *Towards superlattices: Lateral bipolar multi-barriers in graphene*, Physical Review B **89**, 115421 (2014).

[91] S. Dubey, V. Singh, A. K. Bhat, P. Parikh, S. Grover, R. Sensarma, V. Tripathi, K. Sengupta, M. M. Deshmukh, *Tunable Superlattice in Graphene To Control the Number of Dirac Points*, Nano Letters **13**, 3990 (2013).

[92] B. Huard, J. A. Sulpizio, N. Stander, K. Todd, B. Yang, D. Goldhaber-Gordon, *Transport Measurements Across a Tunable Potential Barrier in Graphene*, Physical Review Letters **98**, 236803 (2007).

[93] J. R. Williams, L. DiCarlo, C. M. Marcus, *Quantum Hall Effect in a Gate-Controlled p-n Junction of Graphene*, Science **317**, 638 (2007).

[94] M. T. Allen, J. Martin, A. Yacoby, *Gate-defined quantum confinement in suspended bilayer graphene*, Nature Communications **3**, 934 (2012).

[95] J. Velasco, L. Jing, W. Bao, Y. Lee, P. Kratz, V. Aji, M. Bockrath, C. Lau, C. Varma, R. Stillwell, D. Smirnov, F. Zhang, J. Jung, A. MacDonald, *Transport spectroscopy of symmetry-broken insulating states in bilayer graphene*, Nature Nanotechnology **7**, 156 (2012).

[96] R. T. Weitz, M. T. Allen, B. E. Feldman, J. Martin, A. Yacoby, *Broken-Symmetry States in Doubly Gated Suspended Bilayer Graphene*, Science **330**, 812 (2010).

[97] A. Castellanos-Gomez, M. Buscema, R. Molenaar, V. Singh, L. Janssen, H. S. J. van der Zant, G. A. Steele, *Deterministic transfer of two-dimensional materials by all-dry viscoelastic stamping*, 2D Materials **1**, 011002 (2014).

[98] C. Dean, A. Young, L. Wang, I. Meric, G.-H. Lee, K. Watanabe, T. Taniguchi, K. Shepard, P. Kim, J. Hone, *Graphene based heterostructures*, Solid State Communications **152**, 1275 (2012).

[99] J. R. Williams, T. Low, M. S. Lundstrom, C. M. Marcus, *Gate-controlled guiding of electrons in graphene*, Nature Nanotechnology **6**, 222 (2011).

[100] H. B. Heersche, P. Jarillo-Herrero, J. B. Oostinga, L. M. K. Vandersypen, A. F. Morpurgo, *Bipolar supercurrent in graphene*, Nature **446**, 56 (2007).

[101] C. W. J. Beenakker, *Specular Andreev Reflection in Graphene*, Physical Review Letters **97**, 067007 (2006).

[102] H. Hoppe, U. Zülicke, G. Schon, *Andreev reflection in strong magnetic fields*, Physical Review Letters **84**, 1804 (2000).

[103] N. M. Chtchelkatchev, I. S. Burmistrov, *Conductance oscillations with magnetic field of a two-dimensional electron gas–superconductor junction*, Physical Review B **75**, 214510 (2007).

[104] P. Recher, D. Loss, *Dynamical Coulomb Blockade and Spin-Entangled Electrons*, Phys. Rev. Lett. **91**, 267003 (2003).

[105] J. Schindele, A. Baumgartner, C. Schönenberger, *Near-Unity Cooper Pair Splitting Efficiency*, Phys. Rev. Lett. **109**, 157002 (2012).

[106] Z. B. Tan, D. Cox, T. Nieminen, P. Lähteenmäki, D. Golubev, G. B. Lesovik, P. J. Hakonen, *Cooper Pair Splitting by Means of Graphene Quantum Dots*, Physical Review Letters **114**, 096602 (2015).

[107] I. V. Borzenets, Y. Shimazaki, G. F. Jones, M. F. Craciun, S. Russo, Y. Yamamoto, S. Tarucha, *High Efficiency CVD Graphene-lead (Pb) Cooper Pair Splitter*, arXiv:1506.04597 (2015).

[108] J. Cayssol, *Crossed Andreev Reflection in a Graphene Bipolar Transistor*, Physical Review Letters **100**, 147001 (2008).

[109] V. E. Calado, S. Goswami, G. Nanda, M. Diez, A. R. Akhmerov, K. Watanabe, T. Taniguchi, T. M. Klapwijk, L. M. K. Vandersypen, *Ballistic Josephson junctions in edge-contacted graphene*, arXiv:1501.06817 (2015).

[110] M. Ben Shalom, M. J. Zhu, V. I. Fal'ko, A. Mishchenko, A. V. Kretinin, K. S. Novoselov, C. R. Woods, K. Watanabe, T. Taniguchi, A. K. Geim, J. R. Prance, *Proximity superconductivity in ballistic graphene, from Fabry-Perot oscillations to random Andreev states in magnetic field*, arXiv:1504.03286 (2015).

[111] M. Allen, O. Shtanko, I. C. Fulga, J. I.-J. Wang, D. Nurgaliev, K. Watanabe, T. Taniguchi, A. R. Akhmerov, P. Jarillo-Herrero, L. S. Levitov, A. Yacoby, *Visualization of phase-coherent electron interference in a ballistic graphene Josephson junction*, arXiv:1506.06734 (2015).

[112] B. Özyilmaz, P. Jarillo-Herrero, D. Efetov, D. A. Abanin, L. S. Levitov, P. Kim, *Electronic transport and quantum hall effect in bipolar graphene p-n-p junctions.*, Physical Review Letters **99**, 166804 (2007).

[113] R. V. Gorbachev, A. S. Mayorov, A. K. Savchenko, D. W. Horsell, F. Guinea, *Conductance of p-n-p graphene structures with "air-bridge" top gates.*, Nano Letters **8**, 1995 (2008).

[114] B. Huard, N. Stander, J. A. Sulpizio, D. Goldhaber-Gordon, *Evidence of the role of contacts on the observed electron-hole asymmetry in graphene*, Physical Review B **78**, 121402(R) (2008).

[115] G. Giovannetti, *Doping graphene with metal contacts*, Physical Review Letters **101**, 026803 (2008).

[116] M.-H. Liu, K. Richter, *Efficient quantum transport simulation for bulk graphene heterojunctions*, Physical Review B **86**, 115455 (2012).

[117] J. Cayssol, B. Huard, D. Goldhaber-Gordon, *Contact resistance and shot noise in graphene transistors*, Physical Review B **79**, 075428 (2009).

[118] S.-Y. Kwon, *Growth of semiconducting graphene on palladium*, Nano Letters **9**, 3985 (2009).

[119] M. Oksanen, A. Uppstu, A. Laitinen, D. J. Cox, M. F. Craciun, S. Russo, A. Harju, P. Hakonen, *Single-mode and multimode Fabry-Pérot interference in suspended graphene*, Physical Review B **89**, 121414 (2014).

[120] A. Varlet, M.-H. Liu, V. Krueckl, D. Bischoff, P. Simonet, K. Watanabe, T. Taniguchi, K. Richter, K. Ensslin, T. Ihn, *Fabry-Pérot Interference in Gapped Bilayer Graphene with Broken Anti-Klein Tunneling*, Physical Review Letters **113**, 116601 (2014).

[121] L. Campos, A. Young, K. Surakitbovorn, K. Watanabe, T. Taniguchi, P. Jarillo-Herrero, *Quantum and classical confinement of resonant states in a trilayer graphene Fabry-Pérot interferometer*, Nature Communications **3**, 1239 (2012).

[122] Y. Zhao, J. Wyrick, F. D. Natterer, J. F. Rodriguez-Nieva, C. Lewandowski, K. Watanabe, T. Taniguchi, L. S. Levitov, N. B. Zhitenev, J. A. Stroscio, *Creating and probing electron whispering-gallery modes in graphene*, Science **348**, 672 (2015).

[123] P. Rickhaus, P. Makk, M.-H. Liu, E. Tóvári, M. Weiss, R. Maurand, K. Richter, C. Schönenberger, *Snake trajectories in ultraclean graphene p-n junctions*, Nature Communications **6**, 6470 (2015).

[124] P. Ye, D. Weiss, R. Gerhardts, *Electrons in a periodic magnetic field induced by a regular array of micromagnets*, Physical Review Letters **74**, 3013 (1995).

[125] J. R. Williams, C. M. Marcus, *Snake States along Graphene p-n Junctions*, Physical Review Letters **107**, 046602 (2011).

[126] J. Bird, R. Akis, D. Ferry, D. Vasileska, J. Cooper, Y. Aoyagi, T. Sugano, *Lead-Orientation-Dependent Wave Function Scarring in Open Quantum Dots*, Physical Review Letters **82**, 4691 (1999).

[127] Y. Zhang, Y.-W. Tan, H. L. Stormer, P. Kim, *Experimental observation of the quantum Hall effect and Berry's phase in graphene.*, Nature **438**, 201 (2005).

[128] D. A. Abanin, L. S. Levitov, *Quantized Transport in Graphene p-n Junctions in a Magnetic Field.*, Science **317**, 641 (2007).

[129] A. Shytov, M. Rudner, L. Levitov, *Klein Backscattering and Fabry-Pérot Interference in Graphene Heterojunctions*, Physical Review Letters **101**, 156804 (2008).

[130] P. Carmier, C. Lewenkopf, D. Ullmo, *Semiclassical magnetotransport in graphene n-p junctions*, Physical Review B **84**, 195428 (2011).

[131] N. Davies, A. A. Patel, A. Cortijo, V. Cheianov, F. Guinea, V. I. Fal'ko, *Skipping and snake orbits of electrons: Singularities and catastrophes*, Physical Review B **85**, 155433 (2012).

[132] A. A. Patel, N. Davies, V. Cheianov, V. I. Fal'ko, *Classical and quantum magneto-oscillations of current flow near a p-n junction in graphene*, Physical Review B **86**, 081413 (2012).

[133] S. P. Milovanović, M. Ramezani Masir, F. M. Peeters, *Spectroscopy of snake states using a graphene Hall bar*, Applied Physics Letters **103**, 233502 (2013).

[134] S. P. Milovanović, M. Ramezani Masir, F. M. Peeters, *Magnetic electron focusing and tuning of the electron current with a pn-junction*, Journal of Applied Physics **115**, 043719 (2014).

[135] J.-C. Chen, X. C. Xie, Q.-F. Sun, *Current oscillation of snake states in graphene p-n junction*, Physical Review B **86**, 035429 (2012).

[136] C. W. J. Beenakker, R. A. Sepkhanov, A. R. Akhmerov, J. Tworzydlo, *Quantum Goos-Hänchen effect in graphene*, Physical Review Letters **102**, 146804 (2008).

[137] P. Rickhaus, M. Weiss, L. Marot, C. Schönenberger, *Quantum Hall effect in graphene with superconducting electrodes.*, Nano Letters **12**, 1942 (2012).

[138] T. Taychatanapat, J. Y. Tan, Y. Yeo, K. Watanabe, T. Taniguchi, B. Özyilmaz, *Conductance oscillations induced by ballistic snake states in a graphene heterojunction*, Nature Com **6**, (2015).

[139] S. Morikawa, S. Masubuchi, R. Moriya, K. Watanabe, T. Taniguchi, T. Machida, *Edge-channel interferometer at the graphene quantum Hall pn junction*, Applied Physics Letters **106**, 183101 (2015).

[140] S. W. McDonald, A. N. Kaufman, *Spectrum and Eigenfunctions for a Hamiltonian with Stochastic Trajectories*, Physical Review Letters **42**, 1189 (1979).

[141] E. J. Heller, *Bound-State Eigenfunctions of Classically Chaotic Hamiltonian Systems: Scars of Periodic Orbits*, Physical Review Letters **53**, 1515 (1984).

[142] M. C. Gutzwiller, *Periodic Orbits and Classical Quantization Conditions*, Journal of Mathematical Physics **12**, 343 (1971).

[143] S. Sridhar, *Experimental observation of scarred eigenfunctions of chaotic microwave cavities*, Physical Review Letters **67**, 785 (1991).

[144] J. Stein, H.-J. Stöckmann, *Experimental determination of billiard wave functions*, Physical Review Letters **68**, 2867 (1992).

[145] T. M. Fromhold, P. B. Wilkinson, F. W. Sheard, L. Eaves, J. Miao, G. Edwards, *Manifestations of Classical Chaos in the Energy Level Spectrum of a Quantum Well*, Physical Review Letters **75**, 1142 (1995).

[146] P. B. Wilkinson, T. M. Fromhold, L. Eaves, F. W. Sheard, N. Miura, T. Takamasu, *Observation of 'scarred' wavefunctions in a quantum well with chaotic electron dynamics*, Nature **380**, 608 (1996).

[147] C. M. Marcus, A. J. Rimberg, R. M. Westervelt, P. F. Hopkins, A. C. Gossard, *Conductance fluctuations and chaotic scattering in ballistic microstructures*, Physical Review Letters **69**, 506 (1992).

[148] L. Huang, Y.-C. Lai, D. K. Ferry, S. M. Goodnick, R. Akis, *Relativistic Quantum Scars*, Physical Review Letters **103**, 054101 (2009).

[149] X. Ni, L. Huang, Y.-C. Lai, C. Grebogi, *Scarring of Dirac fermions in chaotic billiards*, Physical Review E **86**, 016702 (2012).

[150] H. Xu, L. Huang, Y.-C. Lai, C. Grebogi, *Chiral Scars in Chaotic Dirac Fermion Systems*, Physical Review Letters **110**, 064102 (2013).

[151] L. Ying, L. Huang, Y.-C. Lai, C. Grebogi, *Conductance fluctuations in graphene systems: The relevance of classical dynamics*, Phys. Rev. B **85**, 245448 (2012).

[152] P. Rickhaus, M.-H. Liu, P. Makk, R. Maurand, S. Hess, S. Zihlmann, M. Weiss, K. Richter, C. Schönenberger, *Guiding of Electrons in a Few-Mode Ballistic Graphene Channel*, Nano Letters **15**, 5819 (2015).

[153] J. M. Pereira, V. Mlinar, F. M. Peeters, P. Vasilopoulos, *Confined states and direction-dependent transmission in graphene quantum wells*, Physical Review B **74**, 045424 (2006).

[154] G. W. Hanson, *Dyadic Green's functions and guided surface waves for a surface conductivity model of graphene*, Journal of Applied Physics **103**, 064302 (2008).

[155] C. E. P. Villegas, M. R. S. Tavares, *Comment on 'Guided modes in graphene waveguides'*, Applied Physics Letters **96**, 186101 (2010).

[156] R. R. Hartmann, N. J. Robinson, M. E. Portnoi, *Smooth electron waveguides in graphene*, Physical Review B **81**, 245431 (2010).

[157] Z. Wu, *Electronic fiber in graphene*, Applied Physics Letters **98**, 082117 (2011).

[158] D. a. Stone, C. a. Downing, M. E. Portnoi, *Searching for confined modes in graphene channels: The variable phase method*, Physical Review B **86**, 075464 (2012).

[159] X. Wang, Y. Ouyang, X. Li, H. Wang, J. Guo, H. Dai, *Room-temperature all-semiconducting sub-10-nm graphene nanoribbon field-effect transistors*, Physical Review Letters **100**, 206803 (2008).

[160] C. Stampfer, J. Güttinger, S. Hellmüller, F. Molitor, K. Ensslin, T. Ihn, *Energy Gaps in Etched Graphene Nanoribbons*, Physical Review Lettersm **102**, 056403 (2009).

[161] X. Liu, J. B. Oostinga, A. F. Morpurgo, L. M. K. Vandersypen, *Electrostatic confinement of electrons in graphene nanoribbons*, Physical Review B **80**, 121407 (2009).

[162] N. Tombros, A. Veligura, J. Junesch, M. H. D. Guimarães, I. J. V. Marun, H. T. Jonkman, B. J. van Wees, *Quantized conductance of a suspended graphene nanoconstriction*, Nature Physics **7**, 697 (2011).

[163] J. Baringhaus, M. Ruan, F. Edler, A. Tejeda, M. Sicot, A. Taleb-Ibrahimi, A.-P. Li, Z. Jiang, E. H. Conrad, C. Berger, C. Tegenkamp, W. A. de Heer, *Exceptional ballistic transport in epitaxial graphene nanoribbons.*, Nature **506**, 349 (2014).

[164] A. S. M. Goossens, S. C. M. Driessen, T. A. Baart, K. Watanabe, T. Taniguchi, L. M. K. Vandersypen, *Gate-Defined Confinement in Bilayer Graphene-Hexagonal Boron Nitride Hybrid Devices*, Nano Letters **12**, 4656 (2012), pMID: 22906072.

[165] S. Sutar, E. S. Comfort, J. Liu, T. Taniguchi, K. Watanabe, J. U. Lee, *Angle-Dependent Carrier Transmission in Graphene p-n Junctions*, Nano Letters **12**, 4460 (2012).

[166] R. N. Sajjad, S. Sutar, J. U. Lee, A. W. Ghosh, *Manifestation of chiral tunneling at a tilted graphene p-n junction*, Physical Review B **86**, 155412 (2012).

[167] F. Zhang, H. Min, M. Polini, A. H. MacDonald, *Spontaneous inversion symmetry breaking in graphene bilayers*, Physical Review B **81**, 041402 (2010).

[168] J. B. Oostinga, H. B. Heersche, X. Liu, A. F. Morpurgo, L. M. K. Vandersypen, *Gate-induced insulating state in bilayer graphene devices*, Nature M **7**, 151 (2008).

[169] F. Freitag, M. Weiss, R. Maurand, J. Trbovic, C. Schönenberger, *Homogeneity of bilayer graphene*, Solid State Communications **152**, 2053 (2012).

[170] A. Logg, M. K.-A., G. N. Wells, et. al., *Automated Solution of Differential Equations by the Finite Element Method*, Springer (2012).

[171] C. Geuzaine, J.-F. Remacle, *Gmsh: a three-dimensional fnite element mesh generator with built-in pre- and post-processing facilities*, International Journal for Numerical Methods in Engineering **79**, 1309 (2009).

A Simulation methods

A.1. 2-dimensional Carrier density simulation
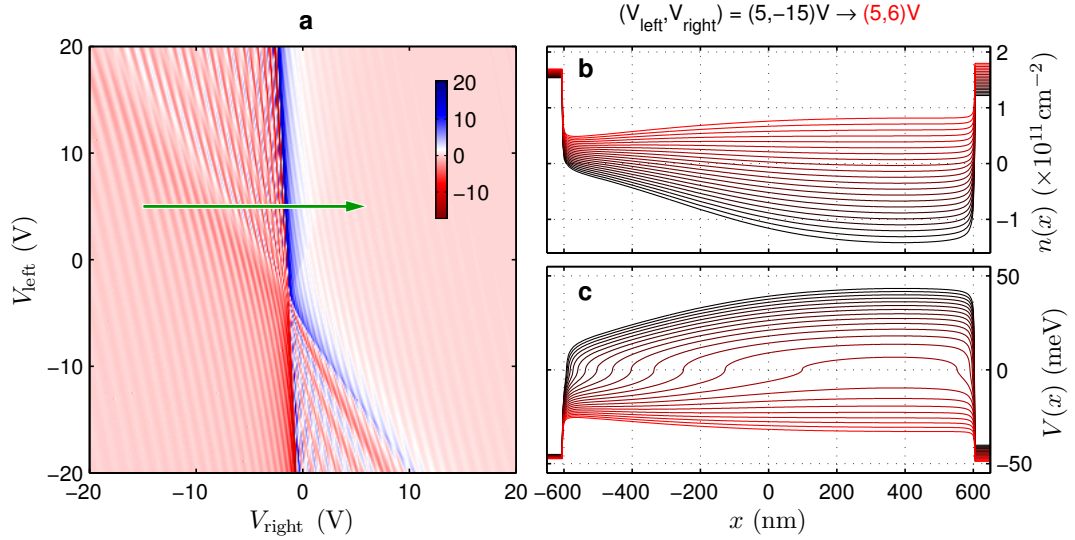
Figure A.1.: **c**, Calculated transconductance map obtained from the numerical derivative $dG(V_{\mathrm{right}}, V_{\mathrm{left}})/dV_{\mathrm{right}}$. The scale of the colorbar is in units of e^2/h per volt. **b**, An illustrating example of the simulated carrier density profile $n(x)$ subject to different gate voltages, and **c**, the corresponding on-site potential profile $V(x)$. The flat tails in **b** and **c** correspond to the contacted region (the leads), while the smooth profiles within $|x| \leq 605$ nm to the suspended graphene (the scattering region). The green arrow shown in **a** indicates the bottom gate voltage sweep considered in **b** and **c**.

The profile of $n(x)$ is computed by a finite-element-based electrostatic simula-

tor with the quantum correction accounted for through the quantum capacitance model [42], which allows to treat electric, chemical, and contact-induced doping in a unified manner. The simulator used throught this thesis by the theory collaborators first computes the self-partial capacitances $C_{\text{Lcontact}}(x)$, $C_{\text{Rcontact}}(x)$, $C_{\text{right}}(x)$, and $C_{\text{left}}(x)$ for the left contact, right contact, bottom gate, and the back gate, respectively. The carrier density is given by [42]

$$n(x) = n_C(x) + \text{sgn}[n_C(x)]n_Q(x)\left(1 - \sqrt{1 + 2\frac{|n_C(x)|}{n_Q(x)}}\right) + \text{sgn}(n_0)\sqrt{2n_Q(x)\,|n_0|},$$
(A.1)

where the first term is the classical contribution

$$n_C(x) = n_0 + \frac{C_{\text{Lcontact}}(x)}{e}V_c + \frac{C_{\text{Rcontact}}(x)}{e}V_c + \frac{C_{\text{left}}(x)}{e}V_{\text{left}} + \frac{C_{\text{right}}(x)}{e}V_{\text{right}}, \quad (A.2)$$

and the rest two terms are the quantum correction that requires

$$n_Q(x) = \frac{\pi}{2}\left(\frac{\hbar v_F}{e}\right)^2\left(\frac{C_{\text{Lcontact}}(x)}{e} + \frac{C_{\text{Rcontact}}(x)}{e} + \frac{C_{\text{left}}(x)}{e} + \frac{C_{\text{right}}(x)}{e}\right)^2 \quad (A.3)$$

in addition to the classical contribution n_C and the chemical doping n_0. In Equations (A.2) and (A.3), V_{left} and V_{right} are respectively the voltages applied on the back gate and the bottom gate and V_c is the "voltage" on the contacts.

As an example, the carrier density profile $n(x)$ given by Equations (A.1)–(A.3) with the self-partial capacitances computed using the MATLAB pdetool simulator, which is a partial differential equation solver based on the finite element method, is shown in Figure A.1b with different curves corresponding to the bottom gate voltage sweep indicated by the green arrow shown in Figure A.1a. The corresponding on-site potential profile $V(x)$ is shown in Figure A.1c and is then included in the Hamiltonian (A.5) to run the transport calculations.

A.2. 3-dimensional Carrier density simulation

For the devices in Chapters 6, 7 and 8 we calculated the two dimensional carrier density $n(x, y)$. For this purpose, the finite-element simulator FEniCS [170] together with the mesh generator GMSH [171] are adopted to compute the self-partial capacitances [42] of the individual metal contacts and bottom gates, which are functions of two-dimensional coordinates (x, y). The classical contribution to the total carrier density $n(x, y)$ is given by the linear combination of the capacitively coupled gate voltages and contact doping mainly arising from the charge transfer between the metal contacts and the graphene sheet. Some examples showing $n(x, y)$ profiles are given in Figure A.2 for the devices in the main thesis. The density close to the graphene
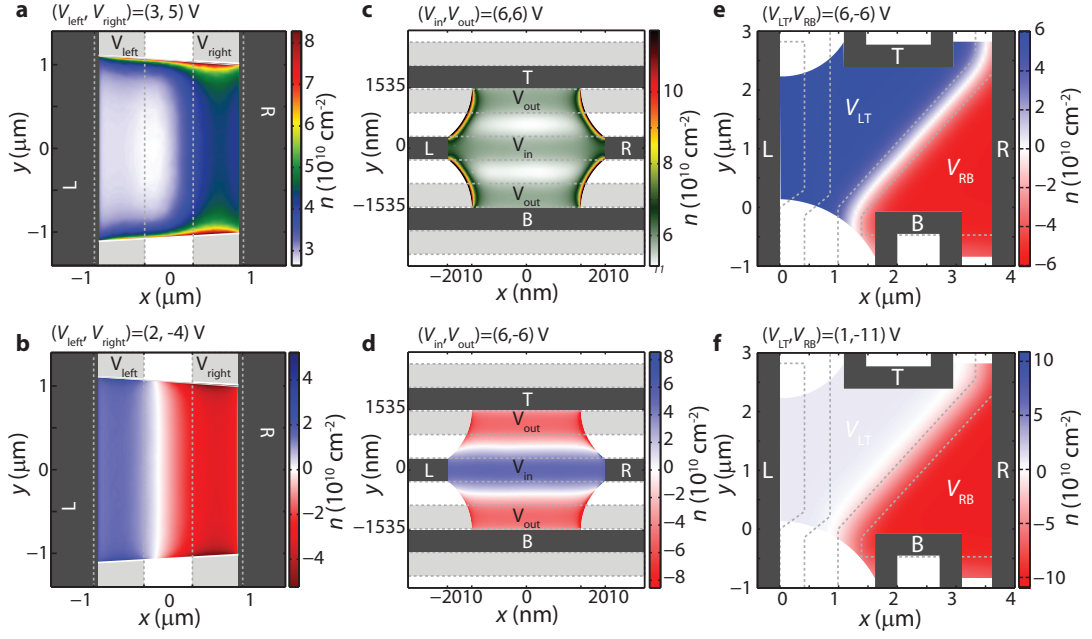
Figure A.2.: 3-dimensional carrier density simulation for different devices. **a**, $n(x,y)$ for the p-n device, as calculated in the snake-state chapter (Chapter 6) for unipolar and **b**, bipolar gating. **c**, Carrier density for an etched guiding device (Chapter 7) again for unipolar and **d**, bipolar gating. **e**, For the mirror device (Chapter 8), the p-n interface is moving drastically in the case of asymmetric gate voltages (**f**).

edge is consistently at least a factor of 2 higher than the bulk density.

A.3. Simulation of two-terminal graphene devices

Electronic transport through the suspended p-n graphene device of Chapter 5 is calculated using a real-space Green's function method within the Landauer-Büttiker formulation at zero temperature, based on a Bloch-theorem-assisted tight-binding model devised particularly for studying quasi-one-dimensional bulk graphene [116].

The Landauer two-terminal conductance G is computed in two steps. First, the dimensionless single-mode conductance g, which ranges between 0 and 2 due to the spinless tight-binding Hamiltonian with the valley degeneracy taken into account, is computed following the same method and parameters described in [116], except that a phenomenological mass term is considered in the lead self-energy in order to introduce a moderate reflection between the suspended and the contacted region even in the

unipolar regime. The mass term is described in the tight-binding model Hamiltonian as $\sum_i U_m \tau_i c_i^\dagger c_i$, where the operator $c_i^\dagger$ (c_i) creates (annihilates) an electron at site i, and $\tau_i = +1$ (-1) for the A (B) sublattice.[1] The strength of U_m, corresponding to one half of the gap opened, is set to be one-third of the energy spacing between the Fermi level and the Dirac point throughout the calculations.

Second, the number of modes M and the contact resistance R_c are considered to generalize the single-mode conductance g to the full conductance,

$$G = \frac{2e^2}{h} \left(\frac{1}{M \cdot g} + \frac{R_c}{h/2e^2} \right)^{-1}. \tag{A.4}$$

We use $M = W\sqrt{\bar{n}/\pi}$ for ideal bulk graphene with $\bar{n} = \overline{|n(x)|}$ the absolute carrier density averaged over the whole scattering region and the width of the graphene sample $W = 3.2\ \mu$m according to the SEM measurement. The contact resistance is deduced from the experimental quantum Hall data to be $R_c = 1.27$ k$\Omega \approx 0.05 h/e^2$. Thus Eq. (A.4) does not contain free parameters, and the main task in the simulation process is to compute the single-mode conductance g, which decisively depends on the on-site potential energy $V(x)$ included in the tight-binding Hamiltonian of the scattering region,

$$H = \sum_i V(x_i) c_i^\dagger c_i + H_0, \tag{A.5}$$

where H_0 describes ideal bulk graphene (see [116]) and x_i is the x coordinate of the site i.

A.4. Voltage to density mapping in Chapter 7

The detailed device geometry as they were used for the simulations are shown in FigureA.3a and b. The measurement setup for the guiding efficiency is explained in the Chapter 7: An AC voltage is applied to the source (S) contact and an AC current is simultaneously measured at the collector (C) and the side drain contacts (D1 and D2). In Figure A.3c we show the measured conductance between the S and C contact $G_{SC} = I_C/V_S$ and in Figure A.3d the conductance $G_{SD1D2} = (I_{D1} + I_{D2})/V_S$ between the source and side drain contacts. The guiding efficiency in Figure A.3e is then given by $\gamma = I_{SC}/(I_{SD1} + I_{SD2} + I_{SC}) = G_{SC}/(G_{SC} + G_{SD1D2})$.

Apparently the V_{out} scale for γ and for the Fabry-Pérot map G_{D1D2} (Figure A.3f) is shifted to high voltages. Whereas the global Dirac point is very close to $V_{in} = 0$V, it occurs at roughly $V_{out} = 30$V for the outer gate. The small shift in V_{in} and the

---

[1] The on-site energy term will be described by $\sum_i[U_m + V(x_L)]c_i^\dagger c_i$ for the left lead and $\sum_i[U_m + V(x_R)]c_i^\dagger c_i$ for the right lead, where $V(x_L)$ and $V(x_R)$ are the on-site energy at the left-most and right-most site in the scattering region, respectively.
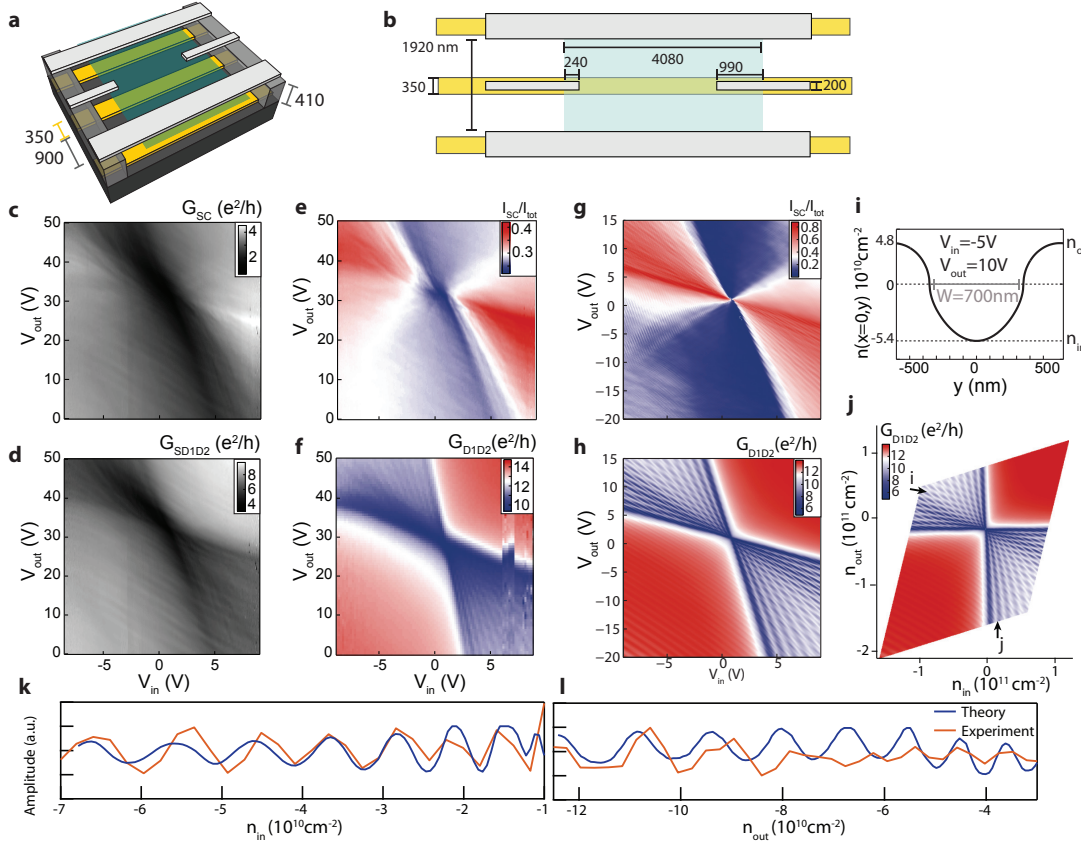
Figure A.3.: **Original data and density mapping. a-b**, 3D and top-view of the measured device with its dimensions used also for the simulations. **c**, The measured guiding conductance G_{SC} between left and right contact, **d**, and the simultaneously measured loss G_{SD1D2} between S and D1 and D2 contact. **e**, The guiding efficiency γ is calculated from these two maps, i.e. $\gamma = G_{SC}/(G_{SC} + G_{SD1D2})$. **f**, The Fabry-Pérot map is measured in a different configuration. **g**, The simulated guiding efficiency and the simulated Fabry-Pérot pattern **h** show the same crosstalk between the inner and outer gate. The voltage scale for the outer voltage V_{out} differs from the experimental data, but not the V_{in} scale. This is due to a problem with the backgate, i.e. the experimental V_{out} scale is not trustworthy. **i**, The density mapping is done according to calculated density profiles as shown in this Figure. **j**, The $G_{D1D2}(V_{in}, V_{out})$ to $G_{D1D2}(n_{in}, n_{out})$ mapping shears the data since the capacitive crosstalk is corrected. **k,l**, The comparison of the Fabry-Pérot oscillation period between experiment and theory reveals a successful voltage to density mapping. Plotted are the oscillations as a function of n_{in} in **k** and as a function of n_{out} in **l** along the directions marked with arrows in **j**. The curves where normalized after subtraction of the background conductance.

regular Fabry-Pérot pattern clearly demonstrate that the shift in V_{out} is not due to doping of the graphene but rather due to experimental problems with the backgate, that also lead to gate-jumps in the Fabry-Pérot map (Figure A.3f). The backgate was connected with a silver-paint and this connection might have become bad at low temperatures, leading to charging of the gates and to instabilities. We therefore discard the V_{out}-scale since the values are apparently not trustworthy, while keeping the V_{in}-scale.

By comparing to the simulated guiding efficiency (Figure A.3g) and Fabry-Pérot map (Figure A.3h) the correct density values for the experimental data can be extracted. This is possible since there are no free fitting parameters in the model and all geometrical parameters which do influence the capacitive crosstalk between the gates are fixed. In addition, the V_{in} voltage scale can be compared. Both experimental and theoretical data are mapped from $(V_{\text{in}}, V_{\text{out}})$ to $(n_{\text{in}}, n_{\text{out}})$ by using the local density profiles $n(x = 0, y)$ (Figure A.3i). The maximal absolute density in the channel n_{in} and of the maximal absolute density in the outer region n_{out} are obtained for all voltages $(V_{\text{in}}, V_{\text{out}})$. Such a mapping is done for the theoretical Fabry-Pérot map in Figure A.3j which is not shown in the 7. The data are sheared since the capacitive crosstalk between backgate and bottomgate is corrected.

The spacing of the Fabry-Pérot resonances represents a good control for the voltage to density mapping. Since the potential is smooth and the cavity size is changing with applied gate voltage, the experimental Fabry-Pérot resonances are best compared to the oscillations obtained in the tight-binding simulation, as it is done in Figure A.3k for the density in the channel and in Figure A.3l for n_{out}. As the periodicity of the measured and calculated oscillation is matching rather well, we conclude that the density is properly mapped. The density of two resonance maxima n_i and n_{i+1} are spaced $\sqrt{n_{i+1}} - \sqrt{n_i} = \sqrt{\pi}/W$, where W is the width of the channel. This can be obtained using the interference condition $k_F W = N\pi$ with N an integer. From the two first maxima in Figure A.3k (experimental or theoretical) a cavity size of $730\,\text{nm}$ is obtained, which corresponds well to the cavity size obtained from electrostatic simulations (see Figure A.3i).

B Fabrication Details and Recipes

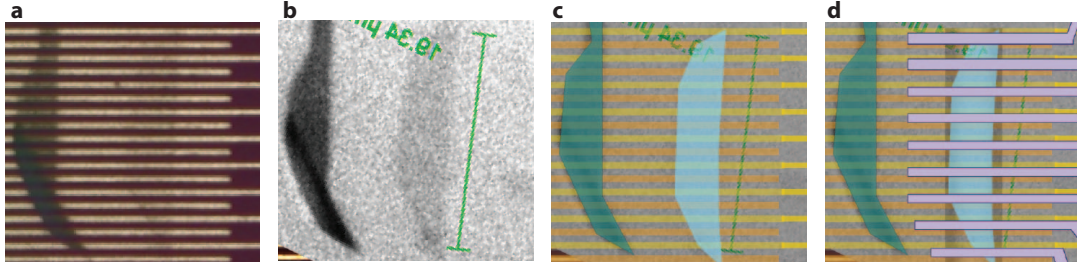## B.1. Design in Adobe Illustrator

Figure B.1.: **a**, After deposition of graphene on top of LOR, an optical picture is taken and the contrast is enhanced. **b**, This picture is aligned in Adobe Illustrator with an optical image of the same flake, recorded after exfoliation and before transfer. **c**, The image in **a** is also aligned with the bottomgate structure and afterwards the contacts (purple) and suspension mask (darkened) is designed.

After deposition of graphene, pictures are taken in the optical microscope (using contrast enhancement) and aligned in Adobe Illustrator CS5 (AI) with respect to predefined markers and with respect to an optical image of the graphene flake recorded before the transfer process, as shown in Figure B.2. After this, the structure is designed and exported as .dxf file.

We write our structures on a Zeiss Leo Supra 35 scanning electron microscope (SEM) with a Raith lithography system. The corresponding software is Raith Elphy Plus (v6). The export from AI as .dxf file and import to Elphy is successful if few rules are followed. They are summarized in Figure B.2: First, as shown in Figure B.2a, curved elements or splines need to be converted into polygons with straight lines. This is done in AI by first adding sufficient anchor points to the path (>Object
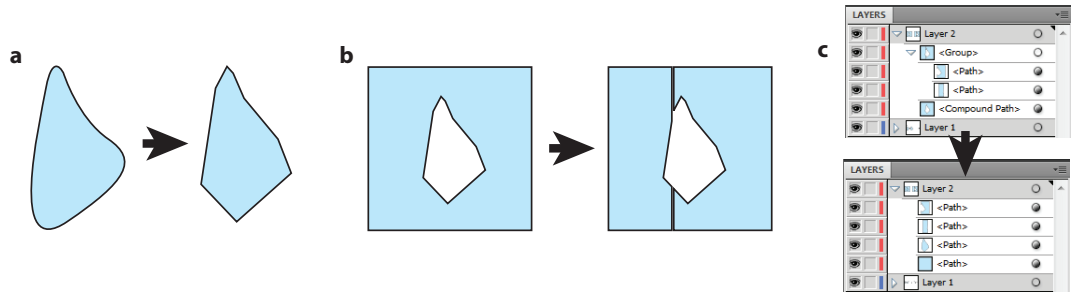
Figure B.2.: **a**, Curved structures (splines) need to be converted into polygons with straight lines. **b**, Structures with holes need to be cut apart. **c**, Grouped structures or compound paths need to be ungrouped.

>Path >Add Anchor Points, repeat if required) and then creating straight lines by the command >Object >Path >Simplify, then select "Straight Lines".

Second (Figure B.2b), structures with holes (appearing as <Compound Path> in the AI "Layers" panel) cannot be read by Elphy. We solve this by cutting the structures into half by drawing a very thin rectangle on top and using the "Minus Front" command from the Pathfinder panel.

Finally the "Layers" panel needs to be checked. All groups, compound paths or sublayers need to be ungrouped (>right click on path >Ungroup) for successful exporting as .dxf.

B.2. Wafer Characteristics

Wafers used in chapter 5 and 7.

- *Susbstrate material*   Si
- *Dopant*   p, boron
- *Resistivity*   0.003 - 0.005 Ωm
- *Capping layer*   300 nm silicon oxide

Wafers used in chapter 6.

- *Susbstrate material*   Si
- *Dopant*   undoped
- *Capping layer*   300 nm silicon oxide

B.3. Preparation of transfer wafers for graphene exfoliation

Clean wafer and get rid of water residues

1. Sonicate in acetone for 10 min
2. Sonicate in IPA, rinse and blow dry
3. UV/ozone treatment for 10 min (Model 42-220, Jelight Company, USA)
4. Baking on hotplate: 5' at 180°C

Spin-coating the dextrane layer must yield a uniform film

1. Spin-coat dextrane (10%w/v): 4000 rpm, 40", yields 250 nm
2. Hotplate 1'30" at 150°C
3. Spin-coat PMMA 950K (60% w/v in chlorobenzene): 4000 rpm, 40", yields 600 nm
4. Baking on hotplate: 1'30" at 150°C

B.4. Graphene exfoliation

The exfoliation recipe yields large-area flakes on LOR or PMMA surfaces but not on SiO_2, PVA or PPC.

1. Put a very shiny graphite flake (from "NGS naturgraphit") on blue scotch tape
2. Exfoliate roughly 7 times until the flake is covered with shiny graphite
3. Cover the tape with another piece of tape
4. Put the sandwiched graphene to a freezer

The PMMA/Dextrane wafer is prepared in the UVO. The duration of UVO exposure is crucial, but not well controlled. If the sample is for too short time in the UVO, its effect is minimal, if it is for too long in the UVO, it will break apart when the dextrane is dissolved. UVO duration time must be adjusted every time. The ideal time is the shortest time when imprints of the tape become visible in the PMMA layer.

1. Let the UVO warm up: after 10' the plasma seems stable
2. Put the PMMA/Dextrane wafer 1-2' to the UVO
3. Immediately after, get the tape from the freezer take the layers apart and put them on the wafer in the UVO
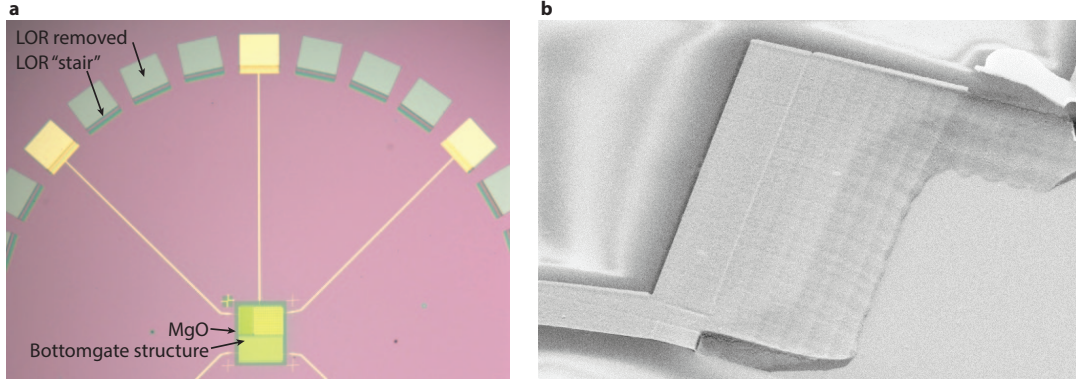4. Press the tape with the red tweezer cover to the sample and remove it

Figure B.3.: **a**, Bottomgate structure, covered with MgO and LOR where the bonding pads are developed **b**, SEM image of the steps in the bonding pads, covered with Pd.

B.5. Fabrication of LOR Base structure

B.5.1. Bottomgate structure

1. Spin-coating 500 nm (4000 rpm, 40") of PMMA (950K dissolved in Chlorobenzene) on a clean wafer
2. Hardening 3' on a hotplate at 180°C
3. Exposure Parameters: Acceleration voltage 20kV, Working distance 17 mm, Aperture: 10μm for small structures (250μm writefield) and 120μm for large structures (2 mm writefield). The dose-factors are set in the Elphy file.
   Dose: 200μC/cm^2 for normal structures
   Dose: 150μC/cm^2 for bottomgate pattern with gate distance of 600 nm
   Dose: 125μC/cm^2 for bottomgate pattern with gate distance of 300 nm
4. Development: 2' in Xylene, wash off with Hexane
5. E-beam evaporation: 5 nm Ti, 40 nm Au
6. Lift-off: 5-15' in 80°C Xylene, wash off with Hexane

The Au bottomgates need to be protected in order to avoid gate leakage.

1. Spin-coating of 500 nm PMMA, hardening 3' at 180 °C
2. Expose inner bottomgate structure (bonding pads need to remain covered with PMMA). Dose: $160\,\mu$C/cm^2
3. Development: 2' in Xylene, wash off with Hexane
4. E-beam evaporation: 100 nm MgO
5. Lift-off: 5-15' in 80°C Xylene, wash off with Hexane

B.5.2. LOR coating and bonding pads

After deposition of LOR, the bonding pads with a "stair"-structure need to be developed

1. Spin-coating of 600 nm of LOR 5A (2200 rpm, 45")
2. Hardening 15' at 200 °C
3. Exposure of bonding pads. The bonding pad is exposed with a dose of 600 μC/cm^2 and a stepwise decrease (steps of 40 μC/cm^2) along the direction where the connecting wires are expected to be
4. Development: 2' in Ethyl-lactate, washing thoroughly in 80 °C xylene using a syringe, wash off with Hexane

B.6. Graphene Transfer, deposition of contacts and etching

The Dextrane/PMMA/Graphene wafers are floating on water. The dextrane dissolves, leaving a PMMA/Graphene layer on the water. Using the tools described in Chapter 4 this layer is put on the volcano, with the flake of question in the middle of the volcano. Afterwards, the PMMA/Graphene is drying for several hours on the volcano. Then the flake is aligned with the bottomgate structure and deposited. The transfer stage should not be heated above 100 °C before the flake in question is in contact with the LOR wafer, otherwise it rolls up. After it is in contact, we heat to 150 °C and remove the volcano.

Pd contacts are written as a next step:

1. Spin-coating of 500 nm PMMA, hardening 3' at 180 °C
2. Expose Pd structure. Dose: 180 μC/cm^2
3. Development: 2'-4' in Xylene, wash off with Hexane
4. Thermal evaporation: 60 nm of Pd
5. Lift-off: 5-15' in 80°C Xylene, wash off with Hexane

Then the etching mask is written

1. Spin-coating of 500 nm PMMA, hardening 3' at 180 °C
2. Expose etching structure. Dose: 180 μC/cm^2
3. Development: 4' in Xylene, wash off with Hexane
4. Reactive Ion etching: O_2 plasma, 16 sccm flow, 25 mTorr background pressure, Power 30W, duration 1'. Cleaning of the RIE chamber beforehand by an Ar/O_2 plasma might be necessary.
5. Remove PMMA: 4 in 80°C Xylene, wash off with Hexane

Finally the graphene is suspended

1. Expose suspension structure. Dose: 1100 μC/cm^2
2. Development: 2' in Ethyl-lactate, 4' warm Hexane, blow-dry with N_2

Curriculum Vitae

Peter Simon Rickhaus
February 7 1987 born in Belp BE

Education

2011–2015	*PhD in experimental physics at the University of Basel* Disseration in the group of Prof. C. Schönenberger: "Electron optics in Graphene", winner of the SPS price 2015 from METAS
2009–2011	*Master of Science in Physics at the University of Basel* Master thesis in the group of Prof. C. Schönenberger, Basel: "Quantum Hall effect in Graphene with Superconducting Electrodes"
2006–2009	*Bachelor of Science in Nanosciences at the University of Basel*
2006	*Matura at the Gymnasium Laufen BL* Focus in visual arts, winner of the Novartis price in Laufen 2006

Positions

2011–2015	*Teaching assistant in physics*
2008–2011	*Teaching assistant in mathematics* "Mathematische Methoden I-IV"

Publications

Quantum Hall Effect in Graphene with Superconducting Electrodes
P. Rickhaus, M. Weiss, L. Marot, and C. Schönenberger
Nano Letters **12**, 1942-1945 (2012)

Ballistic interferences in suspended graphene
P. Rickhaus*, R. Maurand*, M.-H. Liu, M. Weiss, K. Richter
and C. Schönenberger
Nature Communications **4**, 2342 (2013)

Fabrication of ballistic suspended graphene with local-gating
R. Maurand*, P. Rickhaus*, P. Makk, S. Hess, E. Tóvári, C. Handschin, M. Weiss
and C. Schönenberger
Carbon **79**, 486-492 (2014)

Scalable Tight-Binding Model for Graphene
M.-H. Liu, P. Rickhaus, P. Makk, E. Tovari, R. Maurand, F. Tkatschenko, M. Weiss,
C. Schönenberger and K. Richter
Physical Review Letters **114**, 036601 (2015)

Snake trajectories in ultraclean graphene p–n junctions
P. Rickhaus, P. Makk, M.-H. Liu, E. Tóvári, M. Weiss, R. Maurand, K. Richter and
C. Schönenberger
Nature Communications **6**, 6470 (2015)

Guiding of Electrons in a Few Mode Ballistic Graphene Channel
P. Rickhaus, M.-H. Liu, P. Makk, R. Maurand, S. Hess, S. Zihlmann, M. Weiss, K.
Richter and C. Schönenberger
Nano Letters **9**, 5819–5825 (2015)

Klein tunneling based beamsplitter in ballistic graphene
P. Rickhaus*, P. Makk*, M.-H. Liu, K. Richter and C. Schönenberger
accepted in Applied Physics Letters

*both authors contributed equally to this article

Talks

- *Electron Optics in Ballistic Graphene*
  SPS-Price talk, Vienna, September 2015

- *Electron Optics in Ballistic Graphene*
  Talk at graphene 2015, Bilbao, March 2015

- *Electron Optics in Ballistic Graphene*
  Talk at the NCCR QSIT general meeting, Arosa, January 2015

- *Electron Optics in Ultraclean Graphene*
  Invited talk at the GRK1570 annual workshop, Schönsee, September 2014

- *Optik mit Elektronen in Graphene Nanostrukturen*
  Talk in front of the university council as representative of the physics department, Basel, September 2014

- *Snake States and Electron guiding in ultraclean Graphene*
  Talk at Graphene Week, Gotheborg, June 2014

- *Ballistic interferences in ultraclean p-n junctions in magnetic field*
  Invited talk at Graphene flagship meeting, Lancaster, April 2014

- *Quantum Hall effect and Andreev reflection*
  Talk at SPS general meeting, Zürich, Octobre 2011

- *Quantum Hall effect and Andreev reflection*
  Talk at QSIT lunch seminar, Zürich, June 2011

Poster Contributions

- *Electron Optics in Ballistic Graphene*, P. Rickhaus, P. Makk, S.Hess, R. Maurand, M. Weiss, M.H. Liu, C. Schönenberger, Poster at Spintech 8, Basel, 2015

- *Electron Optics with Ultraclean Suspended Graphene*, P. Rickhaus, S.Hess, P. Makk, R. Maurand, M. Weiss, M.H. Liu, C. Schönenberger. Poster at QSIT Review Meeting, Zürich, 2013

- *New Graphene heterostructures*, P. Rickhaus, M. Bräuninger, P. Makk, R. Maurand, M. Weiss, C. Schönenberger. Poster at QSIT Meeting, Arosa, 2013

- *Quantum Hall Effect in Graphene with Superconducting Contacts*, P. Rickhaus, M. Weiss, L. Marot, C. Schönenberger Poster at Graphene Week, Delft, 2012

- *Quantum Hall Effect in Graphene with Superconducting Contacts*, R. Maurand, M. Bräuniger, A.v.d. Torren, F. Freitag, P. Rickhaus, M. Weiss, C. Schönenberger. Poster at QSIT Meeting, Arosa, 2012

Acknowledgments

First, I am grateful to my thesis advisor Prof. Christian Schönenberger. With his enthusiasm and care he created an environment that was in many ways ideal for me. I remember several moments that were truly motivating. On the one hand, Christian recognized small steps and appreciated even little progress. On the other hand, we had long and intense discussions, as on the snake-state experiment, where Christian's expertise helped to really understand intriguing measurements. By his way of leading the group, Christian creates a collaborative spirit from which I benefited a lot. There was enough freedom to develop own ideas and enough guidance helping to complete open projects. And finally it does not go without saying that it was possible to find sufficient time for my family besides the work. This really boosted my motivation and creativity.

I would like to thank Prof. Lieven Vandersypen and Prof. Klaus Ensslin for making the effort to read this thesis. It is an honor that you joined the defense committee.

Great thanks goes to Peter Makk who has been supporting me in many ways. Thanks for thinking about projects, proof-reading the thesis, critical questions, uploading papers, filling Helium, evaporation of markers, and so on. I am truly grateful for all your help! I passed by your office many times, sometimes even without reason. I'd like to acknowledge also the great support of the other post-docs Markus Weiss, Romain Maurand and Minkyung Jung. Markus was the one who introduced me with a lot of patience and care to the basics of nanofabrication and who was a great support during the Master thesis and the PhD. Thank you for proof-reading, for precious hints regarding fabrication and for the many insightful discussions we had. I could profit a lot from Romains creativity. He was the one who imported the LOR fabrication technique to our group, which worked out so well for my thesis. I am grateful also for the many crazy ideas Romain had, few of which I realized. In the last year I had the chance to work with Minkyung Jung and I look forward to the RF results that will come.

Getting to know Ming-Hao Liu at graphene-week 2010 was good fortune, both on the scientific and on the personal level. We spent hours thinking about more or less realistic devices. I am very much aware that without his excellent simulations our work would not have had the same impact. I remember the Schweinshaxe in Regensburg and appreciate our common passion for excellent beer. I'd like to acknowledge also the support of Prof. Klaus Richter who was thoroughly proof-reading all of the publications. The collaboration with his group in Regensburg was extremely beneficial in many ways.

It was great working together with Samuel Hess, whom I supervised during his